Stony Brook University

High p_T Azimuthal Anisotropy in Au+Au Collisions at $\sqrt{s_{NN}} = 200$ GeV

A Dissertation Presented

by

Rui Wei

to

The Graduate School

in Partial Fulfillment of the Requirements

for the Degree of

Doctor of Philosophy

in

Physics

Stony Brook University

December 2010

Stony Brook University

The Graduate School

Rui Wei

We, the dissertation committee for the above candidate for the Doctor of Philosophy degree, hereby recommend acceptance of this dissertation.

Jiangyong Jia (Advisor)
Department of Chemistry

Roy Lacey
Department of Chemistry

Tommas Hemmick
Department of Physics and Astronomy

Derek Teaney
Department of Physics and Astronomy

Xu Du
Department of Physics and Astronomy

Stefan Bathe
Baruch College, CUNY & RIKEN Fellow

This dissertation is accepted by the Graduate School.

Lawrence Martin
Dean of the Graduate School

Abstract of the Dissertation

High p_T Azimuthal Anisotropy in Au+Au Collisions at $\sqrt{s_{NN}} = 200$ GeV

by

Rui Wei

Doctor of Philosophy

in

Physics

Stony Brook University

2010

A noval state of nuclear matter, in which quarks and gluons are deconfined, yet strongly coupled to each other, is created in Au+Au collisions at the Relativisitc Heavy Ion Collider (RHIC). This matter, which displays strong collective flow, and large opacity to the fast moving partons, are commonly refered to as the strongly-coupled quark gluon plasma (sQGP). Many efforts are ongoing to understand the microscopic properties of the strong interaction and the relaxation process leading to the rapid thermalization. The PHENIX experiment has measured the azimuthal anisotropy of π^0 at mid-rapidity ($|\eta| < 0.35$) in Au+Au collisions at $\sqrt{s_{NN}} = 200$

GeV in RHIC 2007 run (Run-7). It allows for detailed study of the anisotropy as a function of collision centrality and transverse momentum p_T in the range of 1-18 GeV/c. The observed anisotropy shows a gradual decrease up to p_T of 7-10 GeV/c and remains significantly above zero at $p_T > 10$ GeV/c. The $\Delta\phi$ dependent nuclear modification factors show a large split between the in-plane and out-of-plane directions, a large difference which exceeds the expectation from the energy loss models. In addition, the anisotropy of π^0 at mid-rapidity are measured with respect to the reaction planes reconstructed by four different reaction plane detectors located at forward region ($|\eta| > 1.0$), for the first time that the detailed study of the influence of non-flow due to jets on the measured v_2 at high p_T are presented. A jet absorption model is employed to study the importances of initial geometry and path length on the jet energy loss. An estimate of the increase in anisotropy expected from initial-geometry modification due to gluon saturation effects and fluctuations is insufficient to account for this discrepancy. Calculations that implement a path length dependence steeper than what is implied by current pQCD energy-loss models show reasonable agreement with the data.

To my family.

Contents

List of Figures

List of Tables

Acknowledgements

First, I want to express my gratitude to my parents who have always been there for me. I owe them more than I can put in here.

I am deeply indebted to my advisor, Professor Jiangyong Jia, for his patient guidance on my Ph.D. research. Jiangyong not only helped me build programming and data analysis skills from scratch, but also showed me a great example of an excellent physicist: creative, productive, meticulous, combined with deep insight of our field. He always provides effective advices when I am stuck in the research, and teaches me how to tackle the complex problems. He has also been a great friend of my personal life.

It was a great pleasure to work closely with Professor Roy Lacey, whose passion of doing innovative physics greatly inspired me. Roy always encouraged me to think creatively and too many times has proven his insightsive visionary thoughts. I thank Dr. Arkadij Taranenko who gave me a lot of suggestions on the analysis and also made office full of fun. I'd also like to acknowledge the Nuclear Chemistry Group at Stony Brook, Professor John Alexander, N. N. Ajitanand, for the fruitful discussions.

It has been an amazing experience working in the PHENIX collaboration. I especially thank Stefan Bathe, Takao Sagaguchi, Gabor David, Esumi

ShinIchi, Dave Winter, Justin Frantz, Shengli Huang, Chun Zhang, Wei Xie, Baldo Sahlmueller, Carla Vale for their generous help on my analysis. I thank all the collaborators for their hard work making PHENIX a productive experiment.

I want to share the moment with all the friends in Stony Brook, especially with Yan, Zhongkui, Xiaoxu, Xiaolan, Lei, Ying, Xu, Yingwu, Meng ...

Last but not the least, my wife Xiaoming deserves all my thanks and praises. It is her who made my life full of joy, who took care of me when the deadline came... None of my achievements is possible without her.

Chapter 1

Introduction

1.1 QCD and Quark Gluon Plasma

Quantum Chromodynamics (QCD) is the quantum field theory that describes the strong interactions at the *fm* scale between the quarks and gluons. It is a non-Abelian gauge theory describes two key features of strong interaction: asymtotic freedom and color confinement. The principle of asymtotic freedom [1] states that at the very small distance or large momemtum transfer q^2, the effective coupling constant α_s of QCD becomes small, and the quarks and gluons interact weakly. The consequence of this feature is that the interactions with large momentum transfer (Q^2 larger than a few GeV^2) can be calculated using the perturbative method. The perturbative QCD (pQCD) has been tested and verified by studying the particle production in elementary p+p, e^-+e^+... collisions. The other key feature is that the partons are confined inside the hadron, known as "color confinement". According to this feature, at the large distance the coupling between partons becomes so strong that per-

turbative method can not be applied. The only non-perturbative method to compute the QCD predictions in this regime is by the full numeric calculation of gauge theory on the lattice (Lattice QCD) [2]. The important prediction of Lattice QCD is the phase transition of bulk nuclear matter from a state where quarks and gluons are confined in hadrons (as in the normal hadronic matter) to a de-confined state at very high density and temperature, called Quark Gluon Plasma (QGP) [4]. Such matter is believed to exist during the first micro seconds of the universe after the "big bang", then it started to cool down, and partons combined together to form colorless hadrons. Lattice QCD predicts that such transition happened at 185 MeV $< T_c <$ 195 MeV [3], as indicated by the narrow bands in Figure 1.1 [1]. In the limit of massless non-interacting particles ("Stefan-Boltzmann" limit), one can estimate that such temperature corresponds to an energy density $\epsilon_c > 1.0$ GeV/fm^3 [2].

It was expected that QGP can be created in high energy heavy ion collisions [6], which took more than 25 years of efforts to reach the the QGP phase transition. The efforts started from the first relativistic heavy ion program at the Bevalac at LBL (with center of mass energy $\sqrt{s_{NN}} \sim 1$ GeV) in the early 1980s [7] (SIS at GSI in the 1990s nearly the same energy as Bevalac), to the AGS at BNL (with $\sqrt{s_{NN}} \sim 5$ GeV) and the SPS at CERN (with $\sqrt{s_{NN}} \sim 17$ GeV) in the 1990s [8], to the RHIC at BNL (with $\sqrt{s_{NN}} =$ 20-200 GeV) [9–12]. At AGS and SPS energies and below, there was no unambiguous evidence for QGP formation, although a number of signals found at SPS strongly suggested the formation of a "new state of matter" [13]. Only after the beginning of the RHIC program at 2000, evidences accumulated over the last 10 years show

[1] Other groups found a lower transition temperature 155 MeV $< T_c <$ 174 MeV [5].

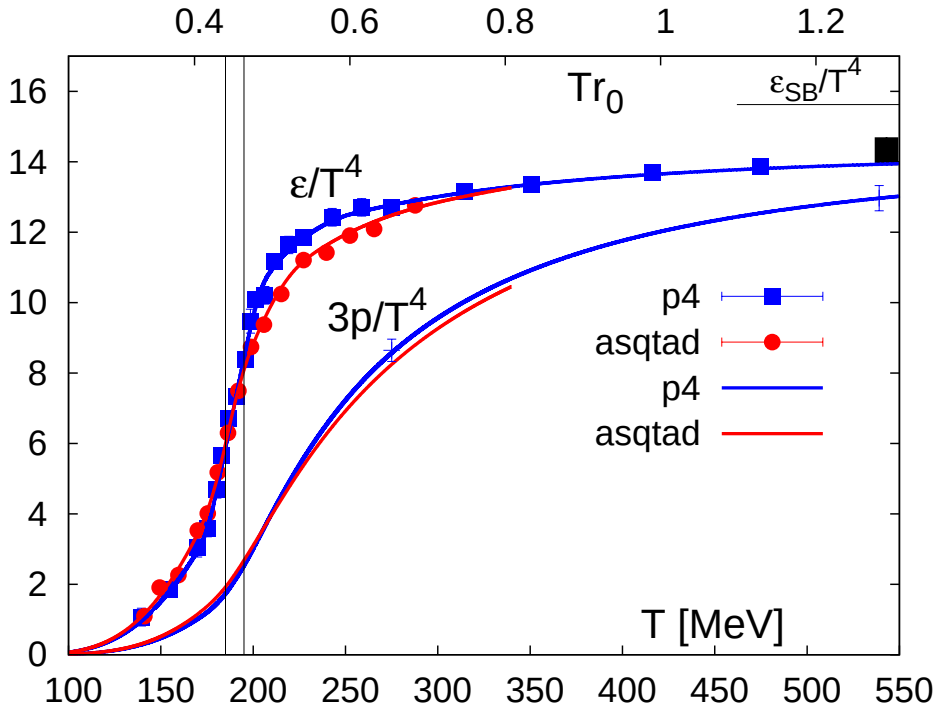

Figure 1.1: The QCD normalized energy density and pressure ϵ/T^4 and $3p/T^4$ as a function of temperature, calculated from lattice QCD [3].

that the QGP had been created and behaves strongly coupled [9–12, 14–16]. Another exciting heavy ion program at the LHC at CERN to the study the QGP at much higher temperature (with $\sqrt{s_{NN}} \sim 5.5$ TeV) is scheduled to start at the end of 2010 [17].

1.2 ultra-Relativistic Heavy Ion Collisions

In this section, we introduce the geometry associated with a heavy ion collision, and discuss the main features of different stages of the space-time evolution of the collision.

1.2.1 Collision Geometry for Heavy Ion Collision

Before discussing the observables for QGP, we first describe the initial geometry in a heavy ion collision, which is a key to interpret the RHIC results. The nucleon distribution inside the nucleus follows the Wood-Saxon density function:

$$\rho(r) = \frac{\rho_0}{1 + e^{\frac{r-R}{a}}} \tag{1.1}$$

where R fm is the nucleus radius, and a is the diffussness. For Au nucleus, $R = 6.38$ fm and $a = 0.535$ fm.

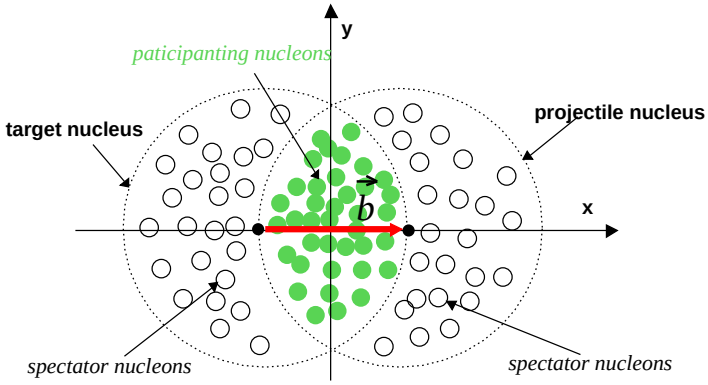

Figure 1.2: The collision geometry for an off center nucleus-nucleus collision.

Figure 1.2 shows a typical geometry for non-head-on nucleus-nucleus collision. The nucleons inside the overlap zone participate in the collisions, called "*participants*; while the rest keep traveling along the beam (z) without any collision, called "*spectators*". The impact parameter b, that connects the centers of two nuclei, controls the size of the overlap region and the number of participants (N_{part}) or the "*centrality*" of the collision. The events are sliced according to the centrality value, that 0-5% represents the most central col-

lisions, and 90-100% the most peripheral collisions. The plane spanned by the beam axis and impact parameter is called "*reaction plane*" (RP). In the collisions, this plane is randomly oriented (not neccessarily along x-axis as shown in Fig. 1.2). This orientation plays an important role in controling the pressure gradient and path length within the medium. Precisely determining the centrality and RP orientation is a crucial step to extract the collision information in the analysis.

1.2.2 Different Stages

Figure 1.3 and 1.4 schematically illustrate the different stages from the initial stage before the collision, the pre-equilibrium stage after the impact, followed by an expanding QGP stage and a final hadronization and freeze-out stage. In general, there is no unambiguous boundary to separate the stages during the entire system evolution. The life time of the collision is so short (∼10 fm/c) that it is impossible to study each phase individually in the experiment. Any contamination from other phase can influence the interpretation of the QGP phase. In more detail, these stages are characterized as belows:

- Initial stage:

  Two Lorentz contracted heavy nuclei approach each other with more than 99.9% of the speed of light at $\sqrt{s_{NN}}$ = 200 GeV. At sufficiently high collision energy, the particle production at mid-rapidity probes the nuclear structure functions in the small-x regime (x is the fraction between parton momentum and hadron momentum), and the gluon dis-

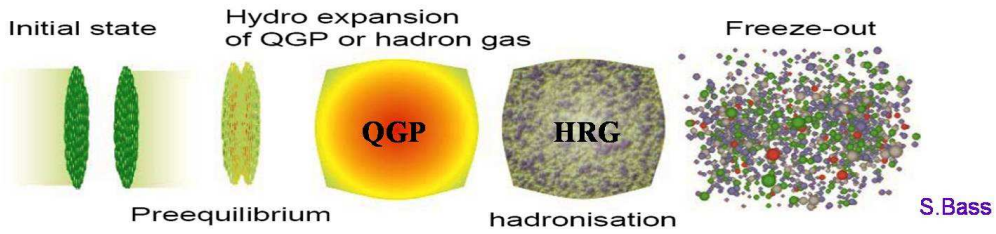

Figure 1.3: Different stages in a relativistic heavy ion collision [18].

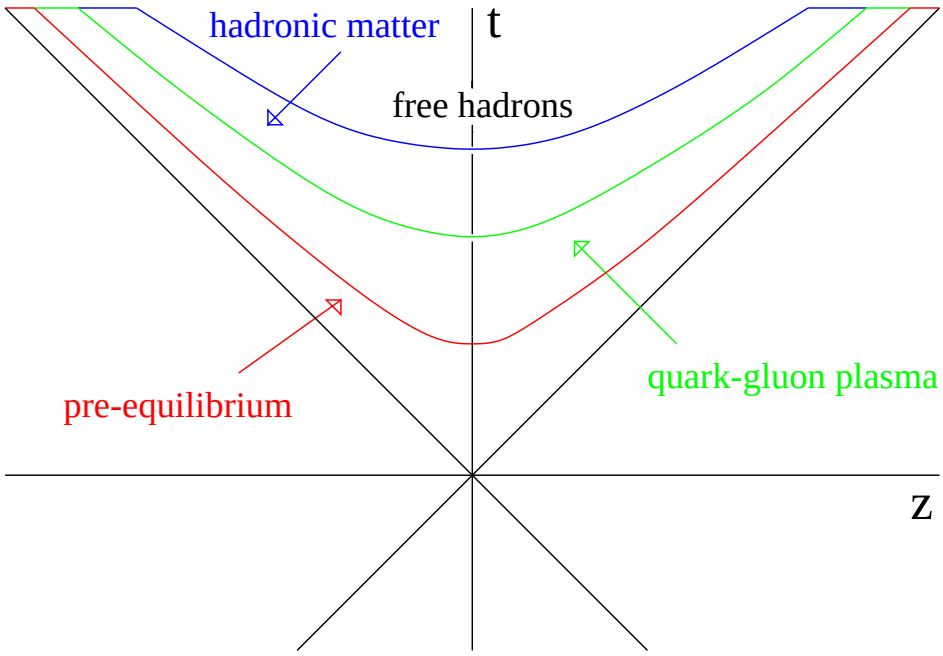

Figure 1.4: The space-time picture of a heavy ion collision [19].

tribution function $xG(x, Q^2)$ increases dramatically with decreasing x. When the gluon density becomes high enough, two gluons start to merge into one, which leads to gluon saturation below some momentum scale Q_s^2. When the saturation scale becomes large ($Q_s \gg \Lambda_{QCD}$), the coupling constant becomes weak ($\alpha_s(Q_s) \ll 1$) which suggests that the high energy limit of QCD may be studied using weak coupling techniques,

which can be formalized in an effective theory, the Color Glass Condensate (CGC) [20, 21].

- Pre-equilibrium:

  The energetic collision of two heavy nuclei excites the QCD vacuum and produces a dense pre-equilibrium matter consisting of quarks and gluons. The scattering of partons leads to local thermalization in the bulk matter and eventually the formation of deconfined QGP, a fast process which takes $\tau_0 \simeq$1 fm/c required by RHIC data [22]. The mechanism of such early thermalization is not well understood, since this stage can not be studied separately in experiment. However, it plays an important role in extracting the QGP matter properties. In this stage, the collisions between the fast partons within the collision zone generate a lot of "hard probes" with either large mass or large transverse momentum p_T, such as heavy quark pairs ($c\bar{c}$ and $b\bar{b}$), or very energetic quarks and gluons known as "jet". These hard probes can be calculated precisely in p+p collisions with pQCD, thus serve as well calibrated probes for the QGP phase.

- QGP and hydrodynamic expansion:

  The thermalized QGP, driven by the pressure gradient, expands and cools down quickly in the time scale of 5-10 fm/c. The system shows strong collective radial flow [24, 27] and large opacity to the fast moving partons [25]. The early success of hydrodynamic calculations at RHIC has implied that the system exhibits rapid thermalization and locally equilibrated (with little or no viscosity) [22]. The hydrodynamic ap-

proach requires knowledge of the equation of state (EoS), which gives a relation between pressure, energy and baryon density, but no detailed knowledge of the microscopic dynamics. Now, major efforts are focused on understanding the the transport properties, such as viscosity to entropy density ratio η/s, energy loss dE/dx, and transport coefficient $\hat{q}$ (Q^2/L, momentum square transfered per unit length). These transport properties are particularly important, because they are directly related to the non-equilibrium, microscopic scattering process of the system. Hence they provide insights on the effective degree of freedom of the QGP.

- Hadronization and freeze-out:

  After reaching the critical temperature T_c, the system hadronizes and turns into hadronic matter. The hadronic matter continues to expand until the system becomes very dilute. The individual hadrons decouple from the system (kinetic freeze-out) and free stream to the detector. Like the QGP hadronization process, the hadronic decoupling happens continuously at the edge of the fireball, where the density is low. The signals from QGP phase maybe "contaminated" in this stage. For example, theoretical study [26] shows that η/s increases rapidly as the temperature cools down in this stage, in distinction from the small values of η/s in the QGP phase.

Our understanding of the QGP properties deepens by the combination of looking for prominant signals and self-generated probes in the experiment and the advances of tools in theory.

1.3 RHIC Paradigm

In the last decade of the RHIC program, combined with various experimental observables and theoretical insights, it is widely accepted by the heavy ion physics community that the QGP is created at RHIC [9–11], and is strongly coupled [15], reaching thermal equilibration. The experimental observations include: large collective flow, constituent quark number scaling of the elliptic flow v_2, strong jet quenching and medium response.

1.3.1 Collective Flow

One of the most important discoveries at RHIC is that the medium displays strong collective dynamics which, for the first time in the history of particle and nuclear physics, could be quantitatively described by ideal hydrodynamics with small viscosity [27].

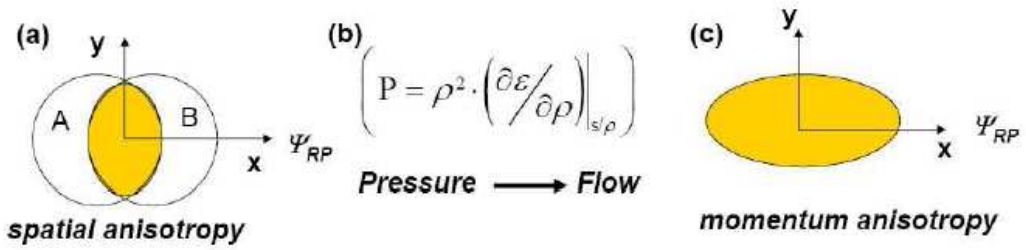

Figure 1.5: Schematic illustration of how pressure gradient converts inital spatial asymmetry to final state momentum anisotropy (elliptic flow).

The off-center collision between two Au nucleus creates an asymmetric overlap zone (Figure 1.5 a), where the short axis is aligned along the azimuth of the reaction plane (Ψ_{RP}). Its spatial asymmetry can be characterized by

the eccentricity (ϵ) of the participants in the overlap region:

$$\epsilon = \left\langle \frac{y^2 - x^2}{y^2 + x^2} \right\rangle, \tag{1.2}$$

where the average $\langle\rangle$ goes over all the participants and events. Since the pressure gradient in the x direction is larger than the y direction, the outward collective flow predominantly drives particle emission along the short axis of the ellipse. Rapid thermalization in the early stage converts the spatial anisotropy to a final state momentum anisotropy, known as "elliptic flow":

$$v_2 \equiv \left\langle \frac{p_y^2 - p_x^2}{p_y^2 + p_x^2} \right\rangle \tag{1.3}$$

or the second Fourier coefficient $\langle \cos 2(\phi_p - \Psi_{RP}) \rangle$ of the azimuthal distribution:

$$\frac{1}{p_T}\frac{dN}{dy dp_T d\phi} = \frac{1}{2\pi p_T}\frac{dN}{dy dp_T}(1 + 2v_2(p_T)\cos 2(\phi_p - \Psi_{RP}) + ...) \tag{1.4}$$

where Ψ_{RP} and ϕ_p are the azimuthal angle of reaction plane and emitted particle, respectively. The magnitude of v_2 reflects the ability of the QGP to convert initial spatial asymmetry into the final state momentum anisotropy, thus it is sensitive to the initial condition, equation of state (EoS), as well as the degree of the thermalization of the medium.

For mid-peripheral collisions ($b \simeq 7$ fm) the average elliptic flow v_2 is approximately 7%, which is surprisingly large. For instance, the ratio of particles in the x direction to the y is $\frac{1+2v_2}{1-2v_2} \simeq 1.3$. At higher transverse momentum $p_T \sim 1.5$ GeV/c, elliptic flow can be as large as 15%, in which the ratio of

in-plane to out-of-plane is ∼2:1. For transverse momentum $p_T < 1.5$ GeV/c, hydrodynamic calculations that model a locally equilibrated QGP with little viscosity show good agreement with the data (Figure 1.6), which indicates that the bulk of the matter is strongly coupled and behaves like an almost perfect fluid. This in turn implies a small shear viscosity to entropy density ratio η/s that almost saturate the conjectured lower bound, $\eta/s = 1/4\pi$, predicted by AdS/CFT for strongly coupled system [28].

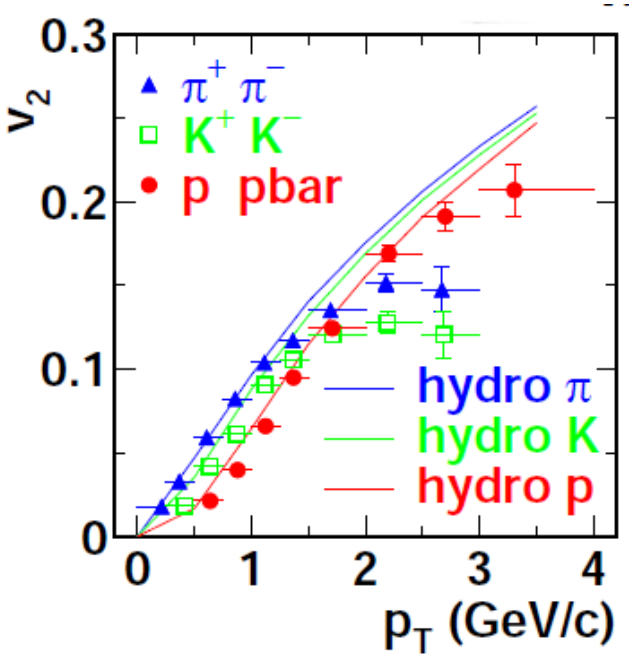

Figure 1.6: Elliptic flow (v_2) vs p_T for different particle species [24]. The ideal-hydro calculations (lines) show good agreement.

Recently, many efforts are ongoing to extract the η/s from the elliptic flow measurement [29, 30]. According to ideal hydrodynamics, elliptic flow v_2 should scale with the inital eccentricity, i.e. v_2/ϵ is a constant as a function of centrality [31]. Any non-zero shear viscosity will not only reduce the value, but also break the eccentricity scaling behavior. By comparing the centrality

dependence of v_2/ϵ between data and viscous hydro calculation [31], RHIC experimentalists have estimated the value of η/s to be a few times of the lower bound. Similar constraints have been obtained by comparing the viscous hydro calculation with the p_T dependence of v_2 [32], as well as by comparing transport model calculations with the v_2 data [33]. Current world estimation [34] set the value of viscosity to be $\eta/s \leq 5/4\pi$. Despite the large uncertainties, this value is still the smallest among all known substances including the liquid He at its critical temperature [35].

The elliptic flow data also suggests that the large collective flow is developed at the partonic stage, QGP phase [36]. Figure 1.7 shows the v_2 value as a function of transverse kinetic energy KE_T ($KE_T = \sqrt{m^2 + p_T^2} - m$), which is a better choice than p_T since the flow is driven by the pressure gradient. A characteristic splitting between measons and baryons is observed. More striking feature is shown on the right plot, when scaled both axis by the number of constituent quarks. All particles species fall onto the same curve, which strongly suggests that the flow is carried by the quark degrees of freedom in the QGP. This phenomena can be well explained by the quark recombination model [37], in which the baryons and mesons are generated by the coalescence of valence quarks that flow within the medium.

Despite the great success of relativisitic hydrodynamics in interpreting the RHIC elliptic flow data, there are still many open questions to be addressed:

- Uncertainty of inital geometry (ϵ):

  Two most common geometric models as the input for hydro calculations are Glauber and CGC models [38]. The former assumes that the initial

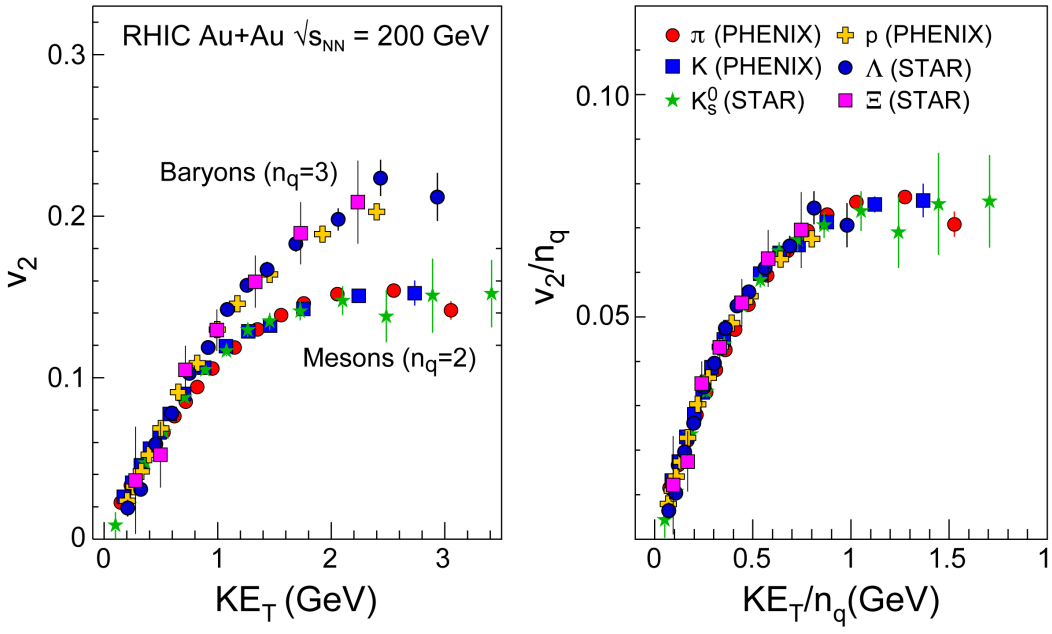

Figure 1.7: Left: v_2 vs KE_T (transverse kinetic energy) for different particle species. Mesons and baryons split at high KE_T. Right: v_2/n_q vs KE_T/n_q. All particle species fall onto a universal curve.

entropy density of QGP is proportional to the combination of participant and collision densities from Glauber model (Figure 1.2):

$$\rho_0 \propto \frac{1-\delta}{2}\rho_{\mathrm{part}} + \delta\rho_{\mathrm{coll}}. \tag{1.5}$$

where the $\delta = 0.14$ [39]. The CGC model takes into account the gluon saturation effect at low x region. Both models are tuned to match the RHIC multiplicity measurement data. However, the eccentricity calculated from these two models can differ up to 30%, an uncertainty which can translate into 100% in η/s extraction [38, 40]. The difficulty lies in that there are no known probes of the reaction zone that escape directly from the fireball and probe only the initial state, without any contribu-

tions from later stages of the expansion.

- Equation of state (EoS):

  The hydrodynamic calculations require the knowledge of the EoS of the medium, $p(e, n)$, and this EoS, through the speed of sound $c_s^2(T) = \frac{\partial p}{\partial e}$, controls the enegy momentum expansion of the medium [41]. The EoS has been calculated by the Lattice QCD, which suggests a cross-over from hadronic phase to QGP phase instead of a first-order phase transition at $\mu = 0$ [42].

- Hadronic freeout:

  As the produced QGP expands and cools, it evolves through a phase described by a hadron gas with rapidly increasing η/s [26]. To precisely identify the contribution from the hadronic stage is a crucial part in interpreting the RHIC results. However, there still lacks direct experimental observables to constrain its contribution.

1.3.2 Jet Quenching

In heavy ion collisions, the hard-scattered partons provide as an important tool in extracting the QGP properties. The production of these partons is well understood in p+p collisions. Any deviation from the expectation of nucleus-nucleus collisions can be attributed to the modification of the QGP phase.

Hard Scattering

At the very beginning of the hadronic collision (e.g. $p + p \rightarrow h + X$), the hard scattered incoming quarks and gluons create a pair of energetic fast moving partons with large transverse momentum. Each of the two fast partons will finally fragment into a spray of hadrons, forming what is called "jet" (Figure 1.8). The hard-scattering happens on a very short time scale and particle production from hard-scattering can be calculated in perturbative QCD (pQCD) framework. For example, the leading order cross section for the process can be calculated by the factorization theorems [43]:

$$\begin{aligned}\frac{d\sigma^{NN}}{dyd^2p_T} &= \sum_{abcd}\int dx_a dx_b d^2k_{aT} d^2k_{bT} g_p(k_{aT}, Q^2) g_p(k_{bT}, Q^2) \\ &\quad f_{a/p}(x_a, Q^2) f_{b/N}(x_b, Q^2) \frac{D^0_{h/c}(z_c, Q^2)}{\pi z_c} \\ &\quad \frac{d\sigma}{d\hat{t}}(ab \rightarrow cd)\delta(\hat{s} + \hat{t} + \hat{u}),\end{aligned} \tag{1.6}$$

where $f_{a/p}(x_a, Q^2)$ is the parton distribution function, $D_{h/c}$ is the fragmentation function, and $\frac{d\sigma}{dt}$ is the parton-parton cross section. pQCD calculations have been very successful in describing the high p_T particle yields in high en-

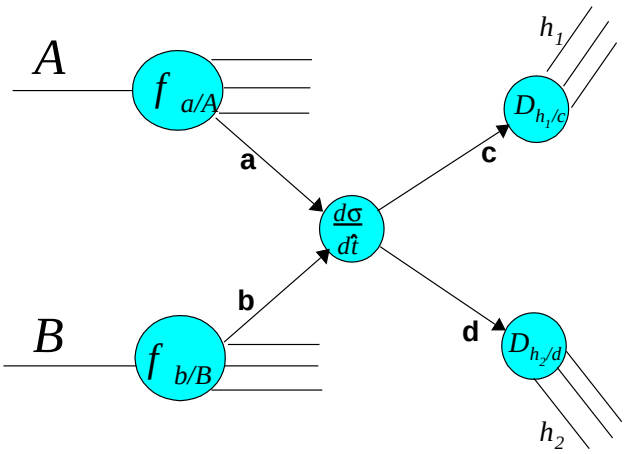

Figure 1.8: Schematic representation of a high-p_T reaction factorized into parton distribution functions (f), parton fragmentation functions (D), and a hard-scattering subprocess.

ergy p+p collisions [44–47]. Figure 1.9 shows the π^0 spectra measured by the PHENIX in p+p collisions at $\sqrt{s_{NN}} = 200$ GeV, together with a next leading order pQCD calculations [48–50] based on the factorization theorem. These calculations are consistent with the data down to $p_T \sim 2$ GeV/c, indicating that the particle production is dominated by the fragmentation of the hard-scattered parton. The success of pQCD in p+p collisions provided us a well calibrated self-generated probe in nucleus-nucleus collisions.

Jet Quenching in QGP Medium

If the hot-dense medium is formed after the collision with a large volumn and long life time, the high p_T jets can be used to probe the properties of the medium. According to QCD, these jets loss energy when traveling through the medium [51, 52]. The main energy loss machnisms are the elastic collisional energy loss and inelastic radiative energy loss due to the medium induced gluon

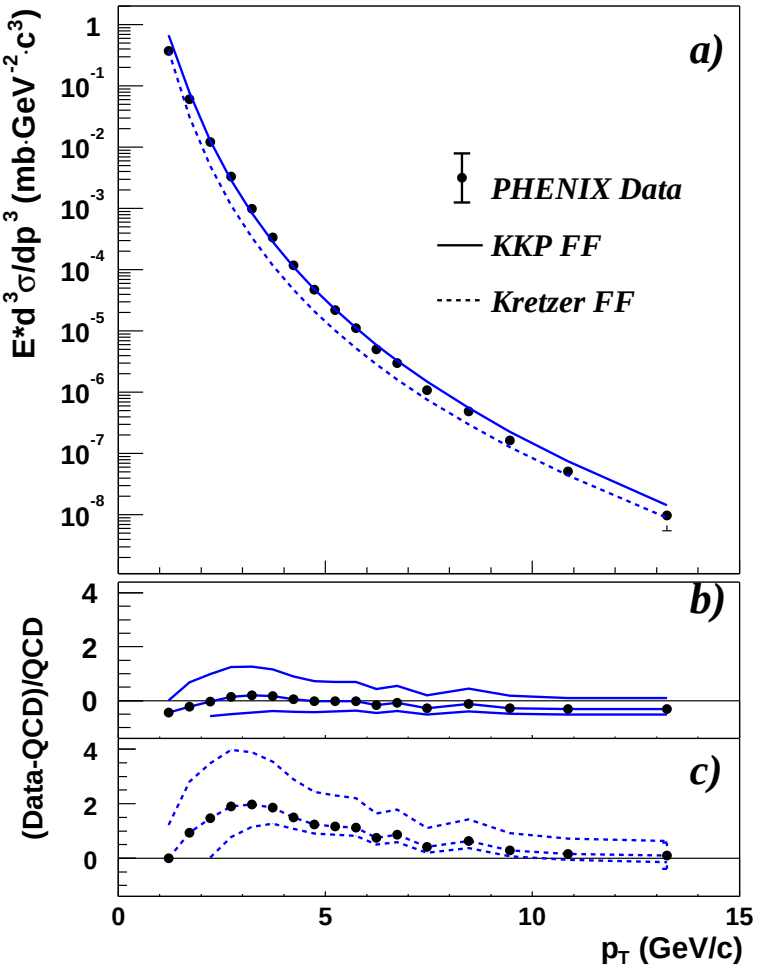

Figure 1.9: a) The invariant differential cross section for inclusive π^0 production and results from NLO pQCD calculations using the "KKP" [49](solid line) and "Kretzer" [50] (dashed line) sets of fragmentation functions. b,c) The relative difference between the data and the theory uing KKP (b) and Kretzer (c) fragmentation functions with scales of $p_T/2$ (lower curve), p_T and $2p_T$ (upper curve). This figure is taken from [47].

radiation [53, 54]. They soften the energy of the hard scattered partons, thus effectively reduces the high p_T hadron yields, known as "jet quenching". The energy loss is dominated by the radiative energy loss, which can be expressed

as

$$\Delta E \sim -\alpha_s \hat{q} L^2, \tag{1.7}$$

for partons travelling through a homogeneous medium of length L [55]. The $\hat{q}$ characteries the stopping power of the medium:

$$\hat{q} = \rho \int dq^2 q^2 \frac{d\sigma}{dq^2} \sim \frac{\mu^2}{\lambda_f}. \tag{1.8}$$

Here ρ denotes the density of color charges in the medium and $d\sigma/dq^2$ is the differential scattering cross section for a parton on a color charge. μ is the inverse color screening length and λ_f denotes the mean free path of an energetic parton in the medium. In the experiment, the jet quenching is quantified by the so called nuclear modification factor R_{AA}, which is defined by the ratio of the yield in nucleus-nucleus collisions to the yield in p+p collisions, normalized by the average number of nucleon-nucleon collisions in A+A collisions:

$$R_{AA} = \frac{1/N_{AA}^{evt} d^2 N_{AA}^{\pi^0}/dp_T dy}{\langle T_{AA} \rangle \times d^2\sigma_{pp}^{\pi^0}/dp_T dy}, \tag{1.9}$$

where dN_{AA} is the differential yield in Au+Au, $d\sigma_{pp}$ is the differential cross section in p+p in a given p_T bin, and $\langle T_{AA} \rangle$ is the overlap function for the centrality being analyzed:

$$\langle T_{AA} \rangle \equiv \frac{\int T_{AA}(\mathbf{b}) d\mathbf{b}}{\int (1 - e^{-\sigma_{pp}^{inel} T_{AA}(\mathbf{b})}) d\mathbf{b}} \tag{1.10}$$

from which the mean number of binary collisions can be calculated, $\langle N_{coll} \rangle = \sigma_{pp}^{inel} \langle T_{AA} \rangle$.

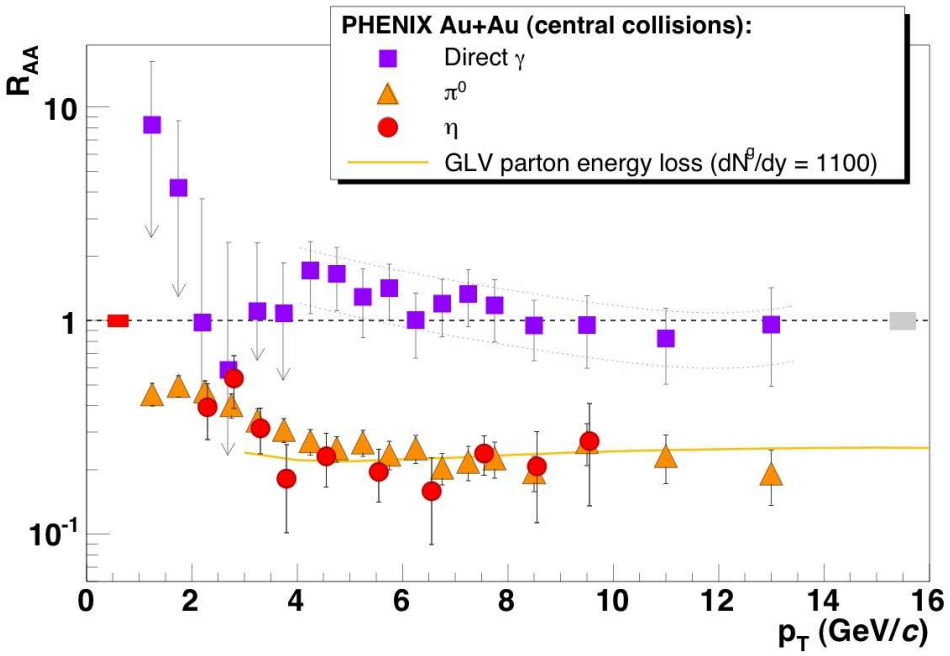

Figure 1.10: The nuclear modification factor R_{AA} as function of transverse momentum p_T for direct photons γ, as well as π^0 and η mesons in central Au+Au collisions [56].

One of the most striking observations at RHIC is that the high p_T particle yields in Au+Au collisions at top energy is found to be factor of 5 suppressed in the most central collision [25] (Figure 1.10). In contrast to the large suppression of hadrons, no modification is found for direct photon which interacts only electrodynamically and thus escape from the medium with very little energy loss. The experimental data of R_{AA} can be used to determine the value of $\hat{q}$ for the QGP, which requires a realistic modeling of the reaction geometry and its time evolution.

Most theoretical models of jet quenching are based on the pQCD framework, which assumes that the coupling of jets with the medium is weak (due to the large momentum transfer) even though the medium itself is strongly

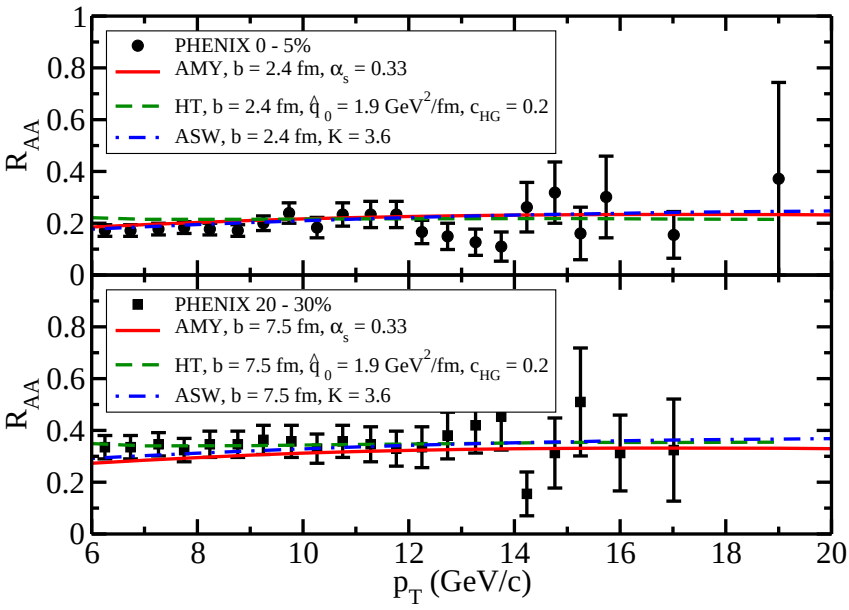

Figure 1.11: Nuclear modification factor R_{AA} in Au+Au collisions at 0-5% (top) and 20-30% (bottom) centrality calculated in the ASW, HT and AMY approaches compared to the PHENIX data [57].

$\hat{q}(\boldsymbol{r},\tau)$ scales as	ASW $\hat{q}_0$	HT $\hat{q}_0$	AMY $\hat{q}_0$
$T(\boldsymbol{r},\tau)$	10 GeV^2/fm	2.3 GeV^2/fm	4.1 GeV^2/fm
$\epsilon^{3/4}(\boldsymbol{r},\tau)$	18.5 GeV^2/fm	4.5 GeV^2/fm	
$s(\boldsymbol{r},\tau)$		4.3 GeV^2/fm	

Table 1.1: The $\hat{q}$ values calculated in ASW, HT and AMY models from [57]. There are large uncertainties between different theoretical models in the extracted $\hat{q}$ values.

coupled. By adjusting the input parameters, such as coupling strength, temperature, gluon density, these models can all produce the observed suppressions of single hadron spectra and di-hadron correlations. Figure 1.11 taken from Ref. [57] shows the R_{AA} calculations from three pQCD based models (abbreviated as ASW, HT and AMY) compared to the experimental data. The models are tuned to match the central suppression level (0-5%) at one high p_T bin, and then calculate the values in other p_T and centralities. All three models can describe the p_T and centrality dependence of R_{AA} quite well. However, the medium properties implied by these input parameters, such as $\hat{q}$, the momentum broadening per unit length, differs significantly among the models as shown in Table. 1.1. This uncertainty is largely due to the energy loss bias intrinsic in the single- and di-hadron observables, which makes them not very sensitive to the details of model implementations. Further progress requires not only theoretical development to understand limitations of perturbative assumptions and to reconcile different pQCD models, but also experimental observables that are more sensitive to jet quenching mechanism.

Azimuthal angular correlations between a high p_T triggered particle with other energetic hadrons provide additional strong support for the picture of significant parton energy loss in the QGP medium. Energy momemtum conservation requires that the hard scattered pair partons move in opposite directions. This leads to back-to-back correlation between the resulting jets, as shown by two peaks in the azimuthal angle correlation separated by 180°. Such back-to-back signal is clearly observed in p+p and d+Au collisions. In central Au+Au collisions, however, one only sees the near-side peak, while the away-side peak disappeared as shown on Figure 1.12. This is consistent with

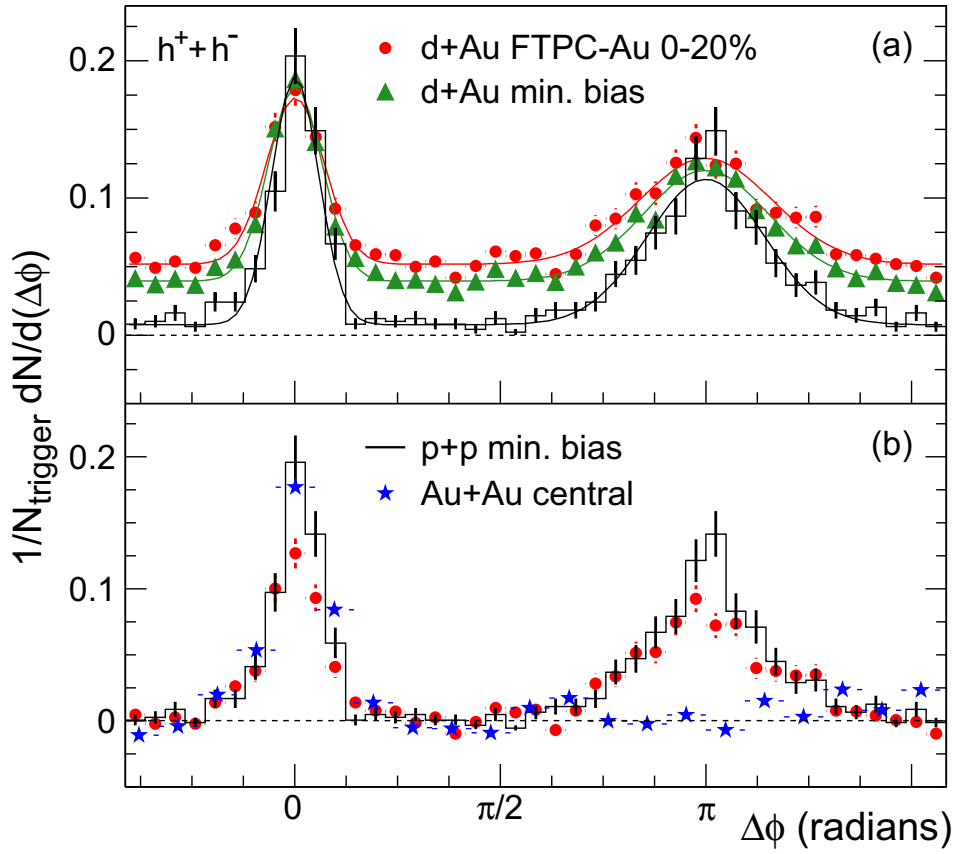

Figure 1.12: (a) Efficiency corrected two-particle azimuthal distributions for minimum bias and central d+Au collisions, and for p+p collisions. (b) Comparison of two-particle azimuthal distributions for central d+Au collisions to those seen in p+p and central Au+Au collisions. The figure is taken from [58].

the picture of surface emission, that the di-jets are generated at the surface of the medium, with one jet leaving outward of the medium, the other one traveling towards inside the medium and suffering large energy loss, thus getting quenched inside. Figure 1.13 shows the trigger and partner p_T dependences of the correlation, where (b), (c) reveal an interesting feature, the double peak structure at the away side when the partner p_T is below 3GeV/c, which is attributed to the medium response to the fast moving parton through the medium, such as Mach cone shock wave [60].

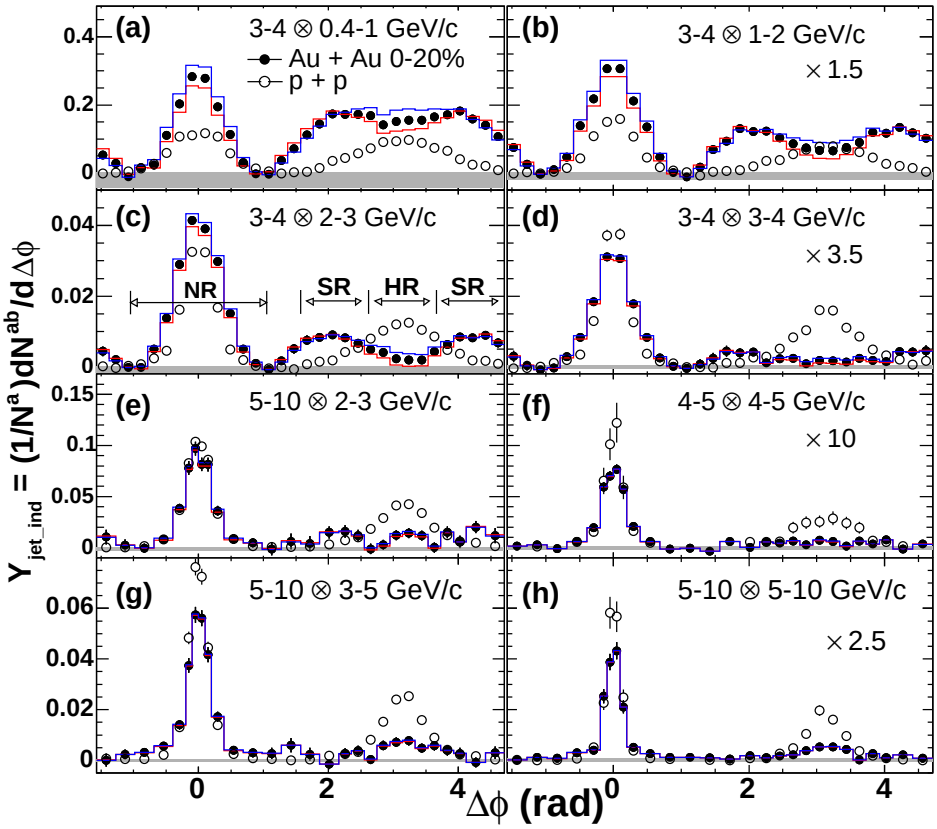

Figure 1.13: Two particle azimuthal angular correlations in Au+Au 0-20% collisions [59]. The away side is suppressed when partner p_T >3 GeV/c. Below double peak structures at away side imply medium response to the fast moving parton.

1.4 High p_T Azimuthal Anisotropy

At high p_T, the azimuthal anisotropy

$$\frac{dN}{d(\phi - \Psi_{RP})} = N(1 + 2v_2 \cos 2(\phi - \Psi_{RP})) \tag{1.11}$$

is believed to be due to the path length dependent energy loss, since the amount of matter a jet has to penetrate varies with $\phi - \Psi_{RP}$. In the in-plane direction (short axis), the partons go through less medium than the out-of-plane

direction. Unlike energy loss in QED, the radiative gluon energy loss per unit length dE/dx not only depends on the color charge density and momentum distribution of the medium, but also linearly depends on the thickness of the medium, due to the non-Abelian nature of gluon radiation in QCD. Thus, v_2 at high p_T is sensitive to the path length dependence of energy loss, which qualitatively scales as $\Delta E \propto l$, $\Delta E \propto l^2$ and $\Delta E \propto l^3$ for collisional, radiative and non-perturbative (via AdS/CFT) energy loss [61], respectively. Previous measurements [62] suggest a large v_2 that exceeds the expectation from pQCD models. However the error above 6 GeV/c, where the jet quenching picture may start to become applicable, is too large to distinguish these models.

In this dessertation, we present the precision measurement of π^0 azimuthal anisotropy in $\sqrt{s_{NN}} = 200$ GeV Au+Au collisions from RHIC 2007 run (Run-7). By measureing π^0 at PHENIX, we can study different p_T regions that are dominated by different physics mechanisms, especially in the intermediate p_T (2.5-4 GeV/c), the transition region from collective flow to jet fragmentation. We will also discuss the important influences of initial geometric shape on the jet quenching interpretation. The v_2 data extend to p_T of 18 GeV/c and achieve a 5-15% statistical error between 5-10 GeV/c. The data quality are much improved compared to Run-4 results, by taking advantage of four times more statistics and better reaction plane resolution from the newly installed reaction plane detectors. The latter improvement also enables us first time to study the non-flow effects due to jets on the measured v_2. We implement simple jet absorption models to study the effects of different geometries, fluctuations and different path length dependences of energy loss on the final observables.

We point out that the azimuthal anisotropy is a more sensitive probe than the nuclear modification factor R_{AA} to distinguish between different energy loss models, and can help to constrain the uncertainties in the theoretical calculations.

1.5 Organization of the Dissertation

The dissertation is organized as follows. Chapter 2 gives an overview of the PHENIX detector and discusses the subsystems relevant for this work in more detail. Chapter 3 presents the detailed data calibration needed for this analysis. Chapter 4 details the data reduction and analysis procedures. In Chapter 5, the results will be presented and discussed, and a jet absorption model will be studied to help our understanding of the results. Chapter 6 will give a summary of the work and the outlook of future work.

Chapter 2

Experiment Setup

2.1 RHIC

The Relativistic Heavy Ion Collider (RHIC) [63] at Brookhaven National Laboratory is a world class machine, able to accelerate a wide variety of nuclei upto 100 GeV per nucleon and proton upto 500 GeV. It builds on the previous accelerator program of the Alternating Gradient Synchrotron (AGS). The designing luminosity for gold beam is 200 $b^{-1}sec^{-1}$ and 20 $\mu b^{-1}sec^{-1}$ for proton averaged over a 10 hour fill. Collisions occur at the six intersections of two independent accelerator rings in which ions are grouped into bunches to increase collision rates while minimizing the average current. Each ring contains 360 RF buckets separated in time by 106 ns. Ions are injected in bunches from the AGS into these buckets one at a time. A range of 6 to 56 bunches can be injected and provided for collisions at each of the six interaction points simultaneously. To minimize intra-beam scattering, the injection is performed in less than a minute. The acceleration from injection energy to

up to 100 GeV/nucleon is achieved within 2 minutes. At this time the bunches are transferred to the storage RF system which limits the bunch length growth to 30 cm rms. This parameter is important because it directly impacts the size of the collision diamond at the experiments and the usable luminosity.

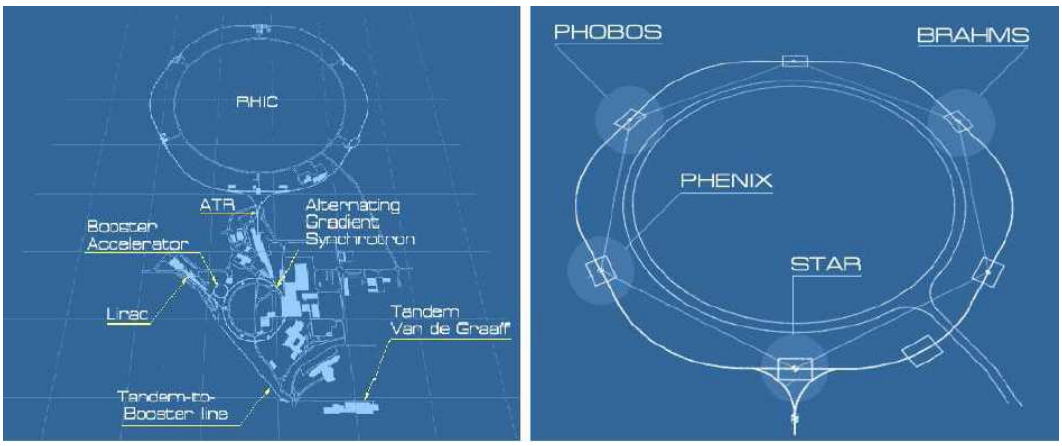

Figure 2.1: (Left) The accelerator facilities at Brookhaven National Laboratory. (Right) The layout of interaction points and four experiments along the ring.

The left figure on Figure 2.1 shows the path of a gold ion through the accelarator complex, the Tandem - Van de Graaff, the Booster synchrotron, the AGS, and finally RHIC. The gold ions begin their journey in the Tandem where negative gold ions extracted from a pulsed sputter ion source and the ions with total charge Q_T = -1 are accelerated through 14 MV potential. After the negative ions passing through the stripping foil in the positive high voltage terminal with a positive charge Q_T. The positive ions are then accelerated back to the ground potential for a gain of $14 \times Q_T$ MeV. The product of the Tandem is a beam of gold ions with a charge of +12 and 1 MeV/nucleon kinetic energy. Upon exiting the Van de Graaff, the gold ions are further stripped to a charge of +32 before traversing the 850 meter long heavy ion transfer line to the Booster

synchrotron. The gold beams are captured into six bunches and accelerated to 95 MeV/nucleon before exiting the Booster where all but the two most tightly bounded K-shell electrons are stripped. Almost half of all ions from the Tandem are successfully accelerated and stripped in the Booster. The gold ions with charge of +79 are filled in the AGS in four Booster cycles totaling 24 bunches. They are re-bunched into four bunches before being accelerated to 8.86 GeV/nucleon and exiting the AGS where they are fully stripped. The ions are transfered to the RHIC storage rings via the AtR beamline. There are four experiments at RHIC, PHENIX, STAR, PHOBOS and BRAHMS, as shown on the right figure of Figure 2.1. PHENIX and STAR are the only two still running, while PHOBOS and BRAHMS have stopped their commissions.

RHIC can virtually accelerate all species from proton (A = 1) to gold ions (A = 197). By the summer of 2010, RHIC has collied Au+Au at $\sqrt{s_{NN}}$ = 9.6, 19.6, 62.4, 130, 200 GeV/nucleon, Cu+Cu at $\sqrt{s_{NN}}$ = 130, 200 GeV/nucleon, d+Au at $\sqrt{s_{NN}}$ = 200 GeV/nucleon, and polarized p+p at $\sqrt{s_{NN}}$ = 200, 500 GeV.

2.2 PHENIX Experiment

PHENIX [64], the Pioneering High Energy Nuclear Interaction eXperiment, is an exploratory experiment for the investigation of high energy collisions of heavy ions and protons. PHENIX is a multipurpose experiment, designed to meet the high multiplicity environment created in high energy heavy ion collisions to measure electro magnetic probes of the medium and charged hadrons emerged from the hot collision zone.

The PHENIX detector consists of over 11 subsystems, grouped into three types of detectors:

- Global detector, for centrality, reaction plane etc,
- Two central arms at mid-rapidity, for γ, e etc,
- Two muon arms at forward rapidity, for μ.

The global detectors, including Beam-Beam Counter (BBC) and Zero Degree Calorimeter (ZDC), measure the time and position of the collisions, and the multiplicity of produced particles. In addition, the Reaction Plane detectors (RxNP) was installed in Run-7 for the purpose of improving reaction plane determination. As shown on the top pannel of Figure. 2.2, the central arms cover the rapidity range of $|\eta| < 0.35$, 180° of azimuth angle, instrumented to detect electrons, photons and charged hadrons. It consists of tracking detectors: Drift Chamber (DC) and Pad Chamber (PC), and particle identification detectors: Time-of-Flight detector (TOF), Electro Magnetic Calorimeters (EMCal) and Ring Imaging Cerenkov detectors (RICH). The forward muon arms have full azimuthal coverage and are designed to detect muons. This analysis does not involved muon arms, thus they will not be discussed in the dissertation. Each of the four arms has geometric acceptance of approximately 1 steradian. The detailed Runs information of PHENIX is listed in Table. 2.1. The baseline layout of the PHENIX detector during Run-7 is shown in Figure 2.2, and the subsystems are summarized in Table. 2.1

Table 2.1: A list of physics run and corresponding parameters in the PHENIX experiment.

Run	Species	$\sqrt{s_{NN}}$ (GeV)	$\int Ldt$	N_{events}	Year
RUN-1	Au+Au	130	1 μb^{-1}	10 M	2000
RUN-2	Au+Au	200	24 μb^{-1}	170 M	2001/2002
	p+p	200	0.15 pb^{-1}	3.7 G	
RUN-3	d+Au	200	2.74 nb^{-1}	5.5 M	2002/2003
	p+p	200	0.35 pb^{-1}	6.6 G	
RUN-4	Au+Au	200	241 μb^{-1}	1.5 G	2003/2004
	Au+Au	62.4	9 μb^{-1}	58 M	
	p+p	200	0.35 pb^{-1}	6.6 G	
RUN-5	Cu+Cu	200	3 nb^{-1}	8.6 G	2004/2005
	Cu+Cu	62.4	0.19 nb^{-1}	0.4 G	
	Cu+Cu	22.5	2.7 pb^{-1}	9 M	
	p+p	200	3.8 pb^{-1}	85 G	
RUN-6	p+p	200	10.7 pb^{-1}	230 G	2005/2006
	p+p	62.4	0.1 pb^{-1}	28 G	
RUN-7	Au+Au	200	813 μb^{-1}	5.1 G	2007

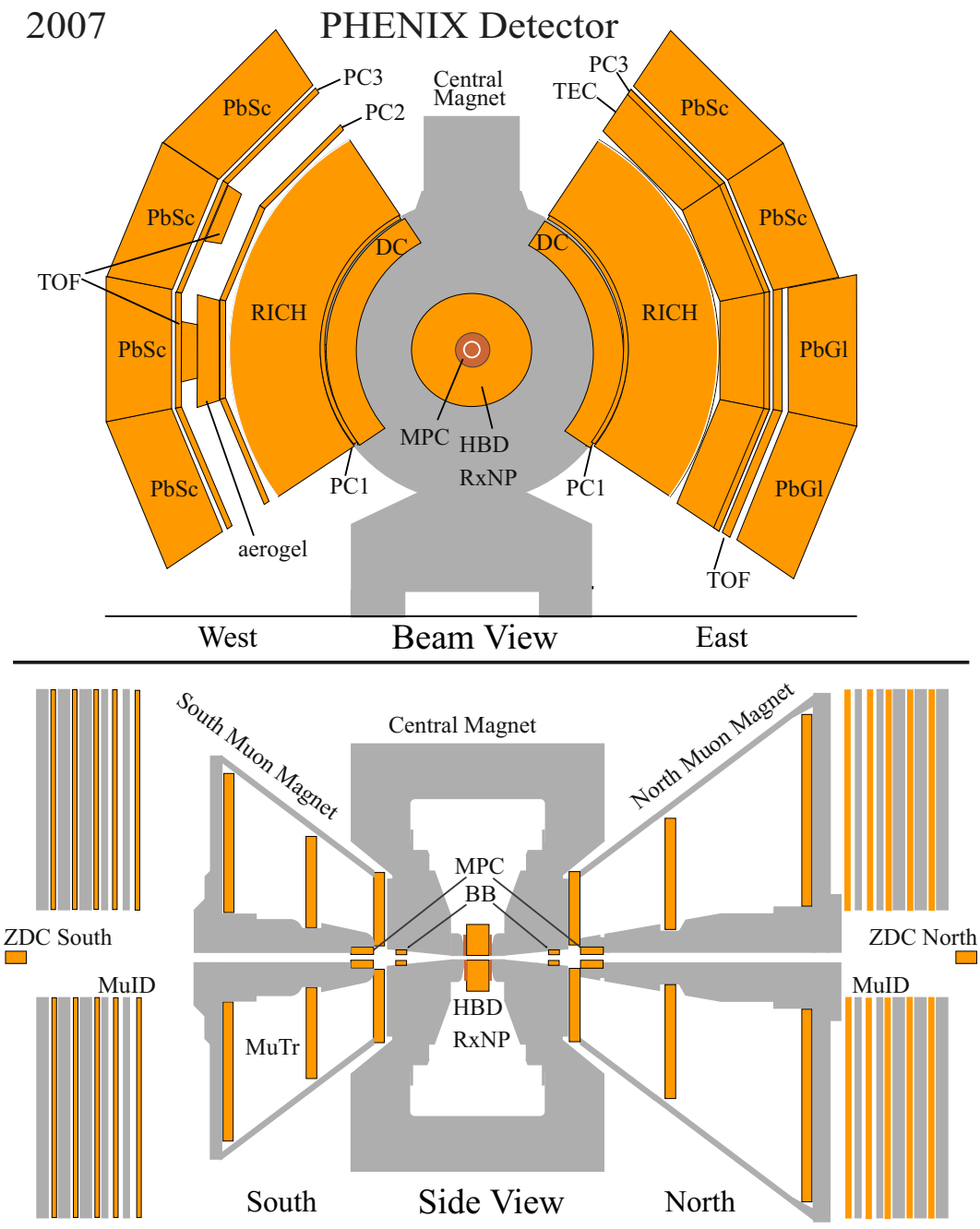

Figure 2.2: Layout for PHENIX experiment during Run-7. The top panel shows the central arms viewed along the beam axis. The bottom panel shows a side view of the PHENIX.

Table 2.2: Summary of the PHENIX detector subsystems.

Component	η	ϕ	Purpose and Feature
Magnet: central	< 0.35	2π	Up to 1.15 T·m
muon (MMS)	-1.1 to -2.2	2π	0.72 T·m for $\eta = 2$
muon (MMN)	1.1 to 2.4	2π	0.72 T·m for $\eta = 2$
BBC	3.0< $\|\eta\|$ <3.9	2π	Global timing and vertex
ZDC	± 2 mrad	2π	Minimum bias trigger
DC	$\|\eta\|$ <0.35	$\frac{\pi}{2} \times 2$	Good momentum and mass resolution
			$\Delta m/m = 0.4\%$ at $m = 1.0$GeV
PC	$\|\eta\|$ <0.35	$\frac{\pi}{2} \times 2$	Pattern recognition
			tracking for nonbend direction
RICH	$\|\eta\|$ <0.35	$\frac{\pi}{2} \times 2$	Electron identification
TOF	$\|\eta\|$ <0.35	$\frac{\pi}{4}$	Hadron identification
PbSc	$\|\eta\|$ <0.35	$\frac{\pi}{2} + \frac{\pi}{4}$	photon and electro detection
PbGl	$\|\eta\|$ <0.35	$\frac{\pi}{4}$	Good $e^{\pm}/\pi^{\pm}$ separation $p >$ 2GeV/c
			by EM shower and p <0.35GeV/c.
			$K^{\pm}/\pi^{\pm}$ separation up to 1 GeV/c
RxNP	1.0< $\|\eta\|$ <2.8	2π	Good reaction plane resolution
MPC	3.0< $\|\eta\|$ <3.9	2π	photon detection at forward region

2.3 Global Detector

Two sets of detectors at forward/backward rapidity are used to determine the global information of the event [65]. The geometric layout is shown on Figure. 2.3. The basic idea is to detect the physics observables of global information at a rapidity region far away from the mid-rapidity region where the analysis focus happens. The global observables include collision vertex alone the beamline, multiplicity, event centrality and reaction plane angle. These global observables help to categorize physics events in the analysis. The global detectors also provide global timing information, and are part of the PHENIX trigger system. For example, all ToF measurements rely on global timing provided by BBC.

2.3.1 Zero Degree Calorimeter (ZDC)

Two compact hadronic Zero-Degree Calorimeters (ZDC) with tungsten absorber plates are installed close to the beam pipe at a distance of 18 meters north and south of the nominal interaction point. The main purpose is to provide the information of overlapping geometry in nuclei-nuclei collisions, by measuring a clear portion of neutrons (spectators) from the nulei after collisions. Since the ZDCs are located behind the beam dipole magnets, the charged particles are bent away from the ZDCs. At ZDC, we have measurements of the deposited energy of spectator neutrons with a resolution of 20%. This energy deposition comes from the spectators and gives a direct measurement of colliding geometry.

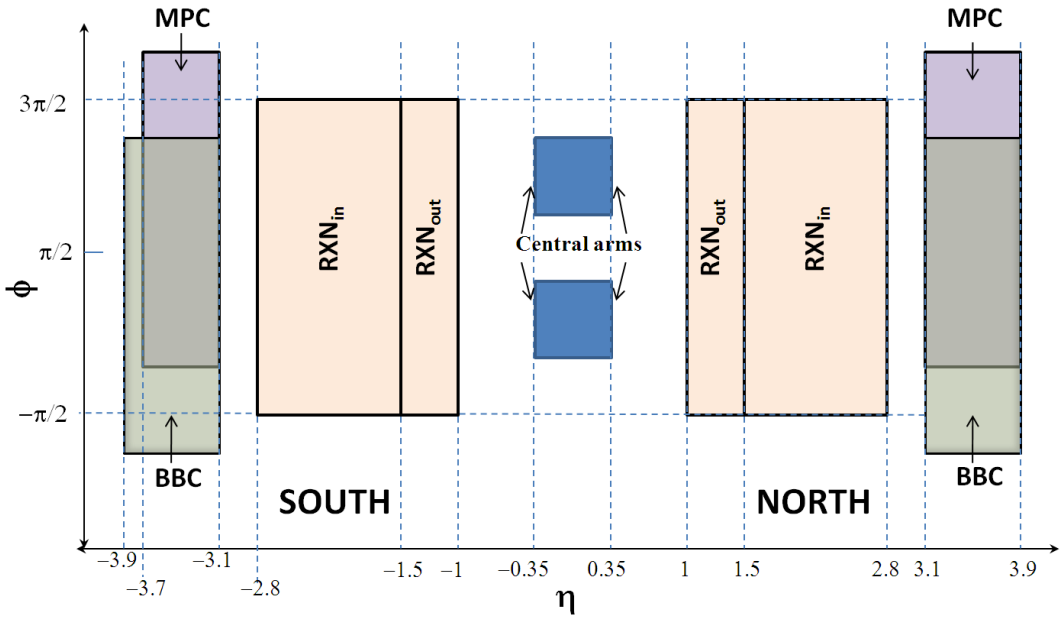

Figure 2.3: (Color online) The azimuthal angle (ϕ) and pseudo-rapidity (η) acceptance of various detectors used for RP measurement, together with the central arm acceptances for π^0 and charged hadron measurement. All RP detectors have full coverage in azimuth. The BBC and MPC are artificially shifted to improve the visibility.

2.3.2 Beam-Beam Counter (BBC)

The Beam-Beam Counters (BBC) are installed at both north and south sides of the collision zone. The north BBC and south BBC are located at 144 cm away from the center of the interaction point and cover a pseudo-rapidity range of 3.0-3.9 and the full azimuth. The main role of BBC for physics experiment is to provide the trigger signal, the collision vertex point, the global timing, the centrality and the azimuthal angle of the reaction plane. Each counter consists of 64 one-inch diameter mesh-dyode photomultiplier tubes with 3 cm quartz on the head of the PMT as a Cherenkov radiator.

The collision time and vertex position are reconstructed from the arrival

time of leading charged particles at north and south BBC. The systematic shifts caused by the time walk of the discrinator and time offset are adjusted for each individual BBC tubes. The collision time (T_0) and vertex position (z_{vtx}) are calculated by,

$$T_0 = (T_{BBCN} + T_{BBCS})/2 \tag{2.1}$$

$$z_{vtx} = c \cdot (T_{BBCN} - T_{BBCS})/2 \tag{2.2}$$

where T_{BBCN} and T_{BBCS} are the corrected average timing and c is the speed of light. The typical timing resolution of BBC is 40 ps, and position resolution of collision is 0.6 cm. Another important function of BBC for centrality determination will be discussed in section 3.1.

2.3.3 Reaction Plane Detector (RxNP)

Figure 2.4 schematically shows the components of the reaction plane detector. The RxNP [69] has two sectors, north and south sitting at the rapidity window of $1.0 < |\eta| < 2.8$. On each side, there are two rings, inner (RXNi $1.5 < |\eta| < 2.8$) and outer (RXNo $1.0 < |\eta| < 1.5$). Each ring is divided into quadrants, composed of 12 plastic scintillators and PMTs. A lead converter is placed in front of the scintillators to increase the multiplicity and energy deposition to increase the reaction plane resolution. Compared to the rapidity window of BBC ($3.0 < |\eta| < 3.9$), RxNP is closer to the collision region and gains more statistics and stronger flow signal.

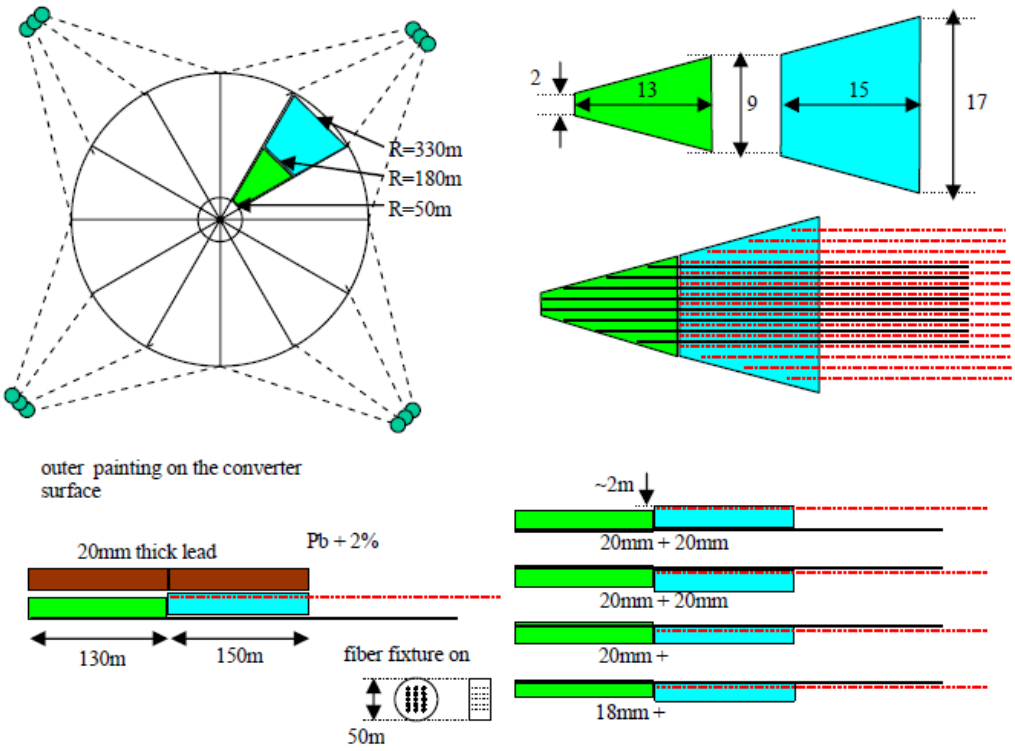

Figure 2.4: Front view of RxNP: top left shows one of the north/south arms. It is divided into 12 azimuthal segments.

2.3.4 Muon Piston Calorimeter (MPC)

The Muon Piston Calorimeter (MPC) [70] is electromagnetic calorimeters built from $PbWO_4$ scintillating crystals and avalanche photodiodes (APD) which sit in the north and south piston holes of the muon magnets of PHENIX. The acceptance in the south (north) is approximately -3.7 $< \eta <$ -3.1 (3.1 $< \eta <$ 3.9). The muon piston holes are cylindrical with a depth of 43.1 cm and a diameter of 42 cm. The small size of the area, proximately to the interaction point, and sizable magnetic fields enforce tight constraints on the calorimeter's design, requiring a compact material with short radiation length

and small moliere radius and a readout that is insensitive to the magnetic fields. MPC South is equipped with 192 crystals of size 2.2×2.2×18 cm^3 in the south piston hole. MPC sits at the similar rapidity window as BBC, but with larger multiplicity, because it can detector both charged and neutral particles. MPC is expected to improve reaction plane resolution.

2.4 Tracking and Particle Identification

The PHENIX central arm detector system [66] consists of tracking systems for charged particles and electromagnetic calorimeter for neutral particles. The particle tracking system reconstructs the track from the collision vertex, and measures the momentum of the charged particles. The electromagnetic calorimeter identifies the particle ID of neutral particles and measures their energy.

2.4.1 Drift Chamber and Pad Chamber

The PHENIX Drift Chambers are of cylindrical shape and located at the region from 2-2.4 m in radial direction from the beam axis. Their length is 1.8m along the beam direction. Each DC covers 90° in azimuthal angle and consists of 40 planes of sensing wires subdivided into 80 drift cells, each spanning 1.125° in azimuth. The wire planes are arranged in six types of wire modules stacked radially in the following order, X1, U1, V1, X2, U2, V2. Each of the X, U and V modules contains 12 and 4 sense wires, respectively. X wires measure trajectories of the charged particles in the $r-\phi$ direction with a track finding efficiency of $> 99\%$ and a two-track resolution of 2 mm. U and V wires

provide measurement of the z-coordinate.

The Pad Chambers are multiwire proportional chambers. They consist of a wire plane, enclosed in a gas volume by two cathode walls. One of the cathode planes is sub-structured into pixels with pad readout, the other consists of an etched copper layer. The cathode panels have a sandwich structure that provides sufficient strength so that little to no additional frame support is needed. This design results in a greatly reduced radiation length, keeping the creation of conversion electrons to a minimum. The operating gas for the Pad Chamber is a 1:1 mixure of argon and ethane. Three separate Pad Chamber planes, covering a total area of 88 m^2, are used to determine three dimensional hit information for charged particle tracks. The first plane (PC1) at radial distance of 2.5 m is mounted to the Drift Chamber. The third Pad Chamber plane (PC3) is located 4.9 m away from the beam pipe between the RICH and EMCal detectors (see Figure 2.2). Track projection from the DC to PC3 plays an important role in background rejection. The PC1 and PC3 planes are present in both arms, while the second plane (PC2) is only installed in the west arm at a radial distance of 4.2 m behind the RICH detector.

2.4.2 Electromagnetic Calorimeter (EMCal)

The Electromagnetic Calorimeter (EMCal) consists of two subsystems. Six sectors of lead-scintillator (PbSc) detectors and two sectors of lead-glass (PbGl) detectors cover the full central arm acceptance of PHENIX. Both set of detectors have been designed to measure electrons and photons with excellent timing, position and energy resolution. The detailed energy calibration will

be discussed in next chapter.

PbSc

The lead-scintillator (PbSc) [67] electromagnetic calorimeter for the PHENIX experiment is a shashlik type detector consisting of 15552 individual towers and covers an area of approximately 48 m^2. The calorimeter is used to measure electron and photon production in relativistic heavy ion collisions at RHIC, and is an integral part of the particle identification and trigger system for PHENIX. The calorimeter has a nominal energy resolution of $8\%/\sqrt{\mathrm{E(GeV)}}$ and intrinsic timing resolution better than 200 ps for electromagnetic showers.

Each tower is composed of 66 sampling cells consisting of alternating tiles of lead and scintillator. These cells are optically connected by 36 fibers to collect the light to phototubes at the back of towers. Four towers are mechanically brought together, and form a module (Figure 2.5). 36 modules are attached to a backbone and held together by welded stainless steel skins on the outside to form a rigid structure called a super-module. 18 super modules make a sector, a 2×4 m^2 plane with its own rigid steel frame.

The energy resolution of PbSc is obtained by the beam test at AGS and SPS. The resolution is given by a formula as following [68]:

$$(\frac{\sigma_E}{E})_B = 4.5\% \oplus \frac{8.3\%}{\sqrt{E(GeV)}}. \tag{2.3}$$

PbGl

The lead-glass (PbGl) calorimeter consists of 9216 towers, previousely commisioned in CERN experiment WA98. Each PbGl sector comprises of 192

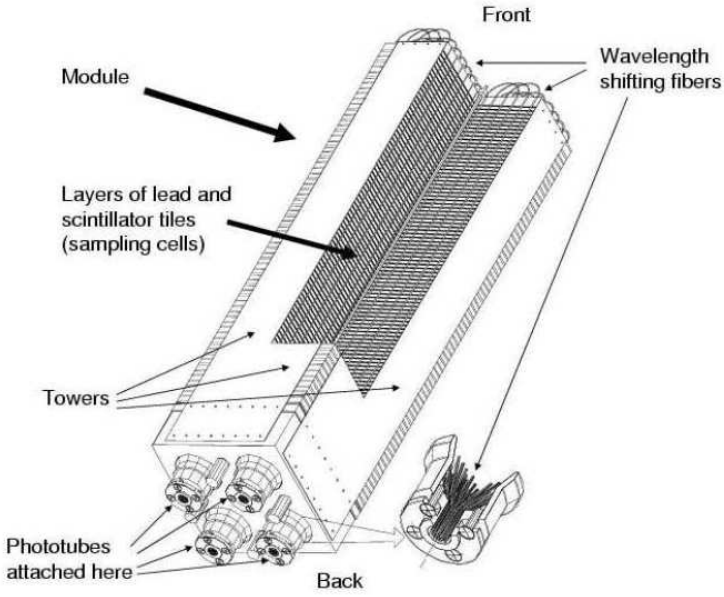

Figure 2.5: Interior view of a PbSc module.

super-modules, each consisting of 24 modules. Figure 2.6 shows the mechanical design of one super-module. The response of the PbGl has been studied in

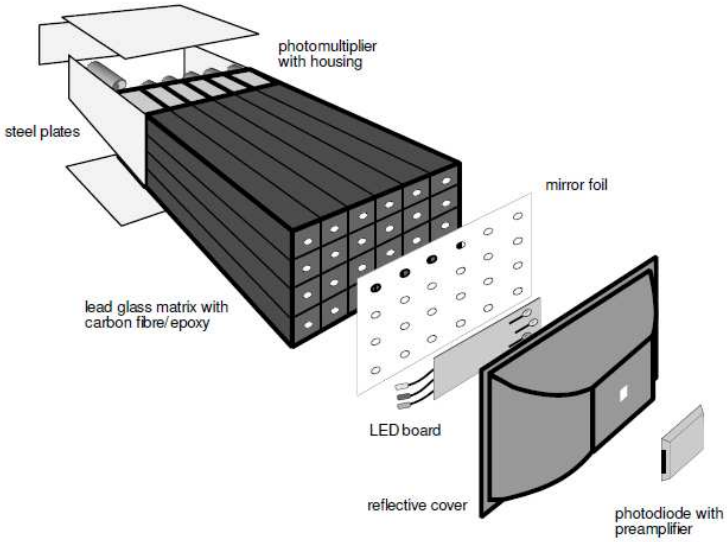

Figure 2.6: Interior view of a PbGl module.

test beams at the AGS and SPS. The energy resolution of e^+ showers versus the

incident energy is obtained by the fitted parameter results of test beams **??**,

$$\frac{\sigma(E)}{E} = 4.3\% \oplus \frac{7.7\%}{\sqrt{E(GeV)}}. \tag{2.4}$$

Chapter 3

Data Calibration

After reconstructing event and particle data from the raw signals of the detectors, there are three important calibrations steps for this analysis: centrality calibration, reaction plane calibration, and EMCal energy calibration.

3.1 Centrality Determination

3.1.1 Monte Carlo Glauber Model

Before going into the details of centrality determination, we first introduce a simple but important simulation of heavy ion collision, the Monte Carlo (MC) Glauber model [71]. The Glauber model is based on a simple geometrical picture of a nucleus-nucleus collision. Nucleons are assumed to travel on straight line trajectories, independent of whether they collide with other nucleons or not. After a nucleon is struck by another nucleon, one has a highly excited baryonic object. It is assumed in the Glauber model that the cross section for the interaction of this excited object with other ground state or

excited nucleons is identical to the ordinary inelastic nucleon-nucleon cross section σ_{nn}.

Quantities in the Glauber model can be calculated based on analytic expressions. However, modeling e.g. smearing effects introduced by the experimental centrality selection is much easier in a Monte-Carlo (MC) framework. In the MC framework the nucleons of the two Au nuclei are distributed in space according to the Wood-Saxon nucleon density profile:

$$\rho(r) = \frac{\rho_0}{1 + e^{\frac{r-R}{a}}} \tag{3.1}$$

An impact parameter b of the nucleus-nucleus collision is chosen randomly. A collision of two nucleons takes place if their distance d satisfies

$$d < \sqrt{\sigma_{nn}/\pi}. \tag{3.2}$$

A participant is defined as a nucleon that has suffered at least one inelastic nucleon-nucleon collision. The number of participants N_{part} is frequently used to characterize the centrality of a nucleus-nucleus collision.

We calculate three oftenly used eccentricities of the overlap region, $\langle\epsilon_{std}\rangle$, $\langle\epsilon_{rp}\rangle$, $\langle\epsilon_{part}\rangle$:

$$\epsilon_{std} = \frac{\langle y^2\rangle - \langle x^2\rangle}{\langle y^2\rangle + \langle x^2\rangle} \tag{3.3}$$

$$\epsilon_{rp} = \frac{\sigma_y^2 - \sigma_x^2}{\sigma_y^2 + \sigma_x^2} \tag{3.4}$$

$$\epsilon_{part} = \frac{\sigma_y'^2 - \sigma_x'^2}{\sigma_y'^2 + \sigma_x'^2} = \frac{\sqrt{(\sigma_y^2 - \sigma_x^2)^2 + 4\sigma_{xy}^2}}{\sigma_y^2 + \sigma_x^2} \tag{3.5}$$

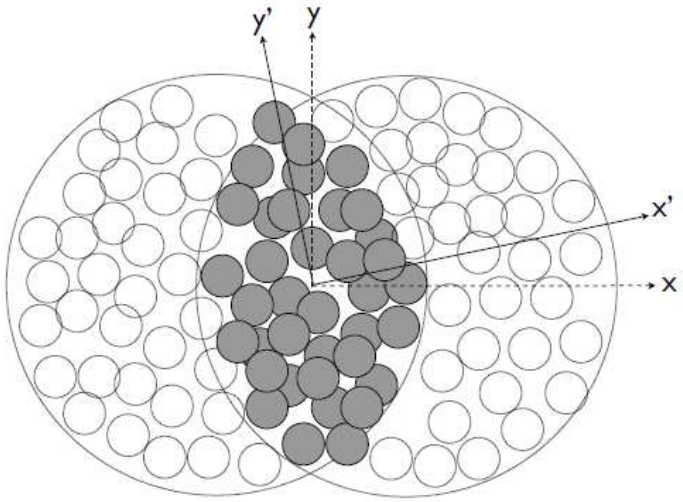

Figure 3.1: Schematic illustration of a nucleusnucleus collision in MC-Glauber model depicted in the transverse plane.

Where $\sigma_y^2 = \langle y^2 \rangle - \langle y \rangle^2, \sigma_x^2 = \langle x^2 \rangle - \langle x \rangle^2$.

3.1.2 PHENIX Minimum Bias Efficiency

In PHENIX, BBC and ZDC are used to provide the minimum bias trigger and centrality determination. Over the course of past Runs, several centrality determination methods have been developed. 1) Perp method which defines centrality by applying cut perpendicular to the BBC charge vs ZDC energy. 2) Clock-method which defines centrality by cut on the angle ϕ of a given (BBC, ZDC) value relative to a fixed origin, typically chosen to be ($0.2BBC_{max}$,0). 3) BBC-percentile method which defines centrality by cutting only on the BBC charge. Efficiency is folded in such the centrality that is defined in 0-100% range.

Perp method and Clock method have been applied in the previous Au+Au

Runs at 200 GeV prior to Run-7. BBC-percentile method was used in Au+Au 62.4 GeV, Cu+Cu at 200 and 62.4 GeV, as well as d+Au collisions. It is realized that the BBC percentile method have certain advantages over the Clock method. For example, it was demonstrated that the requirement of ZDC in the centrality definition introduces large RMS width on the N_{part} and N_{coll} in the peripheral bin.

The minimum bias trigger condition for all 200 GeV Au+Au was defined as: $bbcn >= 2 \&\& bbcs >= 2 \&\& (ZDCNS|ZDCLL1)$ (at least two hits on each side of the BBC and ZDC hits required Level 1 live bit). PHENIX has used HIJING simulation at 200 GeV Au+Au to estimate the trigger efficiency, where the simulated HIJING events were run through a GEANT simulation of the BBC response. The vertex distribution for these events was chosen to approximate what was seen during real data taking. From these events, the efficiency is estimated to be $92.3 \pm 0.4(stat) \pm 1.6(sys)$ [72].

3.1.3 Calculating Geometrical Parameters for Experimental Centrality Selections

Experimental results are normally represented as a function of "geometric" quantities such as $N_{\rm part}$ N_{coll}, etc. Therefore, it is desirable to extract mean values for these quantities for the respective classes of measured events. This is carried out via a mapping procedure involving the definition of centrality classes in both the measured and the calculated distributions; a subsequent step is then used to connect the mean values from the same centrality class in the two distributions.

The assumption underlying the BBC charge centrality classes is that the impact parameter b is a monotonic function of the average BBC charge multiplicity. That is, for large b events (peripheral) we expect low charge multiplicity, whereas for small b events (central) we expect large charge multiplicity. Once the total integral of this charge distribution is known, centrality classes are defined by binning the distribution based upon the fraction of the total integral. The same procedure can then be applied to the Glauber-based distribution obtained via a large number of Monte Carlo trials. For each centrality class, the mean value of the Glauber geometric quantities (e.g., $\langle N_{\rm part} \rangle$, $\langle \varepsilon_{\rm part} \rangle$) for the Monte Carlo events can then be calculated. As is well known, this relatively straightforward procedure is only complicated by the actual details of event selection, an uncertainty in the total measured cross section, fluctuations in both the measured and calculated distributions, as well as a finite kinematic acceptance.

To map Monte Carlo simulation onto the data, we exploit the idea that the integrated charge measured by either of the BBCs is linearly proportional to the number of participants. Linearity here means that each participant contributes equally. The number of hits in the detector is typically assumed to follow the statistics of the negative binomial distribution (NBD) [73] and the parameters μ and k of this distribution can be extracted as a function of the location of the vertex (relative to the nominal crossing point) by fitting the experimental BBC hits distribution [for each vertex interval] with a Negative Binomial Distribution (NBD) convoluted with the probability to have a given number of participants obtained with the Glauber Monte Carlo [73]. Here, μ gives a measure of the average number of hits per participant pair while k

gives a measure of the magnitude of the fluctuations. With these parameters and the assumption that the charge signal deposited in the BBC, for each hit, follows a Landau type distribution, one can map the Glauber Monte Carlo hits distributions on to the experimental ones.

In PHENIX, the NBD are used for two distinct purposes [73]:

- Together with other approaches, it provides an estimation of minimum bias trigger efficiency.
- NBD can then be used to estimate the Glauber quantities such as N_{part} and N_{coll}. In this exercise, we generate a set of Monte-Carlo Glauber events, which is then required to pass the triggering condition. The μ and k (or combined with some other procedures) should be chosen such that the fraction of events passing this cut matches the minimum bias trigger efficiency of 93%.

3.1.4 Calculating Geometric Parameters

In this study, we choose to calculate all quantities using the PHOBOS Glauber code [74] which has been released to public. We modified the package to include BBC response, such that we can simulate the BBC trigger efficiency in the standard way. For the Monte Carlo simulations the value $\sigma_{NN} = 42$ mb was used for the nucleon-nucleon cross section and the Wood-Saxon parameters for the density distribution of ^{197}Au was used:

- radius R=6.38 fm
- diffuseness d=0.535 fm

The nucleons were assumed to have no hard-core and the condition for nucleon-nucleon collision is that the inter-nucleon distance d should satisfy $\pi d^2 < \sigma_{NN}$. The input NBD parameter is $\mu = 4.00$ and $k = 1$. We call this set up as the "default settings".

In Figure 3.2, the left panel shows the Monte Carlo charge distribution obtained with the default parameter, and the right panel shows the BBC trigger efficiency as function of BBC charge. The overall efficiency is 94.2%, and efficiency loss becomes important when BBC charge < 100. Centrality classes were defined from this distribution following the procedure discussed earlier. That is, the whole distribution range is truncated to give 93% efficiency (1.2% of lower BBC charged was discard as discussed earlier), which is then cut into its respective percentiles (0-5%, 5-10%, etc) and the corresponding values for the geometric quantities are calculated.

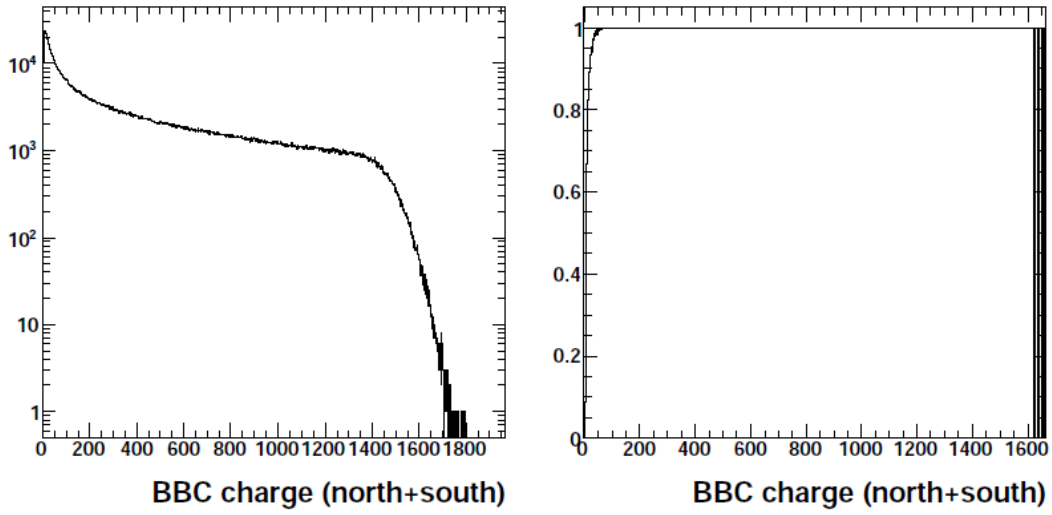

Figure 3.2: Left: Simulated BBC charge distribution. It is used to determine the centrality classes. Right: BBC trigger efficiency.

We have calculated geometric quantities for different centrality classes, which include $\langle N_{part} \rangle$, $\langle N_{ncoll} \rangle$, $\langle b \rangle$, $\langle \epsilon_{std} \rangle$, $\langle \epsilon_{rp} \rangle$,$\langle \epsilon_{part} \rangle$, the average transverse size of the overlap region $\left\langle \bar{R} \right\rangle$ and the nuclear overlap function T_{AB}.

3.1.5 Systematic Errors of Geometric Parameters

In order to estimate the systematic errors for the calculated geometric quantities, the calculations were repeated for different settings of several model parameters etc, as summarized below.

- Change the cross section to 39mb; (default is 42mb)
- Change the cross section to 45mb;
- Change the Wood-Saxon function parameters R=6.65fm, a=0.55fm; (default: R=6.38fm,a=0.535)
- Change the Wood-Saxon function parameters R=6.25fm, a=0.53fm;
- In the default calculation nucleons are allowed to overlap. In this calculation nucleons are simulated with a hard core. The radius of the hard core was taken as PHOBOS's default value, such that the distance between the centers of two nucleons is always greater than r = 0.4 fm.
- This uncertainty on minimum bias efficiency is assumed to be 93 ± 2. This uncertainty is translated into an error of the extracted quantities. For this purpose the percentiles of the cross section in the simulation were modified by a fraction 2/93, such that a slightly more central event sample was selected for each centrality class. Ncoll is e.g. determined in

the simulation for the 0-9.79% most central events instead of the 0-10% most central events.

- As in previous calculation , but a slightly less central event samples for each centrality class was selected. E.g. the 0-10.21% most central events instead of the 0-10% most central events were evaluated.

- μ, k was found to depends on the BBC z vertex, the difference between the using z dependent μ k and μ k fixed at the average value are evaluated and included as error.

- NBD with $\mu = 4.0$, $k = 1.0$ also gives 93% trigger efficiency, the difference of the resulting Glauber variable from default is evaluated.

The final systematic error of an extracted quantity for a given centrality class is the quadratic sum of all differences compared to the default calculation: $\epsilon_x = \sqrt{\sum_i (x_i - x_{default})^2}$, separately for those checks that produce systematically higher values and those produce systematically lower values, where x stands for extracted quantity. e.g. N_{coll}. Then the larger of the higher and lower systematic errors are used as the final systematic errors.

The final numbers with the associated systematic errors are documented in Table 3.1.5.

Bin %	$\langle N_{\rm part}\rangle$	$\langle N_{\rm coll}\rangle$	$\langle b\rangle$	$\langle \epsilon_{std}\rangle$	$\langle \epsilon_{part}\rangle$	$\langle \bar{R}\rangle$	$\langle T_{AB}\rangle$
	$S.E_{N_{\rm part}}$	$S.E_{N_{\rm coll}}$	$S.E_b$	$S.E_{\epsilon_{std}}$	$S.E_{\epsilon_{part}}$	$S.E_{\bar{R}}$	$S.E_{T_{AB}}$
0-5	350.8	1067	2.284	0.02635	0.08342	2.041	25.4
	(3.092	107.7	0.0746	0.003517	0.002295	0.07485	1.855)
5-10	301.7	857.8	3.949	0.08232	0.1265	1.929	20.42
	(4.665	85.45	0.1421	0.00647	0.004796	0.06779	1.446)
10-15	255.7	680.2	5.161	0.1356	0.1754	1.815	16.19
	(5.426	67.26	0.1923	0.009927	0.007756	0.06217	1.136)
15-20	216.4	538.7	6.13	0.1808	0.2211	1.709	12.83
	(5.619	52.39	0.2258	0.01019	0.008584	0.05654	0.8909)
20-25	182.4	424.4	6.96	0.2202	0.2636	1.61	10.11
	(5.743	40.37	0.2666	0.01173	0.009796	0.05234	0.7354)
25-30	152.7	330.9	7.705	0.2551	0.3037	1.515	7.879
	(5.903	32.68	0.2919	0.01181	0.01014	0.04991	0.6079)
30-35	126.8	254.7	8.385	0.2849	0.3408	1.426	6.065
	(5.945	25.78	0.3193	0.01299	0.01128	0.04706	0.5012)
35-40	104.2	193.1	9.014	0.31	0.3752	1.339	4.599
	(5.758	20.71	0.3426	0.0121	0.01141	0.04557	0.4141)
40-45	84.59	143.9	9.603	0.3319	0.4088	1.258	3.425
	(5.639	16.51	0.3798	0.01113	0.01208	0.03998	0.353)
45-50	67.73	105.4	10.15	0.3489	0.4414	1.178	2.511
	(5.405	13.5	0.4027	0.01401	0.01434	0.03776	0.2945)
50-55	53.16	75.22	10.69	0.3629	0.4771	1.099	1.791
	(4.96	10.53	0.418	0.0143	0.01493	0.03541	0.2367)
55-60	40.96	52.52	11.19	0.3713	0.5136	1.02	1.251
	(4.478	8.164	0.4369	0.013	0.01696	0.03456	0.1875)
60-65	30.77	35.67	11.69	0.3748	0.553	0.9398	0.8494
	(3.911	6.135	0.4549	0.01494	0.02084	0.04041	0.143)
65-70	22.64	23.77	12.16	0.3714	0.5978	0.8548	0.566
	(3.406	4.658	0.4844	0.01331	0.02519	0.04826	0.1091)
70-75	16.14	15.37	12.63	0.3627	0.6478	0.7558	0.3659
	(2.791	3.323	0.5007	0.01434	0.02782	0.05903	0.07832)
75-80	11.15	9.686	13.09	0.35	0.6949	0.6414	0.2306
	(2.194	2.323	0.5223	0.01565	0.02006	0.07038	0.05548)
80-93	5.601	4.193	13.92	0.3375	0.7451	0.4012	0.09984
	(0.8102	0.761	0.5059	0.00725	0.01317	0.04566	0.01837)

Table 3.1: Parameters table with systematic errors (in parenthesis) in different centralities.

3.2 Reaction Plane Calibration

3.2.1 Determine the Reaction Plane Angle

In heavy ion collisions, two nucleus with certain impact parameter b do not collide head on, leaving the overlap zone asymmetric in the azimuth plane. As illustrated in Figure 3.3, the reaction plane is defined as the plane determined by the impact parameter (x) and beam axis (z). If the medium is quickly thermalized, the pressure gradient converts the initial spatial anisotropy into final momentum space anisotropy. One can expect more particles being pushed out from the short axis (in-plane x) direction than the long axis (out-of-plane y) direction, so called anisotropic flow. It is defined as a correlation between the emitted particles and the direction of the impact parameter in a collision. In the standard method of measuring the anisotropy, the event plane method, one crucial step is to determine the azimuthal angle of the reaction plane in each event.

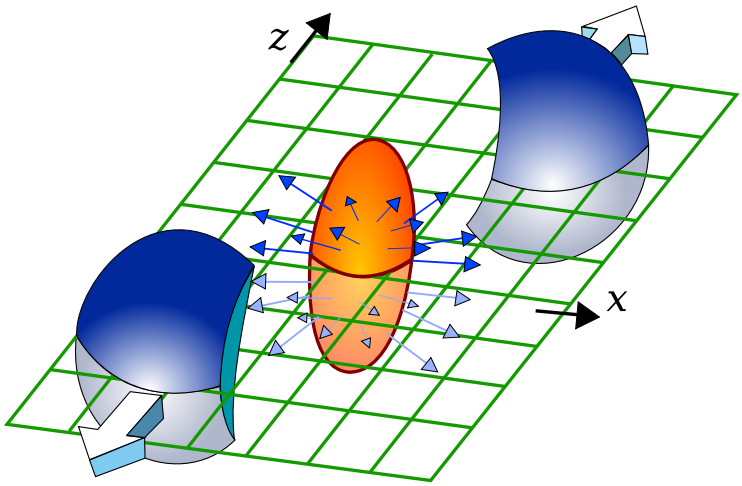

Figure 3.3: Cartoon to show the reaction plane.

Two factors are important to accurately measure the true reaction plane angle in the transverse plane: the magnitude of the anisotropic flow and the multiplicity used to determine the angle [75]. In the flow study, the particle emission azimuthal angle measured with respect to the reaction plane can be written in a form of Fourier series [75]:

$$E\frac{d^3N}{d^3p} = \frac{1}{2\pi}\frac{d^2N}{p_t dp_t dy}(1 + \sum_{n=1}^{\infty} 2v_n \cos(n(\phi - \Psi_r))) \tag{3.6}$$

where Ψ_r denotes the true reaction plane angle in the transverse plane, n denotes the order of the harmonics and the sine terms vanish due to the reflection symmetry with respect to the reaction plane.

In a given event, the event plane (measured reaction plane in experiment) can be determined independently for each harmonic of the anisotropic flow [76]. The event flow vector Q_n and the event plane angle Ψ_n from the n-th harmonic of the distribution are defined by

$$Q_n \cos(n\Psi_n) = \quad X_n \quad = \sum_i \omega_i \cos(n\phi_i) \tag{3.7}$$

$$Q_n \sin(n\Psi_n) = \quad Y_n \quad = \sum_i \omega_i \sin(n\phi_i) \tag{3.8}$$

and the n-th harmonic plane angle (Ψ_n) is calculated as

$$\Psi_n = \frac{1}{n}\tan^{-1}(\frac{Y_n}{X_n}) = \frac{1}{n}\tan^{-1}\frac{\sum_i \omega_i \sin(n\phi_i)}{\sum_i \omega_i \cos(n\phi_i)}. \tag{3.9}$$

The sums go over the i particles used in the event plane determination at forward detectors and the ω_i is the weight. In the experiment, due to the

detector granularity, we sum over all the unit cells of the detector, i.e. towers in MPC and PMTs in BBC and RxNP, with the collected charge or energy deposition as the weight. On Figure 3.4, the black curve shows the reaction plane angle distribution before the calibration. PHENIX mainly used the second order reaction plane angle ($n = 2$).

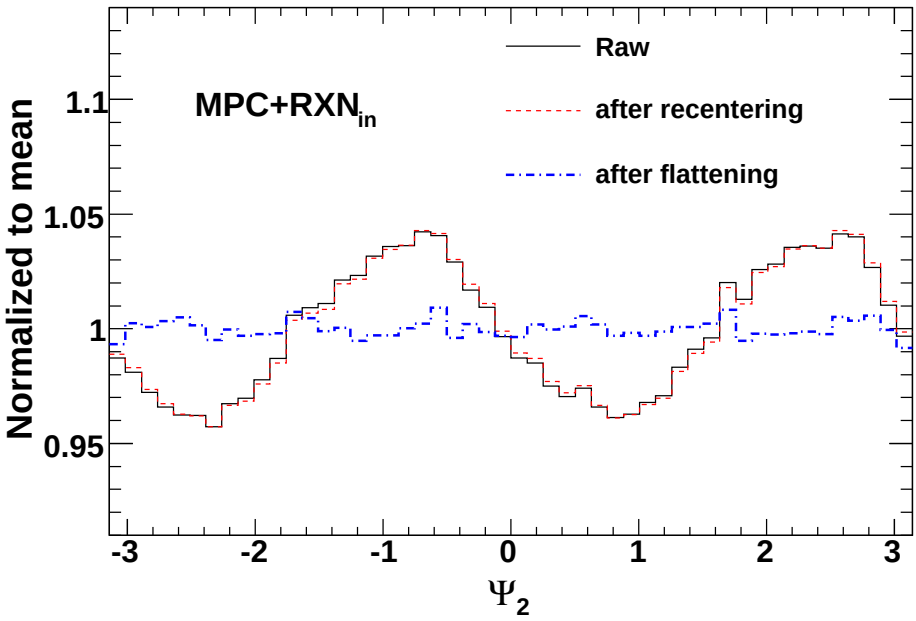

Figure 3.4: Reaction plane angle distribution. Solid: raw distribution. Dash: after re-centering. Dot-dash: after flattening.

3.2.2 Calibration

In the experiment, since the direction of the reaction plane is randomly oriented, the overall distribution of the reaction plane angle should be flat over the sample of sufficient number of events. As one can see on Figure 3.4, the measured reaction plane angle distribution (black curve) is not flat. It

is mainly due to the finite acceptance, or the anisotropic position of PMTs, or un-uniform response of the PMTs which cause the particles to azimuthally anisotropic in the laboratory system. We take two steps to remove such detector effects [76]:

- **Re-centering**:

  Normalize the distributions (X_n, Y_n) by subtracting the ($\overline{X_n}$, $\overline{Y_n}$) averaged over all the events, and dividing by the width of (X_n, Y_n);

$$X_2^{corr} = \frac{X_2 - \overline{X_2}}{\sigma_{X_2}} \tag{3.10}$$

$$Y_2^{corr} = \frac{Y_2 - \overline{Y_2}}{\sigma_{Y_2}} \tag{3.11}$$

- **Flattening**:

  Fit the unweighted laboratory distribution of the event planes, summed over all events, to a Fourier expansion and devises an event-by-event shifting of the planes needed to make the final distribution isotropic.

$$\Phi_2^{corr} = \frac{1}{2}\tan^{-1}(\frac{Y_2^{corr}}{X_2^{corr}}) \tag{3.12}$$

$$\Phi_2 \simeq \Phi_2^{corr} + \Delta\Phi \tag{3.13}$$

$$\Delta\Phi = \sum_k [A_k \cos(2k\Phi_2^{corr}) + B_k \sin(2k\Phi_2^{corr})] \tag{3.14}$$

The coefficients A_k and B_k are obtained by requiring the n-th Fourier moment of Ψ_2^{corr} distribution:

$$A_k = -\frac{2}{k} < \sin(2k\Phi_2^{corr}) > \quad (3.15)$$

$$B_k = \frac{2}{k} < \cos(2k\Phi_2^{corr}) > \quad (3.16)$$

After these two steps, the measured reation plane angle distribution is flatten as shown as the red curve on Figure 3.4. The raw distribution is only deviating by about 5% from a flat line, and most of the corrections arises from the flattening procedure.

3.3 EMCal Energy Scale Calibration

3.3.1 EMCal Clustering

When a photon deposits the energy as an electromagnetic shower or a charged particle penetrates with a ionization energy through out the calorimeter, 60-100% of the energy are observed by one tower, which is called "maximum tower". The neighboring towers are clustered together with this central tower to reconstruct the deposited shower. The reconstruction procedures are described as follows [77]:

1. At first, a noise threshold of 10 MeV is applied for each tower. The towers which share at least same edge on each other are gathered into an isolated cluster.

2. Find a "local maximum tower" which contains the maximum amplitude in 3×3 around towers and satisties the additional energy threshold (80 MeV). The towers in 5×5 around the local maximum towers are called "peak area".

3. If there is a tower with contribution to two or more peak areas, the tower energy is divided into each peak areas according to the parameterized shower profile, and recognized as split clusters if they pass the shower profile test.

4. Redefine the cluster area as "core cluster" by the towers which contains more than 2% of energy sum in the beloning peak area.

Reconstruction of Hit Position

The impact position of a particle based on the center of gravity with a correction by a hit angle. The center of gravity is given by

$$x_{cent} = \frac{\sum_i E_i x_i}{\sum_i E_i} \tag{3.17}$$

$$y_{cent} = \frac{\sum_i E_i y_i}{\sum_i E_i} \tag{3.18}$$

where (x_i, y_i) is the position within a sector of the i-th module of the cluster and E_i is its energy ($E_{tot} = \sum_i E_i$). In the experiment, the center of gravity does not correspond to the hit position because shower development angle depends on the angular incidence. The relation between the center of gravity (x_{cent}, y_{cent}) and true hit position (x_{true}, y_{true}) is studied with the test beam data,

$$x_{true} = x_{cent} - (1.05 + 0.12 \ln E_{tot}) \sin^2 \alpha_x \tag{3.19}$$

$$y_{true} = y_{cent} - (1.05 + 0.12 \ln E_{tot}) \sin^2 \alpha_y \tag{3.20}$$

with

$$\sin \alpha_x = \frac{v_x}{\sqrt{v_x^2 + v_z^2}} \tag{3.21}$$

$$\sin \alpha_y = \frac{v_y}{\sqrt{v_y^2 + v_z^2}} \tag{3.22}$$

where (v_x, v_y, v_z) is defined as the vector from collision vertex to the center of gravity. Figure 3.5

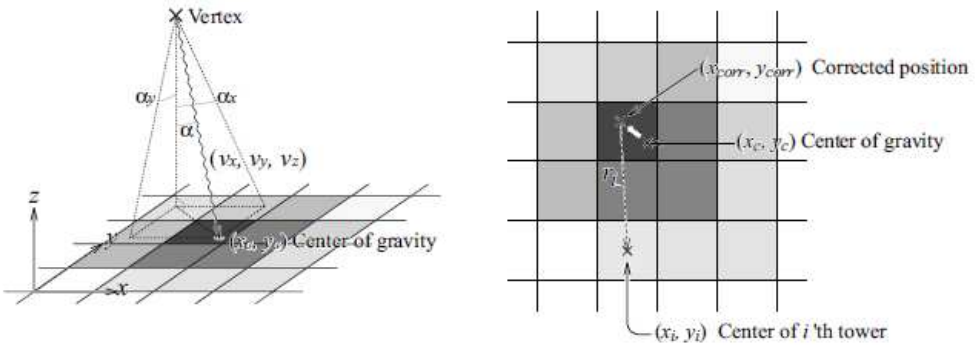

Figure 3.5: Definitions of vectors and impact angles. The impact position is corrected with the test beam data. The amplitude of each tower is represented by gray scale.

Reconstruction of Energy

The hit occupancy of the EMCal is extremely high due to the large mulitiplicity of charged particles and photons in the heavy ion collisions. It is about 15% for the PbSc in the most central Au+Au collisions at $\sqrt{s_{NN}} = 200$ GeV. In such extreme condition, the deposited energy in a cluster can be easily affected by other clusters unlike at the test beam. For instance, the observed ionization energy for the minimum ionizing particles increase by $\sim$ 6% in central Au+Au collisions. In order to make the bias caused by the high multiplicity condition small, it was proposed to sum only a few towers, instead of taking all towers, for energy measurement. A few towers are named as "core" towers. This idea comes from the fact that about 80% of the energy deposits on only one tower when a photon hit on the center of the tower. This technique of taking only the "core" towers enables EMCal to suvive such extreme condition

in the heavy ion collisions. The E_{core} energy of a cluster is defined as

$$E_{core} = \sum_{i}^{core} E_i^{meas}, \tag{3.23}$$

where E_i^{meas} is the measured energy in i-th tower and $\sum_i^{core}$ is the sum of the "core" towers. The "core" towers are defined by the following conditions:

$$\frac{E_i^{pred}}{E_{all}^{meas}} > 0.02, \text{ and} \tag{3.24}$$

$$E_{all}^{meas} = \sum_{i}^{all} E_i^{meas} \tag{3.25}$$

where E_{all}^{meas} is the sum of measured energy in all towers belonging to the "peak-area" clusters, E_i^{pred} is the predicted energy using the shower profile in the i-th tower. The energy fraction of the E_{core} to the total energy depend on the incident angle, position and energy, as parameterized with test beam data:

$$\frac{E_i^{pred}}{E_{all}^{meas}} = p_1(E_{all}^{meas}, \theta) \cdot e^{-\frac{(r/r_0)^3}{p_2(E_{all}^{meas}, \theta)}} + p_3(E_{all}^{meas}, \theta) \cdot e^{-\frac{r/r_0}{p_4(E_{all}^{meas}, \theta)}} \tag{3.26}$$

where r is the distance between the center of tower and the center of gravity, r_0 is the size of unit EMCal tower (5.54 cm for PbSc), θ is the angle of incidence with respect to a perpendicular on the detector surface, and $p_i(E, \theta)$

are parameterized to:

$$p_1(E,\theta) = 0.59 - (1.45 + 0.13\ln E)\sin^2\theta, \quad (3.27)$$

$$p_2(E,\theta) = 0.26 + (0.80 + 0.32\ln E)\sin^2\theta, \quad (3.28)$$

$$p_3(E,\theta) = 0.25 + (0.45 - 0.036\ln E)\sin^2\theta, \quad (3.29)$$

$$p_4(E,\theta) = 0.42 \quad (3.30)$$

For example, Figure 3.6 shows a profile of expected shower energy fraction in towers in the case of perpendicular hit of photon on the center of a tower. The average number of towers belonging to the "core" towers is 4 towers in this case. The E_{core} contains 91.8% energy of the total energy on average. Such an E_{core} energy represents an estimate of the true energy of a photon impinging on the PbSc unbiased by background contributions from other particles produced in the same event and depositing energy in the neighborhood of a given cluster.

3.3.2 Energy Calibration

The calibration of energy scale is one of the most important tasks for the measurement of π^0 and photon, because a few % deviation of the energy scale corresponds to the large change in the invariant yield due to the steeply falling spectra.

In the past, PHENIX has used minimum ionizing charged particles (MIP) method to calibrate the energy scale. In Run-7, due the energy cutoff in the reconstructed CWG dataset, we can not check the MIP peak [77]. Instead, we

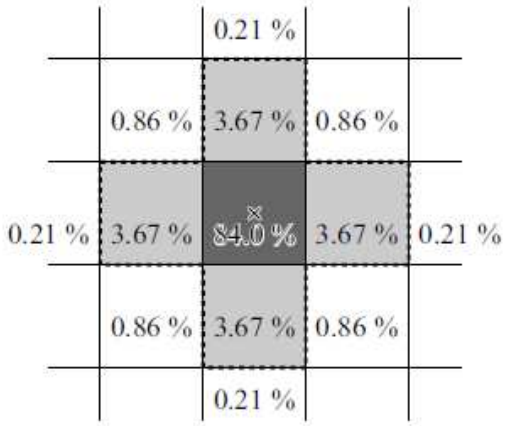

Figure 3.6: An example of expected shower energy fraction in towers in the case of perpendicular hit of photon on the center of a tower. Surrounded five towers by dotted lines are used for E_{core} calculation.

used π^0 and slope method to recalibrate the energy scale for this analysis.

π^0 method

The basic idea of using π^0 is that the invariant mass of decay photon pairs from a π^0 would have an invariant mass equal to the π^0 mass. The invariant mass is assumed to be evenly divided into two decay photons. The correction factor for measured cluster energy is extracted from the ratio between measured invariant mass peak position and the nominal π^0 mass. The procedures are described as follows:

1. Calculate the invariant mass of cluster pairs in an event. Fill the invariant mass histogram of the target tower. The cuts used are:

   - Cluster shower shape $\chi^2 < 3$.
   - Minimum p_T in the target tower: > 0.8 GeV/c

- Minimum p_T in the associated tower: > 0.2 GeV/c
- Minimum p_T of the clusted pair: > 1.0 GeV/c
- Asymmetry $(\frac{|E_1-E_2|}{E_1+E_2}) < 0.8$
- Event centrality > 40 to reduce the combinatoric background.

2. Fit the π^0 peaks of each tower with Gaussian+polynomial function to extract the peak position and width.
3. The energy scale correction factor is calculated as $c = \frac{0.135GeV}{position}$
4. Apply the correction factors to each tower, and recalculate the energy of each cluster. Iterate last four steps until the results converge.

The iteration procedures are automatically applied to over 25,000 individual towers. Sometimes the method failed to pick up the right π^0 peak position due to limited statistics, or the tower itself is dead/hot that can not be calibrated. Those examples are shown on Figure 3.7. The towers are grouped into three categories: 1) good towers (π^0 fitted well); 2) mis-calibrated (wrong peak location picked up by the fitting procedure); 3) bad towers (dead or hot). The second one can be recovered by the slope method.

Slope method

In this method, the calibration of energy depends on the slope of the tower energy spectra and the position of the tower in each sector. The steps are summarized as follows:

- Fit the E_{core} distribution of every tower in 1-2 GeV/c range with the exponential function $(p_0 e^{-p_1 * E})$, with the inverse exponential slope $1/p_1$

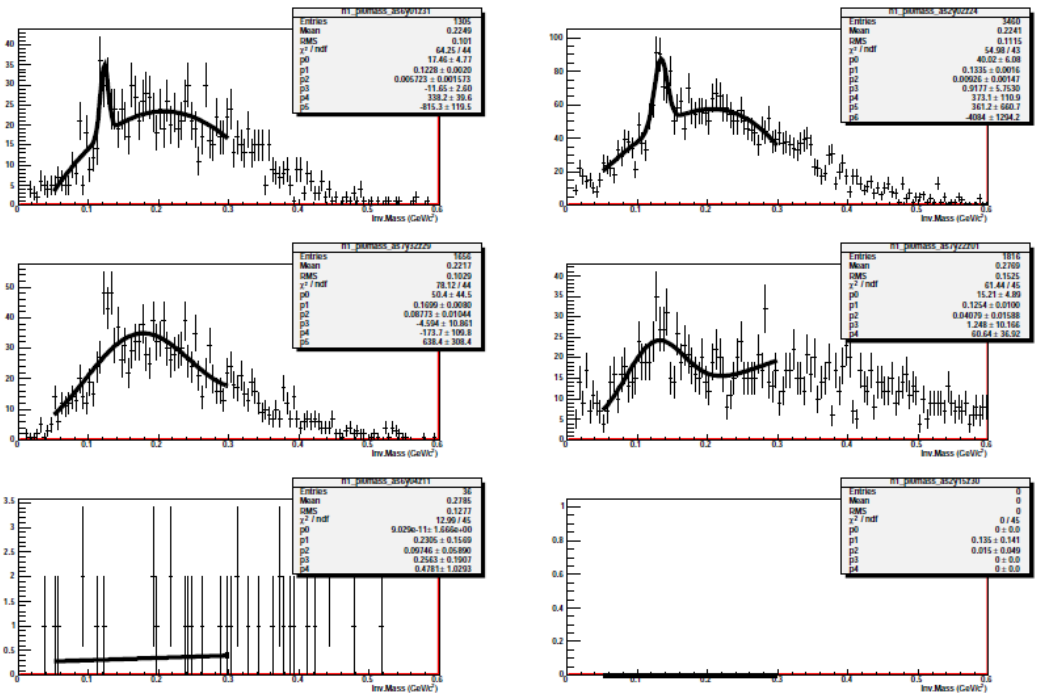

Figure 3.7: Examples shown how π^0 method works. The top two show the examples of fitting π^0 peak well, while it failed in middle two figures. The bottom two are regarded as bad towers.

representing the average energy of the tower. The example of the fit is shown in Figure 3.8

- Extract the position dependence of the tower's average energy, Figure 3.9, which takes care of the incident angle dependence of the energy deposition.

- The correction factor of each tower is defined as

$$c = \frac{\text{functional vaule(as parameterized in Figure3.9)}}{\text{individual tower value}}. \tag{3.31}$$

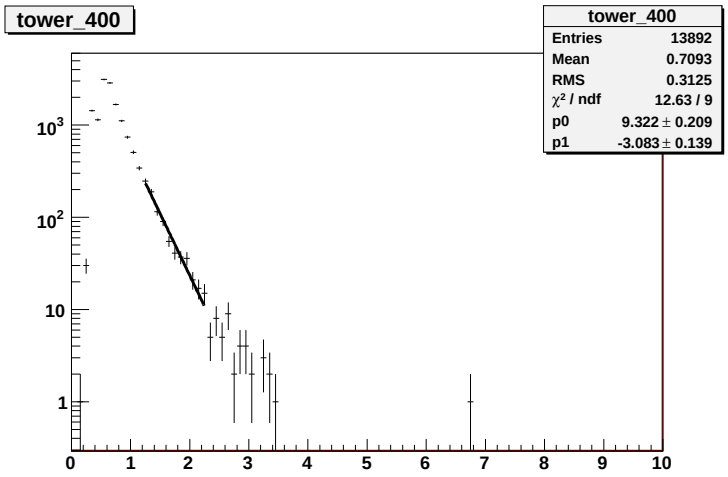

Figure 3.8: The example of fitting the tower's E_{core} distribution with the function $f(E) = p_0 e^{p_1 E}$, where p_1 is the slope. $1/p_1$ is the average energy of the tower.

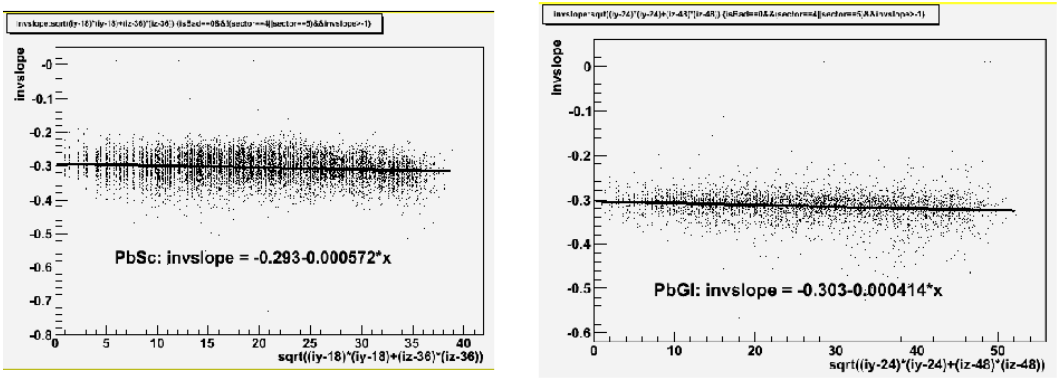

Figure 3.9: The parameterization of average energy of towers as function of the position for PbSc and PbGl.

Figure 3.10 shows the comparisons of extracted π^0 peak positions after applying two sets of calibration constants. A large amount of the towers can be recovered by slope method which does not require a large statistics. Table. 3.2 summarize the number of towers recovered by different methods.

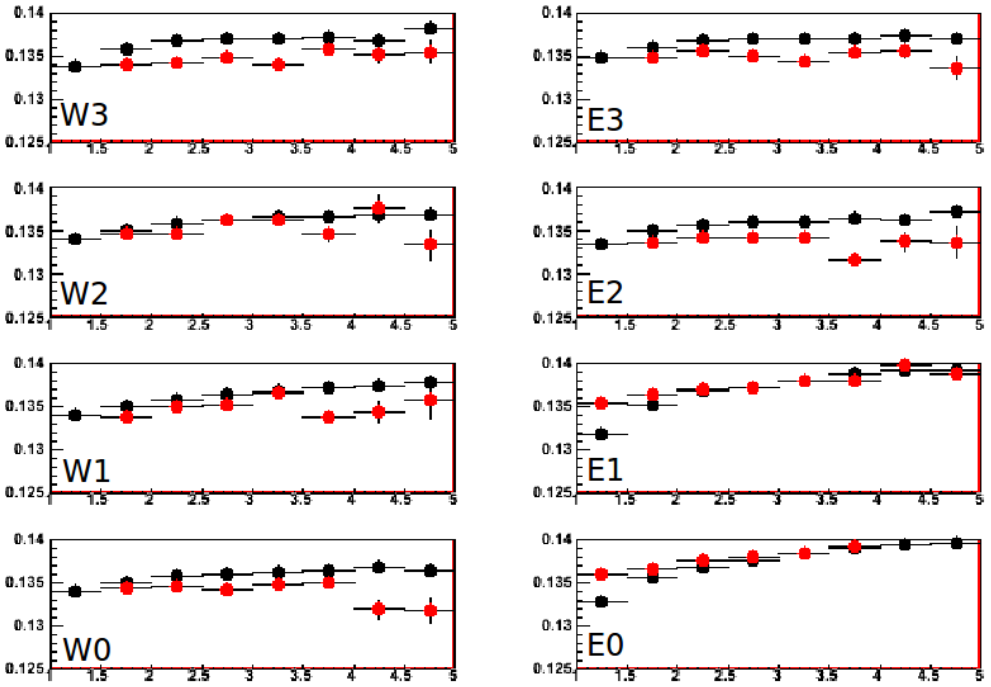

Figure 3.10: The comparisons of extracted π^0 peak position as function of p_T after applying two calibration methods. Black: π^0 method; Red: slope method.

Sector	π^0 method	Slope method	Bad towers	Total
W0	2247	341	4	2592
W1	2231	347	14	2592
W2	2258	304	30	2592
W3	1669	540	383	2592
E0	2170	2208	230	4608
E1	2678	1838	92	4608
E2	2170	348	74	2592
E3	2023	477	92	2592

Table 3.2: Summary of the number of calibrated towers of PHENIX EMCal in Run-7.

The performance of the energy scale calibration can be checked by looking at at the relative width of the π^0 peak ($\frac{\pi^0 \text{ width}}{\pi^0 \text{ position}}$) before and after the calibration. The results are shown in Figure 3.11. The energy resolution is greatly

improved after this calibration.

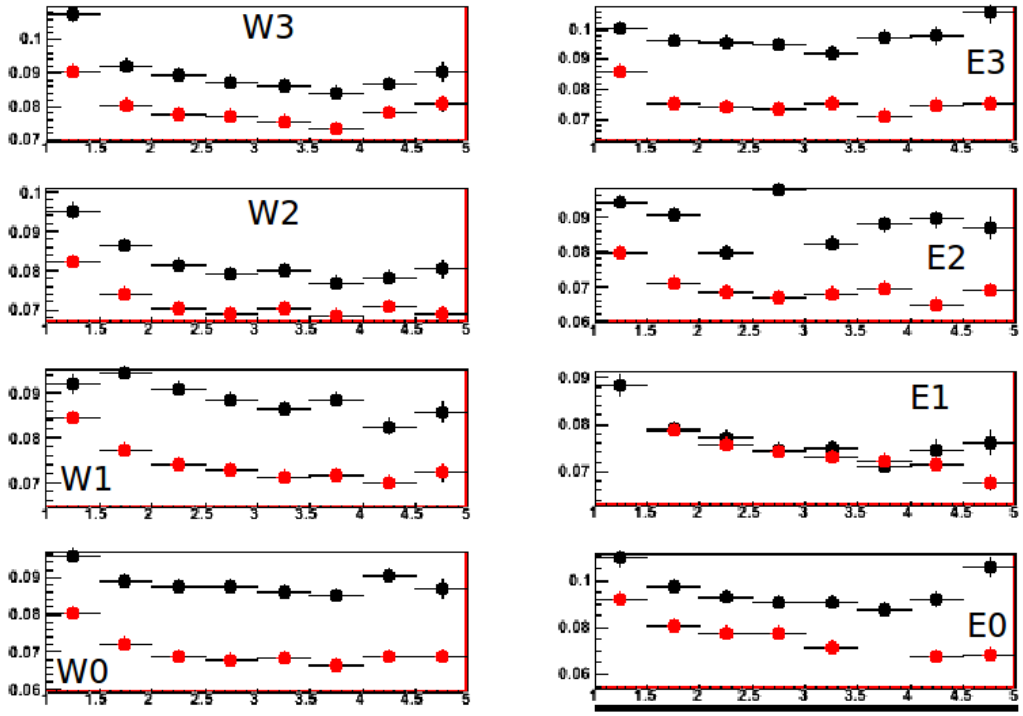

Figure 3.11: The relative width of π^0 peak for eight sectors as function of p_T before (black) and after (red) the calibration. The resolution is greatly improved.

Chapter 4

Data Analysis

In this chapter, the detailed procedures and methods to obtain the azimuthal anisotropy of π^0 in Au+Au collisions are discussed. They include 1) π^0 Reconstruction; 2) methods to study the anisotropy; 3) analysis details, such as event selection, variable cuts, systematic errors, etc.

4.1 Reaction Plane Resolution

As mentioned previously, the azimuthal distribution observed in heavy ion collisions can be described by a Fourier series:

$$\frac{dN}{d(\phi - \Psi_{RP})} \propto 1 + 2\sum_{n\geq 1} v_n \mathrm{cos}n(\phi - \Psi_{RP}) \tag{4.1}$$

where the coefficients are $v_n = \langle \mathrm{cos}n(\phi - \Psi_{RP})\rangle$. In PHENIX, the Ψ_{RP} is usually measured using the forward detectors, so called event plane Ψ_{EP}. Then the coefficients $v_n^{raw} \equiv \langle \mathrm{cos}n(\phi - \Psi_{EP})\rangle$ measured according to the event plane

can be written as

$$
\begin{aligned}
v_n^{raw} &= \langle \cos n(\phi - \Psi_{EP}) \rangle && (4.2)\\
&= \langle \cos n((\phi - \Psi_{RP}) + (\Psi_{RP} - \Psi_{EP})) \rangle && (4.3)\\
&= \langle \cos n(\phi - \Psi_{RP}) \rangle \langle \cos n(\Psi_{RP} - \Psi_{EP}) \rangle && (4.4)\\
&= v_n \times \sigma_n && (4.5)
\end{aligned}
$$

where $\sigma_n \equiv \langle \cos n(\Psi_{EP} - \Psi_{RP}) \rangle$ is called reaction plane resolution. The true anisotropy coefficient is the measured value corrected by the resolution factor,

$$v_n = \frac{v_n^{raw}}{\sigma_n}. \tag{4.6}$$

To estmate the reaction plane resolution factor σ_n, we use the well-known subevent method used in the past [79]. The calculation consists of measuring the orientation of reaction plane in two subevents of roughly equal size and analyze the distribution of the difference in angle between them. For the first purpose, the two detectors placed on both side of the central arm covering the same pseudo-rapidity window (north and south). If only flow correlations are present, the distribution of $\Delta\Psi \equiv \Psi_{south} - \Psi_{north}$ can be described by

$$\frac{dN}{d\Delta\Psi} = \frac{e^{-\chi^2}}{2}\left(\frac{2}{\pi}(1+\chi^2) + z[I_0(z) + L_0(z)] + \chi^2[I_1(z) + L_1(z)]\right), \tag{4.7}$$

where $z = \chi^2 \cos\Delta\Psi$ and L_0, L_1 are modified Struve functions and I_0, I_1 are modified Bessel functions. By fitting the subevent distribution with Eq 4.7 (Figure 4.1) and extract the resolution parameter χ, the resolution correction

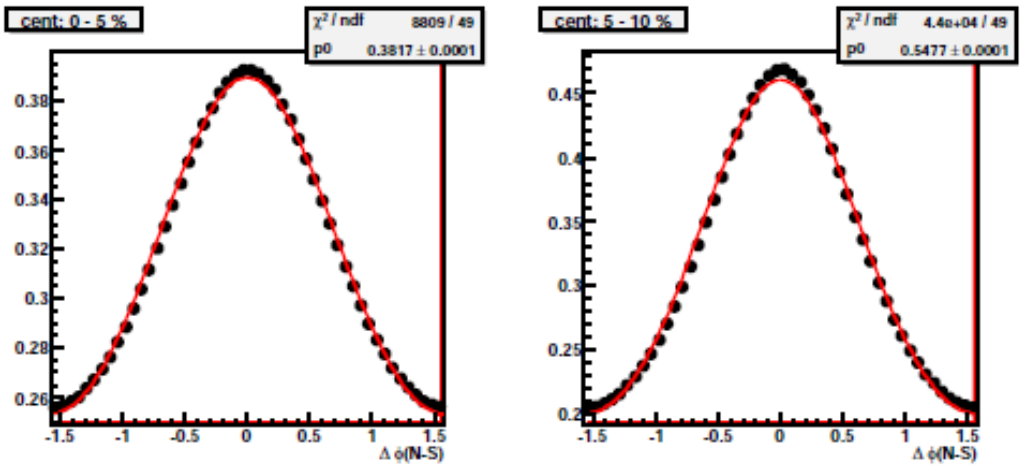

Figure 4.1: Examples showing the $\Delta\Psi \equiv \Psi_{south} - \Psi_{north}$ distribution and fitting using Eq 4.7.

factor can be obtained by

$$\langle \cos n\Delta\Psi \rangle = \frac{\sqrt{\pi}}{2}\chi e^{-\chi^2}[I_{\frac{n-1}{2}}(\frac{\chi^2}{2}) + I_{\frac{n+1}{2}}(\frac{\chi^2}{2})]. \tag{4.8}$$

In this analysis, we utilized all the available forward detectors to determine the reaction plane angle:

- BBC: $3.0 < |\eta| < 4.0$
- MPC: $3.0 < |\eta| < 4.0$
- RXNin: $1.5 < |\eta| < 2.8$
- RXNout: $1.0 < |\eta| < 1.5$

We also combined MPC and RXNin for the purpose of reducing autocorrelations due to jet bias and increasing resolutions than using them separately.

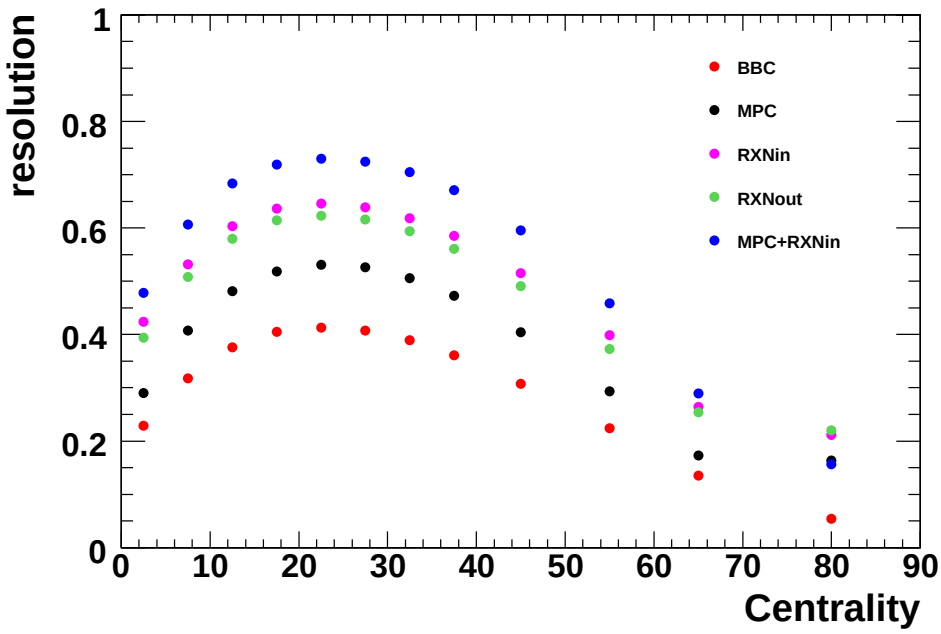

Figure 4.2: The resolution factor as function of centrality for different detectors.

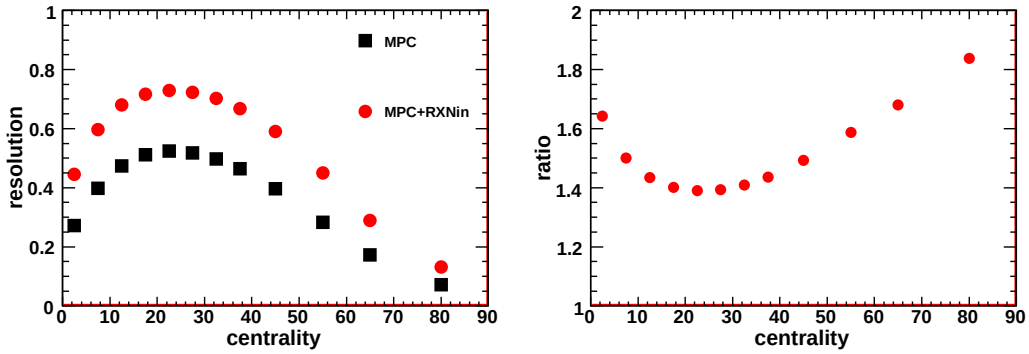

Figure 4.3: Left: resolution factor for MPC and combined MPC+RXNin; Right: the ratio of resolution of combined to MPC.

The resolution factors as function of centrality are shown in Figure 4.2.

4.2 Event and run Selection

The collision vertex z (along the beam axis) are constrained within 30 cm of the nominal crossing point.

During the running period, in order to keep data in small units over which constant calibrations can be assumed, the DAQ is started and stopped approximately for 1 hour. Each such starting and stopping is called a "run" (lower case). For Run7, there were about 850 runs which recorded physics data. In this analysis, we performed run-by-run QA based on some quantities to reject certain bad runs.

- The runs with number of events less than 500K are excluded;
- The flattness of centrality and reaction plane distributions are checked.
- To ensure the uniformity of the detector acceptance and energy calibration, a rejection criteria based on the π^0 yields per event is used to make sure the acceptance and energy calibration is stable in the analysis.

After all the run-by-run QA, 3.5 billion minimum bias events are left for this analysis.

4.3 Cluster Selection

photon

During the PHENIX data production, a moderate energy threshold cut of $E_{core} > 0.2GeV$ is applied to exclude the dust-clusters, since they can cause large combinatoric background for π^0 measurement.

Cuts based on the shower-shape are used to distinguish between showers produced by photons/electrons and hadrons, because their pattern of energy depositions are different. The analytical parameterization of the energy sharing and its fluctuations is employed for the identification of electromagnetic clusters. The χ^2 is calculated with the parameterization [77],

$$\chi^2 = \sum_i \frac{(E_i^{pred} - E_i^{meas})^2}{\sigma_i^2}, \tag{4.9}$$

where E_i^{meas} is the energy measured in tower i and E_i^{pred} is the predicted energy for an electromagnetic particle of total energy $\sum_i E_i^{meas}$. The χ^2 value characterizes how electromagnetic a particular shower is and can be used to discriminate against hadrons. The default cut to identify photons is set to $\chi^2 < 3$.

In PHENIX EMCal, the dead and noisy towers were identified offline by observing some basic quantities over the running period: the total number of hits per tower above 100 MeV, the integrated energy per tower. 5-σ low outliers were flagged as dead map, and 5-σ high outliers were considered in the warn map. The hot towers are noisy towers which passed these basic checks, but a small amount of them can increase the high p_T π^0 yields substantially, due the steeply falling spectra of particle production at high p_T. The hot towers are identified based on the hit frequency in a iteration procedure. A good cluster candidate can not be in the 3×3 vicinity of dead/warn/hot towers.

π^0

After selecting two photons, addition pair cuts are applied to the pair quantities to reduce the background.

- p_t >= 1.0GeV/c;
- Two photons should hit the same sector;
- Energy asymmetry cut: $\frac{|E_1-E_2|}{E_1+E_2} < 0.8$.

4.4 π^0 Reconstruction

Statistical subtraction method is applied to measure the π^0 yields. We form all the photon pairs in the same event over the Run-7 data set, and calculate their invariant mass($M_{\gamma\gamma}$) and the momentum ($\mathbf{p}_{\gamma\gamma}$) correspondingly:

$$M^2_{\gamma\gamma} = 2 \cdot E_{\gamma 1} \cdot E_{\gamma 2}(1 - \cos\theta), \tag{4.10}$$

$$\mathbf{p}_{\gamma\gamma} = p_1 \cdot \mathbf{n_1} + p_2 \cdot \mathbf{n_2}. \tag{4.11}$$

where $E_{\gamma 1(2)}$ is the photon energy, θ is the openning angle between two photons, and $\mathbf{n_{1(2)}}$ is the unit vector of the photon. If the two photons are decayed from a same π^0, their invariant mass would be the nominal mass of the π^0, which is $\sim$135 MeV/c^2. Due to the large multiplicity environment in a heavy ion collision, there is a significant background introduced by random combinations of different photon sources. Such background is estimated using the event-mixing technique, which takes one photon from one event, and the other photon from a similar event (in terms of similar centrality class, collision

vertex, reaction plane orientation, etc), such that the two photons from two different events are not correlated and can properly estimate the bacground shape. Figure 4.4 shows the procedures as described above to obtain the π^0 yield in the given p_T and centrality bin. In the π^0 nominal mass region ($\sim$ 135 MeV/c^2), a prominent peak can be seen sitting on top of the backgrounds (red curve). The event-mixing distribution is scaled to match the side-bands of the π^0 peak, thus gives an estimation of the backgrounds under the peak. After subtracting the background, the peak can be well described by the Gaussian function, with the peak position m_0 $\sim$135 MeV/c^2. The width reflects the energy resolution of the EMCal detectors.

4.5 Methods to Study π^0/η Azimuthal Anisotropy

In heavy ion collisions, due to the initial asymmetric shape of the overlap geometry, the azimuthal distribution with respect to the reaction plane of the emitted particles is not flat. The distribution can be decomposed into the Fourier series,

$$E\frac{d^3N}{dp^3} = \frac{1}{2\pi}\frac{d^2N}{p_t dp_t dy}(1 + \sum_{1}^{\infty} 2v_n \cos(n(\phi - \Psi_{RP}))). \tag{4.12}$$

where Ψ_{RP} is the azimuthal angle of the reaction plane. The magnitude of the anisotropy is usually charaterized by the first two orders of the Fourier coefficients, $v_n = \left\langle e^{in(\phi_p - \Psi_{RP})} \right\rangle$, n = 2, 4, ..., where ϕ_p is the azimuthal angle of an emitted particle, and the brackets denote averaging over particles and events.

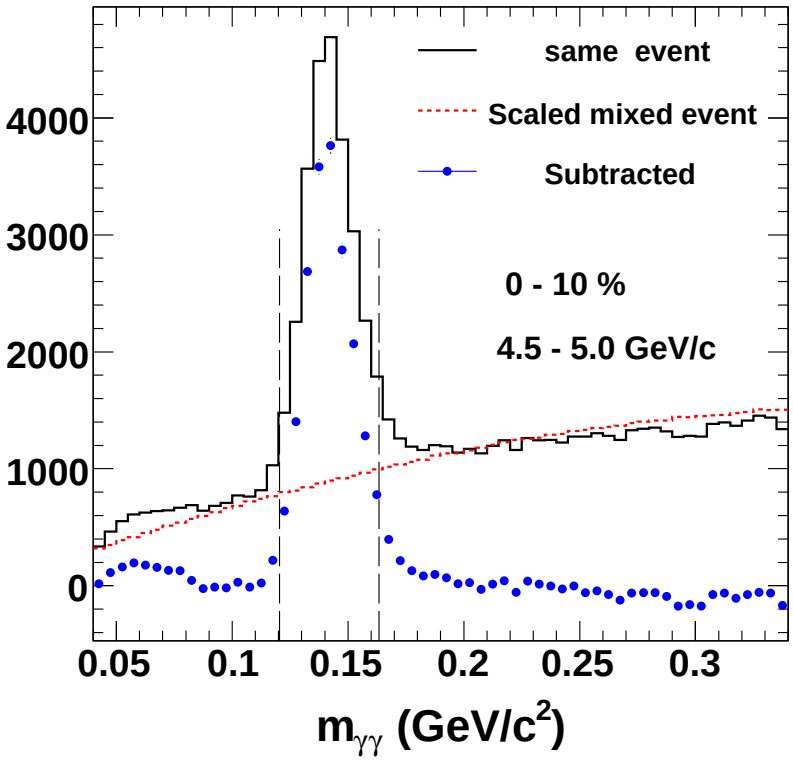

Figure 4.4: An example shows the π^0 yield extraction procedures. The lines are: invariant mass distribution of photon pairs from same event (black), mixed events (red), and the background subtracted π^0 peak (blue).

In this analysis, we use two methods to extract the $v_{2,4}$ coefficients for π^0/η in different centralities and p_T selections. In the following, we explain the methods using π^0 as an example.

4.5.1 $dN/d\phi$ Method

The main ideas of this method are to extract π^0 yields in different angular bins with respect to the reaction plane angle, and to decompose the angular distribution into Fourier basis to evaluate the anisotropy parameter $v_{2(4)}$. Usually six angular bins are used in the interval of $\Delta\phi \in (0 \rightarrow \pi/2)$, but we will show that finner binning (18 bins) gives the same result. The procedures can be described as follows:

1. Iterate over all the events.

    - In each event, determine the azimuthal angle of the reaction plane, as discussed in section 3.2.
    - Form all the photon pairs, and calculate their invariant mass, p_T and angle ($\phi_{\gamma\gamma}$), as in Eq. 4.10.
    - Fill the histogram of the invariant mass distribution for the corresponding centrality, p_T and angular bin.
    - Mix events in the similar global class (centrality, collision vertex etc), and repeat the above three steps.

2. Extract π^0 yields in each angular bin at a given centrality and p_T bin.

3. Fit the angular π^0 yields distribution with the harmonic function $f(\Delta\phi) = N_0(1 + 2v_2^{raw}\cos(2\Delta\phi))$ as shown in Figure 4.5.

4. Correct v_2^{raw} by the reaction plane resolution factor, $v_2 = v_2^{raw}/\sigma$.

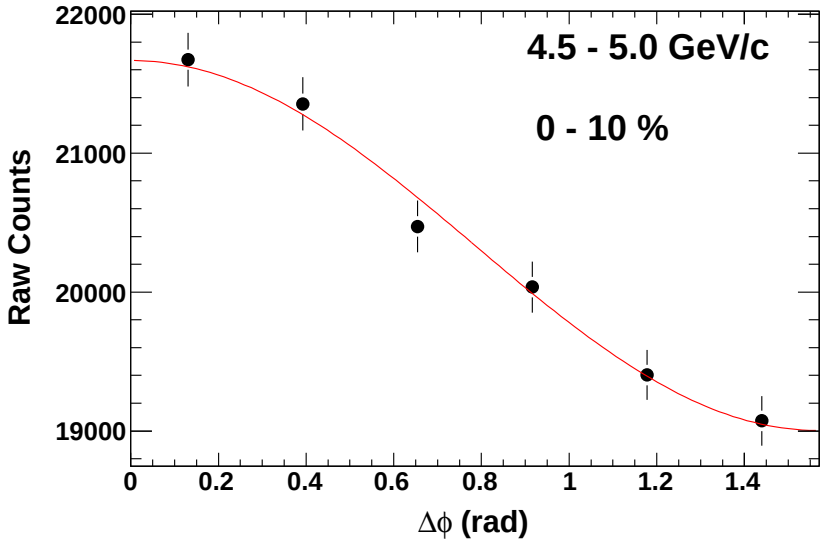

Figure 4.5: The example of $dN/d\phi$ distribution fitted by the harmonic funtion to extract the raw v_2.

4.5.2 Invariant Mass Method

In [78], the authors suggested another way to study the azimuthal anisotropy of short lived particles. In analogy to the single partile anisotropy, the distribution of partile-pair azimuthal angle can generalized into:

$$p(\phi_{pair} - \Psi_{RP}) = \frac{1}{2\pi} \sum_{n=-\infty}^{+\infty} v_n^{pair} e^{in(\phi_{pair} - \Psi_{RP})}. \tag{4.13}$$

The pair anisotropy coefficient is defined as $v_n^{pair} = \left\langle e^{-in(\phi_{pair} - \Psi_{RP})} \right\rangle$. In this analysis, the angle ϕ_{pair} is the angle of momentum vector sum of two photons. In the case of the anisotropy of a short-lived particle (A) which rapidly decays

into two daughter particles (A→B+C), the sine coefficient v_n^{pair} vanishes when the colliding system is symmetric with respect to the reaction plane.

In this method, one first sorts resonance decay candidate photons into bins of invariant masses $M_{\gamma\gamma}$. Then extract the total resonance yield, following the standard procedure. That is, one counts the number of pairs in each invariant-mass bin, let $N_{pair}(M_{inv})$ denote this number. One then separates this distribution into an uncorrelated part $N_{BG}(M_{inv})$ and a correlated part $N_{signal}(M_{inv})$ using the event mixing technique:

$$N_{pair}(M_{inv}) = N_{BG}(M_{inv}) + N_{signal}(M_{inv}). \tag{4.14}$$

Next step, define the azimuthal angle of the pair ϕ_{pair}, and carry out the analysis to extract the pair anisotropic coefficient v_n^{pair} in each invariant mass bin. Then it can be decomposed into:

$$N_{pair}(M_{inv})v_{s,n}^{pair} = N_{BG}(M_{inv})v_{s,n}^{BG} + N_{signal}(M_{inv})v_{s,n}^{signal}, \tag{4.15}$$

$$N_{pair}(M_{inv})v_{c,n}^{pair} = N_{BG}(M_{inv})v_{c,n}^{BG} + N_{signal}(M_{inv})v_{c,n}^{signal}, \tag{4.16}$$

where $v_{s,n}^{pair} = \langle \sin(n\Delta\phi) \rangle$, and $v_{c,n}^{pair} = \langle \cos(n\Delta\phi) \rangle$. This decomposition is based on the assumption that the background components $N_{BG}(M_{inv})v_{c,n}^{BG}$ are smooth functions of invariant mass M_{inv}. As mentioned above, symmetry with respect to the reaction plane for resonance particles implies that $v_{s,n}^{signal}$=0. If the background consists of uncorrelated particles, one also has $v_{s,n}^{BG}$=0.

One can extract the anisotropy coefficient v_2^{sig} directly from the fit of

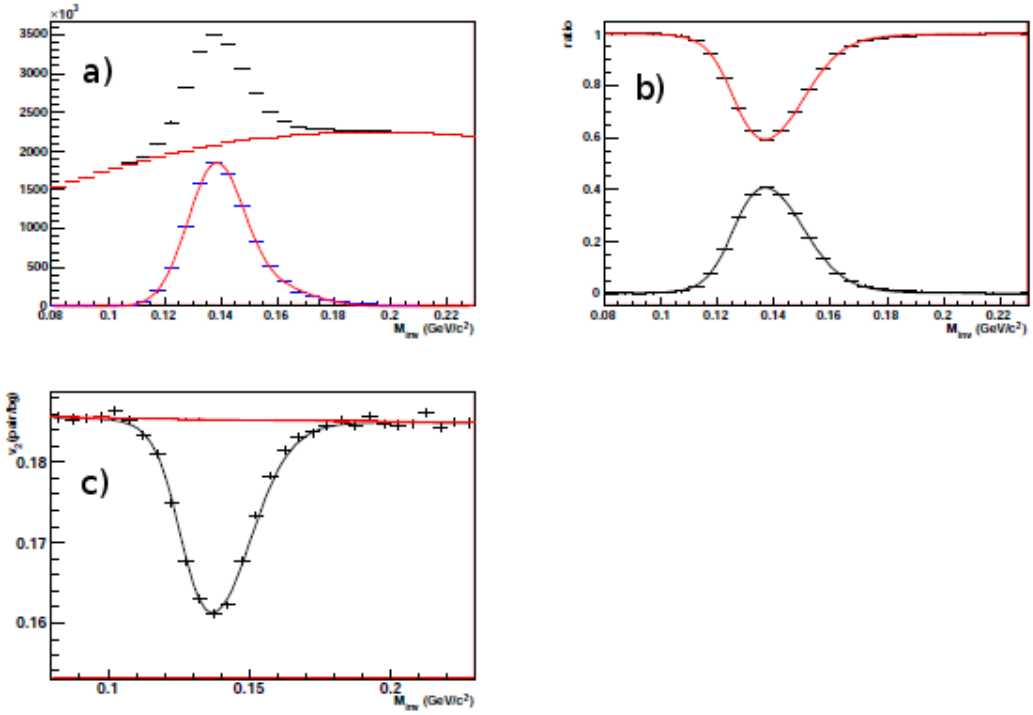

Figure 4.6: An example showing the procedures of invariant mass method in centrality 20-30% and $p_T \in$ 2.0-2.5 GeV/c. a) shows the invariant mass distributions for total pairs (black), background (red) and signal (blue fitted with pink Gaussian curve). b) shows the ratios N_{BG}/N_{pair} (red) and N_{sig}/N_{pair} (black). c) shows the fit to v_2^{pair} (black) and the red curve is the background $v_2(M_{inv})$.

$v_2^{pair}(M_{inv})$ distribution via the following the function:

$$v_{c,n}^{pair} = v_{c,n}^{sig}\frac{N_{sig}}{N_{pair}}(M_{inv}) + v_{c,n}^{BG}\frac{N_{BG}}{N_{pair}}(M_{inv}), \tag{4.17}$$

by assuming the $v_{c,n}^{sig}$ is a constant function of M_{inv}. The ratios $\frac{N_{sig}}{N_{pair}}(M_{inv})$ and $\frac{N_{BG}}{N_{pair}}(M_{inv})$ are funtions of invariant mass and they can be extracted from the fit. For the $v_{c,n}^{BG}$, one can use a polynomial function to parameterize: $v_{c,n}^{BG} = p_0 + p_1 M_{inv} + p_2 M_{inv}^2$. The example can be seen in Figure 4.6

4.5.3 Comparison of Two Methods

Figure 4.7 compares the v_2 values obtained from the two methods: $dN/d\phi$ method and invariant mass method . The v_2 values agree within the statistical errors, the systematic deviation is less than 3%.

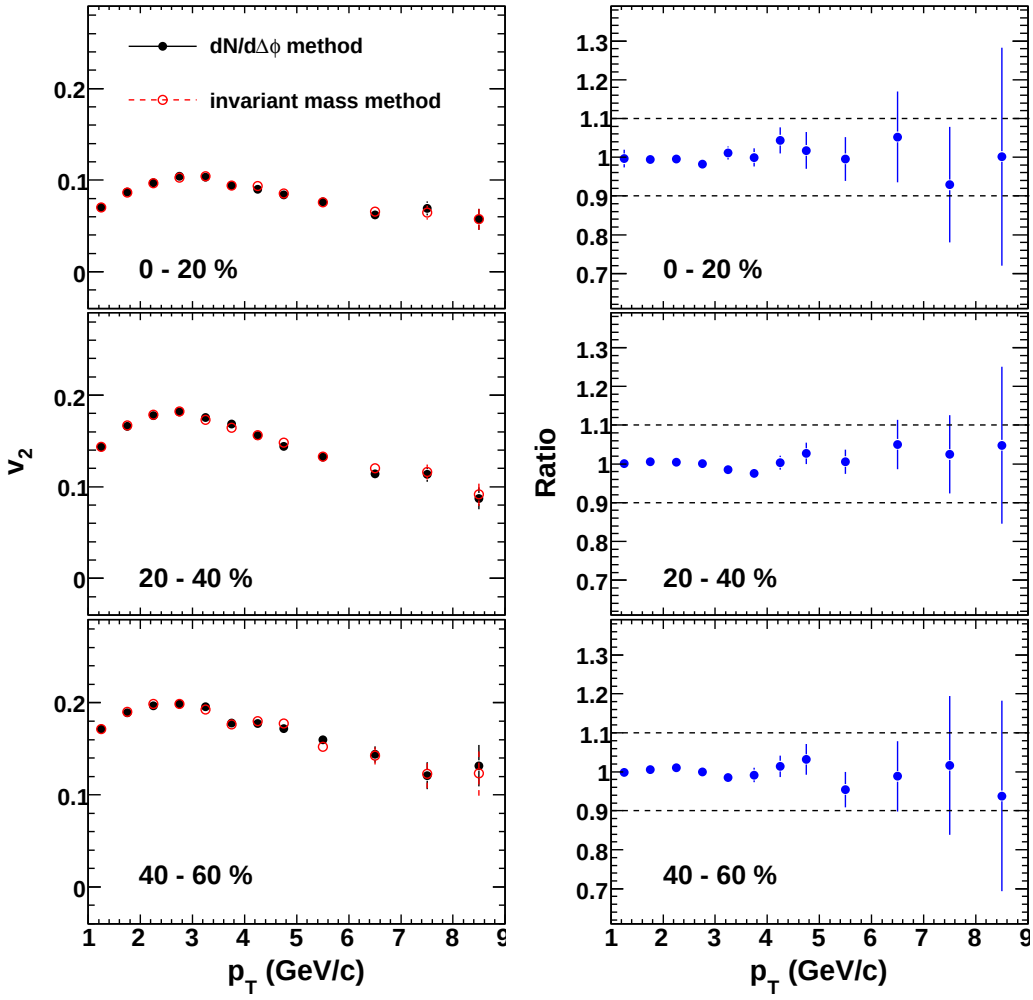

Figure 4.7: Comparisons of two methods to measure the v_2.

4.6 Discussion of Errors

4.6.1 Background scaling

To estimate the contribution to the pair mass distribution from uncorrelated pairs using the event-mixed distributions, we have to scale them appropriately. The conventional method is to choose a region away from the signal peak being measured, and match the integrals of the signal and background distributions in that region. In other words, the event-mixed distribution is scaled with the factor k:

$$k = \frac{n_{fg}}{n_{bg}}, \tag{4.18}$$

and its associated error:

$$\frac{\delta k}{k} = \sqrt{\frac{1}{n_{fg}} + \frac{1}{n_{bg}}} \tag{4.19}$$

where n_{fg} and n_{bg} are the number of counts observed in the normalization region of the signal and background, respectively. In this analysis we choose two side-band regions away from the π^0 peak to do the normalization: 0.08-0.09 GeV/c^2 and 0.2-0.23 GeV/c^2.

4.6.2 Fitting and Extraction

In order to arrive at an interval in which to integrate counts in the (subtracted) peak region, we perform a fit on the subtracted distribution. This fit has the following form:

$$F(m) = \frac{A}{\sqrt{2\pi\sigma^2}} \mathrm{e}^{-\frac{m-m_0}{2\sigma^2}} + a + bx \tag{4.20}$$

where A, σ, m_0, a, b are fit parameters. At the given centrality and p_T bin, all these parameters are allowed to vary, with the limits set on the A, σ, m_0 requiring them to be positive. The additional polynomial accounts for the residual background not subtracted with the mixed distribution. For each reaction plane angular bin, the σ and m_0 are fixed to the values taken from the RP-inclusive parameterization. The signal integration region is $[m_0 - 3\sigma, m_0 + 3\sigma]$.

4.6.3 Estimating Statistical Errors

If N is the measured number of counts in the peak region, S the number of correlated (foreground) pairs, and B the number of uncorrelated pairs, then

$$N = S + B. \tag{4.21}$$

The background B is estimated from the mixed event distribution as

$$B' = kM, \tag{4.22}$$

where M is the number of counts in the peak region of the unscaled mixed event distribution. The estimate for the number of correlated pairs is now

$$S' = N - B' = N - kM = N - \frac{n_{fg}}{n_{bg}}M. \tag{4.23}$$

We estimate the error on S' as

$$\begin{aligned}
\delta^2 S' &= \delta^2 N + (\delta^2 k)M^2 + k^2(\delta^2 M) && (4.24)\\
&= N + (\delta^2 k)M^2 + k^2 M && (4.25)\\
&= S' + B' + (\delta^2 k)M^2 + k^2 M && (4.26)\\
&= S' + B' + (\frac{\delta k}{k})^2(kM)^2 + k^2 M. && (4.27)
\end{aligned}$$

The last term is second order in k which has negligible contribution.

4.6.4 Systematic Errors

According to $v_2 = v_2^{raw}/\sigma_{RP}$, the main sources of the systematic error include uncertainties in σ_{RP} and v_2^{raw}. The former is estimated to be 10% for central and peripheral collisions and 5% for mid-central collisions by comparing measurements from different reaction plane detectors which reside in different pseudorapidity ranges as mention in section 4.1, as shown on Figure 4.8. The latter accounts for dependence of v_2 on π^0 identification cuts, as well as variation among different sectors of EMCal and different run groups, and are correlated in p_T; it is estimated to be 10% for central collisions and 3% for other centrality selections.

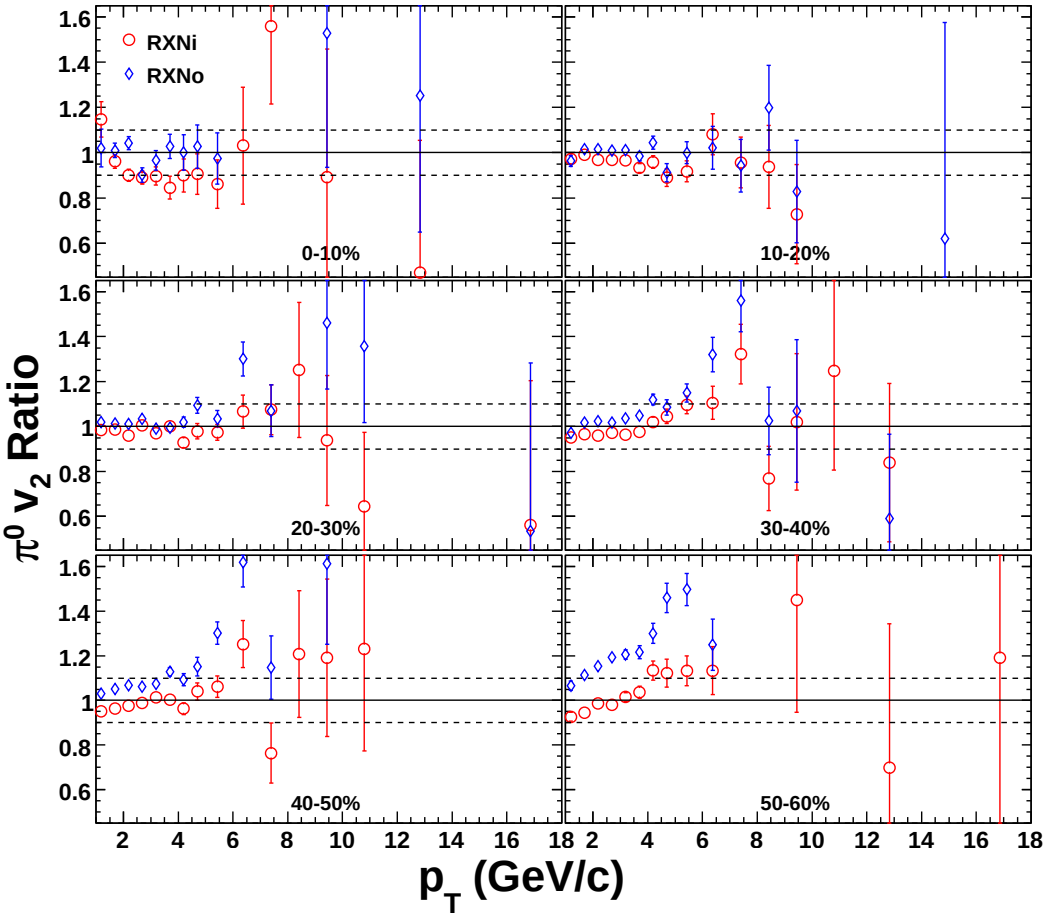

Figure 4.8: π^0 v_2 ratios of MPC results for RXNin and RXNout as function of p_T for centralies 0-10%, 10-20%, 20-30%, 30-40%, 40-50%, and 50-60%.

Chapter 5

Results

5.1 v_2 and v_4 results

The π^0 v_2 results are presented in Figure 5.1, with the reaction plane angle determined by the combined MPC/RXNin, using the $dN/d\phi$ method as described in section 4.5. The data are plotted as a function of mean π^0 p_T for six centrality bins, spanning the p_T range of 1-18 GeV/c, which nearly doubles the range of previouse PHENIX measurement [62] in Run-4 (Figure 5.3). The p_T binnings are $\Delta p_T = 0.5$ GeV/c for $p_T < 5$ GeV/c, $\Delta p_T = 1.0$ GeV/c for $5 < p_T < 10$ GeV/c, and $\Delta p_T = 2.0$ GeV/c for $10 < p_T < 18$ GeV/c. The error bars represent the uncorrelated statistical errors on the measured v_2 values arising from the statistical uncertainties on the $dN/d\Delta\phi$ data points. Figure 5.2 shows the results with combined centralities (0-20%, 20-40%, 40-60%, 20-60%), for better demonstration of the p_T trend of v_2 values, which is limited by the statistics at high p_T (>6 GeV/c). Figure 5.3 shows the consistency of the results by comparing to the previous measurement in

Run-4. With four times more statistics and much improved reaction plane resolution, the uncertainty on the v_2 measurement is greatly reduced.

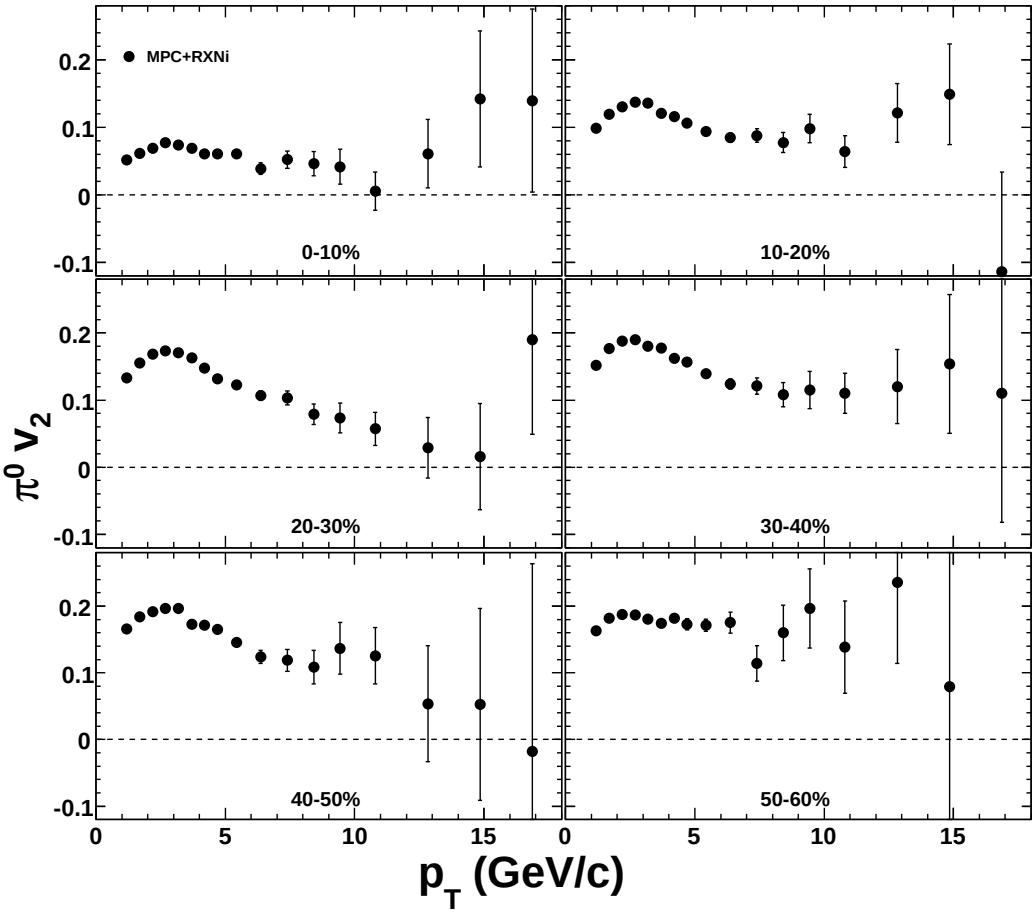

Figure 5.1: π^0 v_2 versus p_T for centralies 0-10%, 10-20%, 20-30%, 30-40%, 40-50%, and 50-60%.

The results in Figure 5.1 and 5.2 show a increase of v_2 at low p_T, reaching a maximum in the range of $p_T \sim 2.5$ GeV/c, then a slow decreasing trend is oberved between $3 - 7$ GeV/c across all centralities, and remains significantly above zero at higher p_T. The increasing trend at low p_T (< 3 GeV/c) is well understood by the hydrodynamic calculations [30, 75], resulting from the collective flow of the medium driven by the pressure gradient. At the high

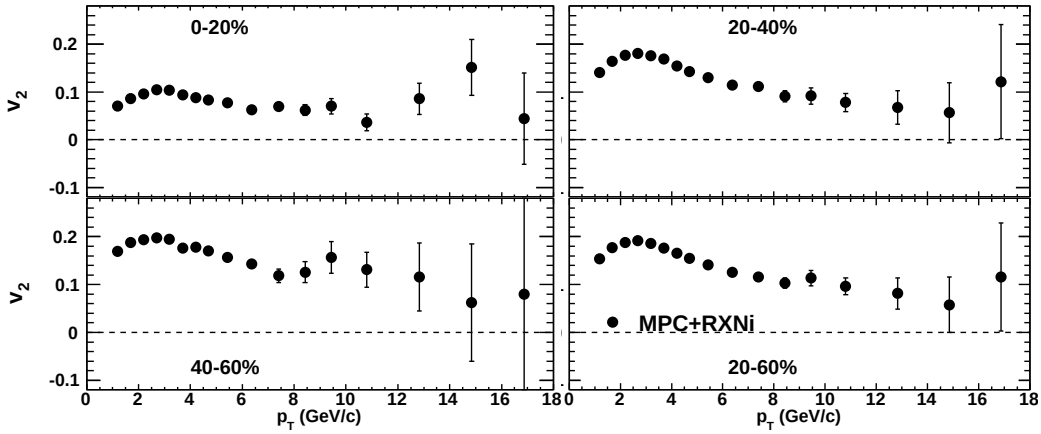

Figure 5.2: π^0 v_2 versus p_T for centralies 0-20%, 20-40%, 40-60%, and 20-60%.

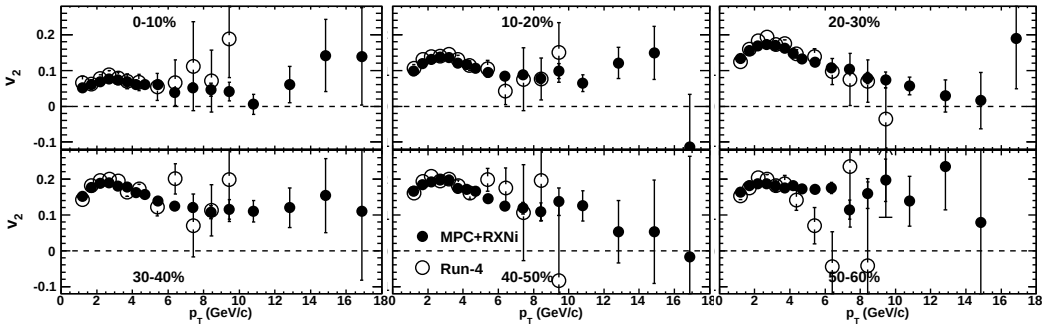

Figure 5.3: π^0 v_2 versus p_T compared with Run-4 results (open symbol).

p_T ($>$ 6 GeV/c), it is believed that the particle production is dominated by the fragmentations of jets which share lost energy penetrating through the medium. Dependening on the azimuthal emission angle, partons traversing such medium, on average experience different path lengths and therefore different amount of energy loss. This leads to an azimuthal anisotropy that is observed at high p_T. In the intermediate p_T range (3 ¡ p_T ¡ 6 GeV/c), the decreasing trend of v_2 may be the result of the detailed interplay of flow, jet quenching and recombination effects [80].

5.1.1 Low p_T: Hydrodynamics Region

It has been observed that the v_2 for identified particles at RHIC follows constituent quark number scaling [36], which suggests that the collective flow is developed at the partonic stage of the medium. Interesting questions arise that up to what KE_T ($= \sqrt{m^2 + p_\perp^2} - m$) the scaling still holds, and how about the higher order coefficients. Does v_4 follow the same scaling or different? Both are crucial to understand the picture of partonic collectivity.

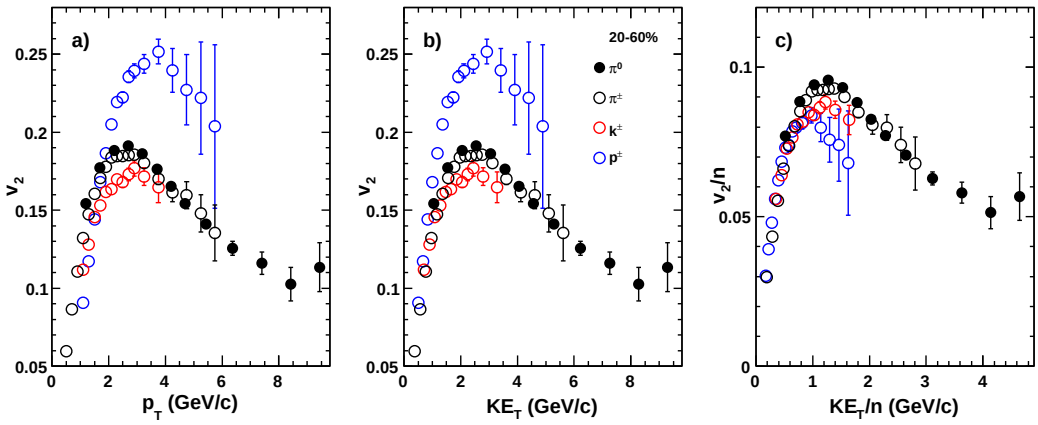

Figure 5.4: Comparison between π^0 and charged identified particles in 20-60% centrality plotted for a) v_2 vs. p_T; b) v_2 vs. KE_{T}; c) v_2/n vs. KE_{T}/n.

Much effort is ongoing to study the elliptic flow of different particle species. Figure 5.4 a) shows the v_2 as function of p_T for four identified particles, π^0, $\pi^{\pm}$, $k^{\pm}$ and $p\bar{p}$, in 20-60% centrality measured by PHENIX. The neutral pion and charged pion results are consistent in the common p_T range. In PHENIX, the identified $\pi^{\pm}$ results are limited to $p_T < 4$ GeV/c. [23], so the π^0 result can help to extend the comparisons with baryons ($p\bar{p}$) to higher p_T. At low p_T($<$ 2 GeV/c), a well know mass ordering of v_2 values is observed, that the heavier particles have smaller v_2. The proton v_2 crosses the pion v_2 at $p_T \sim 2$ GeV/c,

and reverses the mass ordering as that for low p_T. The v_2 is more strongly dependent on the quark composition of the particles than on their mass, which has been attributed to the dominance of quark coalescence mechanism for p_T $\sim$ 2-4 GeV/c. Figure 5.4 b) shows the same v_2 data as a function of KE_T. In contrast to the PID mass ordering observed in a), all particle species scale to a common set of elliptic flow values for $KE_T \leq 1$ GeV, this particle mass scaling gives way to a clear splitting into a meson branch and a baryon branch. c) shows the results obtained after constituent quark number scaling, that v_2 and KE_T are divided by the number of constituent quark n_q for meson ($n_q = 2$) and baryons ($n_q = 3$). An excellent scaling at $KE_T/n_q < 0.9$ GeV is consistent with the quark-like degrees of freedom picture in the flowing QGP medium.

At the $KE_T/n_q > 1.0$ GeV, the scaling seems to start breaking. In this KE_T range, the equivalent p_T for proton is about 5 GeV/c, where a different mechanism other than quark coalescence, jet quenching starts to kick in. It is not surprising that the scaling suggested by the quark coalescence model is violated at such high p_T. More detailed comparisons rely on the better baryon identification at high p_T in the future.

Figure 5.5 shows similar presentations of v_4 results as function of p_T and KE_T. Instead of divided by n_q in Figure 5.4 c), v_4 divided by n_q^2 follows the scaling between different particle species. This scaling is found by the motivation that in hydrodynamics, the v_4 goes like $\sim v_2^2$. This observation further strengthen the conclusion that partonic flow has been built up in the early stages of the QGP medium.

Figure 5.6 shows the v_4/v_2^2 ratio for pions, kaons and protons as function of p_T in the 20-60% centrality bin. This ratio is flat with p_T in the measured

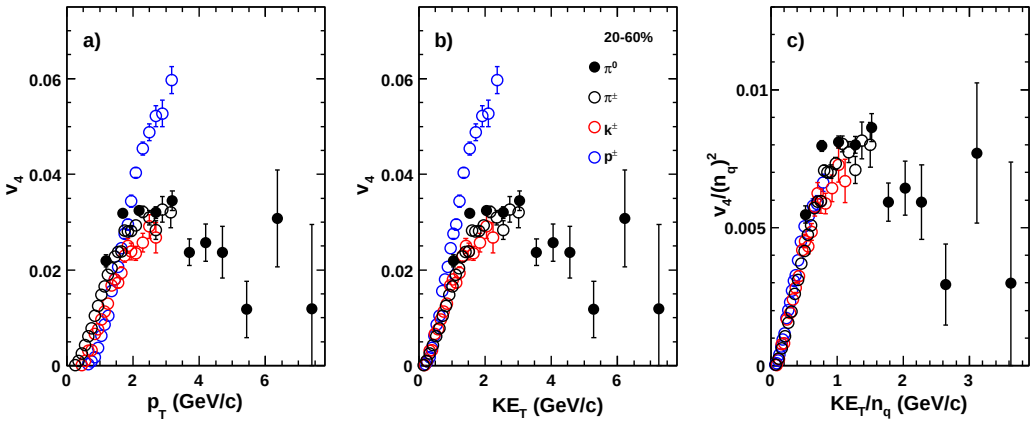

Figure 5.5: Comparison between π^0 and charged identified particles in 20-60% centrality. a) v_4 vs. p_T; b) v_4 vs. $K_{\rm ET}$; c) v_4/n^2 vs. $K_{\rm ET}/n$.

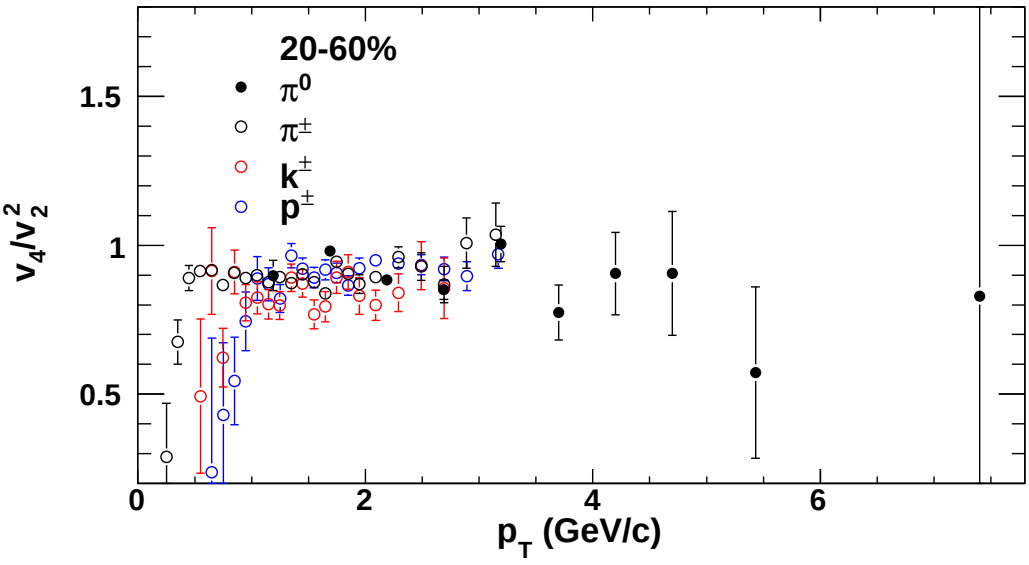

Figure 5.6: Comparison of v_4/v_2^2 between π^0 and charged identified particles in 20-60% centrality.

range and is independent of the particle species within errors. We analyze the results in terms of a simple coalescence model [81]:

$$\frac{v_{4,m}(2p_T)}{v_{2,m}^2(2p_T)} = \alpha(\frac{1}{4} + \frac{1}{2}\frac{v_{4,q}(p_T)}{v_{2,q}^2(p_T)}) \tag{5.1}$$

$$\frac{v_{4,b}(3p_T)}{v_{2,b}^2(3p_T)} = \alpha(\frac{1}{3} + \frac{1}{3}\frac{v_{4,q}(p_T)}{v_{2,q}^2(p_T)}), \tag{5.2}$$

where $v_{4,m}(p_T)$, $v_{4,b}(p_T)$ and $v_{4,q}(p_T)$ represent the meson, baryon and quark v_4 respectively, and $v_{2,m}(p_T)$, $v_{2,b}(p_T)$ and $v_{2,q}(p_T)$ represent the v_2. Using the measured v_4/v_2^2 ratio around 0.8 for both baryons and mesons, from Eq. 5.1 5.2, we obtain that the partonic $v_{4,q}/v_{4,q}^2$ ratio is around 0.5. This result indicates that a thermalized partonic liquid has been produced at RHIC.

5.1.2 Intermediate p_T: Recombination Region

In the intermediate p_T range (2-4 GeV/c), where the quark recombination process dominates, interesting phenomena such as the baryon/meson ratio anomaly [82], the doule peak structure of the away side in two particle correlations [62] are discovered. The interplay of flow (from low p_T) and jet (from high p_T) makes it challenging to interpret the data. The high precision v_2 data can shed some light in understanding the underlying physics.

Above 1.5 GeV/c, the observed v_2 starts to deviate from ideal hydrodynamics. The position of the onset of the deviation from ideal hydro and its magnitude are believed to constrain the shear viscosity of the fluid [83]. Figure 5.7 shows the pion v_2 results in more detailed centrality selections. We focus in the 2-4 GeV/c region where the v_2 reaches maximum. There is a suggestion that such turning of $v_2(p_T)$ is due to the viscous effect of the flowing medium [83]. With combined pion results (including π^0 and $\pi^{\pm}$), we fit the data points with second order polynomial function in the p_T region of 1.5-4 GeV/c, in order to find the peak position. The peak location as a function of N_{part} is presented in Figure 5.8. There is little centrality dependence of the

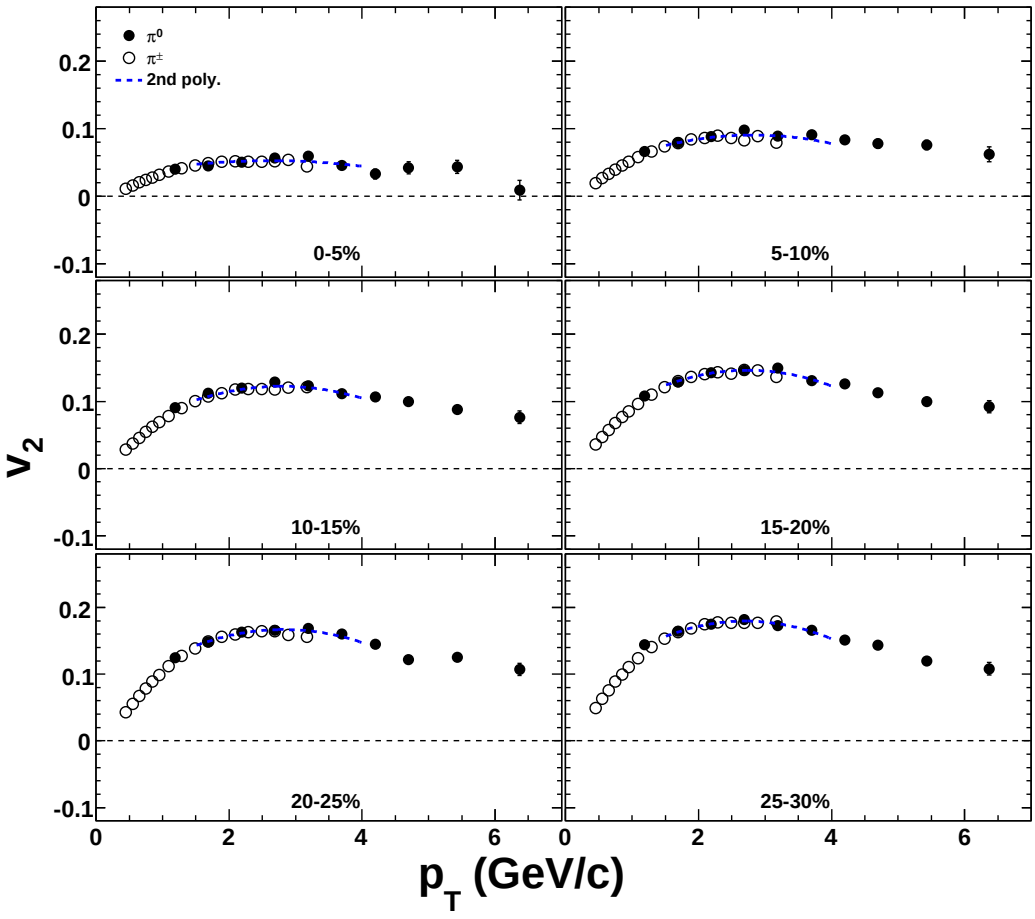

Figure 5.7: v_2 of π^0 and $\pi^{\pm}$ as function of p_T for different centralities. The second order polynomial functions are fitted to find the position of the v_2 maximum with these two combined data.

peak location, which may indicate that the phase transition has been reached in most centralities, and once above the critical temperature the QGP may have a similar η/s ratio which characterizes the transport property of the medium.

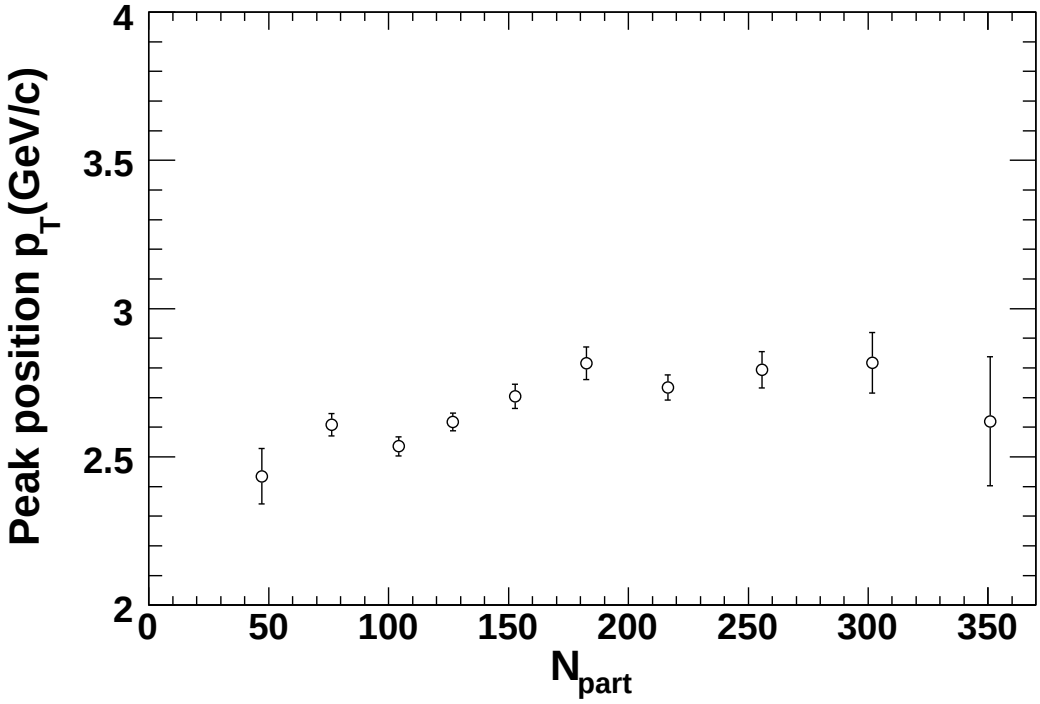

Figure 5.8: The peak position of v_2 maximum as function of $N_{\rm part}$

5.1.3 High p_T: Jet Quenching

From low p_T to high p_T, the particle production mechanism switches from quark recombination to jet fragmentation. An interesting question is that when the latter process becomes dominant, and whether it can be implied from the data.

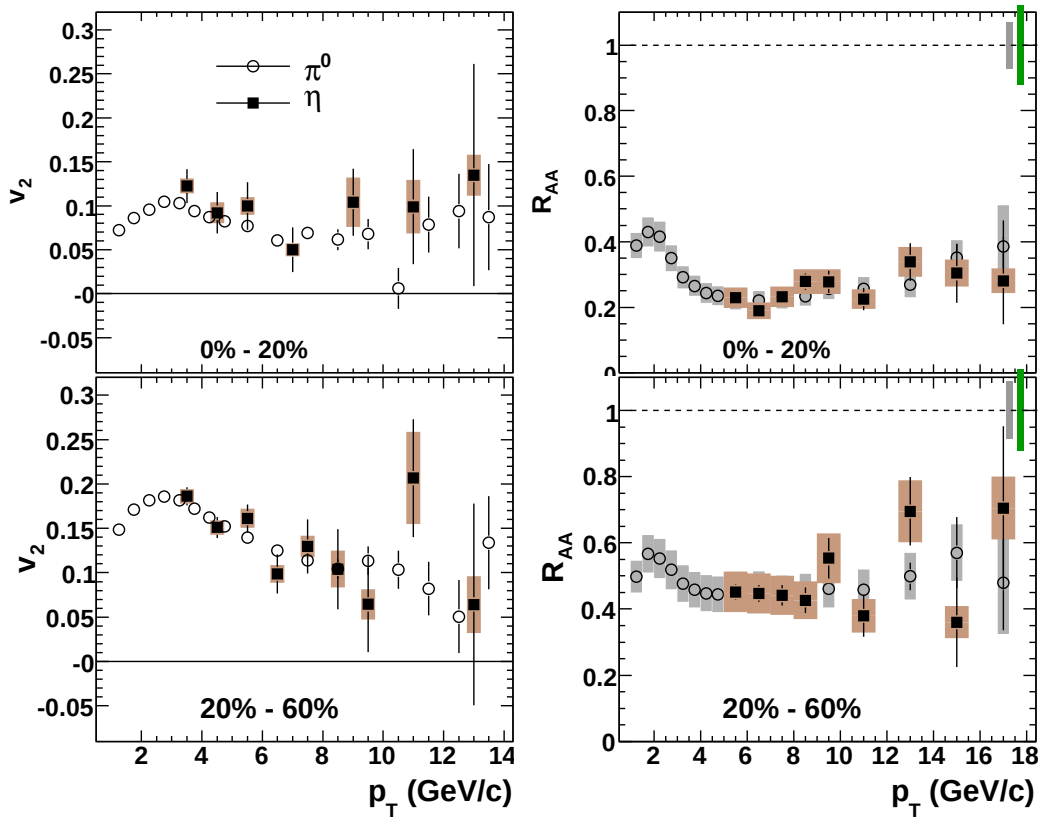

Figure 5.9: Left: η $v_2(p_T)$ and R_{AA} [84] compared to π^0.

The left panels of Figure 5.9 compare the v_2 for π^0 and η mesons. The systematic uncertainties on η v_2 are estimated by varying the η identification cuts, the parameterization of the residual background, and the peak integration window. The changes in v_2 values are added in quadrature to give the

total systematic uncertainty. At low p_T where the signal to background ratio is small, the total error is dominated by the η identification cuts, especially the asymmetry cut, and the residual background; it is correlated with p_T and is estimated to be about 15% in central bins and 10% in mid-central bins. At high p_T where the statistics are poor, the total error is dominated by the peak integration, and is correlated with the statistical error of the v_2. The uncertainties associated with the reaction plane resolution are common with the π^0 analysis, thus are not plotted.

Within errors, the π^0 and η v_2 are consistent with each other across the measured p_T range, suggesting the differences between their mass ($m_\eta = 0.55$ GeV, $m_{\pi^0} = 0.145$ GeV) and quark content ($(u\bar{u}-d\bar{d})/\sqrt{2}$ for π^0 and $(u\bar{u}+d\bar{d}-2s\bar{s})/\sqrt{6}$) do not lead to appreciable difference in their azimuthal anisotropyes at $p_T > 3$ GeV/c. This, together with their similar suppression levels (, indicated by the right panels of), seems to imply similar interactions with the medium, both at partonic phase for their constituent quarks and at the hadronic phase.

One possible scenario is that both are dominated by fragmentation of jets surviving the medium, at least at high p_T region where the jet quenching physics is expected to dominates. On the other hand, the v_2s of η and π^0 indicate slow but gradual decrease up to 7-8 GeV/c, whereas the suppression are flat for both species at $p_T > 4$ GeV/c. This suggest that the collective flow may still be important up to 7-8 GeV/c, even though the inclusive R_{AA} is not very sensitive. This attests to the importance of the reaction plane dependent suppression $R_{AA}(\Delta\phi)$ in studying the interplay between the collective flow and jet quenching, which is discussed in section.

Figure 5.10 shows the v_2s of inclusive charged hadrons and π^0. They increase monotonically at low p_T, cross each other at ~2 GeV/c, and then slowly decrease to a same relative flat value at $p_T > 5$ GeV/c. The merge of v_2 between π^0 and charged hadron may imply that the hadron production at high p_T is dominated by the jet fragmentation. The picture is supported by the jet quenching $R_{AA}(p_T)$ results. Figure 5.11 shows the nuclear modification factor $R_{AA}(p_T)$ for charged hadrons and π^0's [86]. At low p_T, the R_{AA} increases monotonically up to ~2 GeV/c for all centralities. In central collisions, at $p_T > 2$ GeV/c, it decreases at higher p_T down to an approximately constant value of 0.2-0.3 for $p_T > 5$ GeV/c. The π^0 R_{AA} shows the same trend, but the changes are smaller than those for charged hadrons. The fact that the π^0 R_{AA} values are smaller than the inclusive charged hadron R_{AA} at the intermediate p_T ($2 < p_T < 5$ GeV/c) can be explained by the large p/π ratios observed in the same p_T range in central Au+Au collisions [82]. In the high p_T region ($p_T > 5$ GeV/c), the parent parton loses energy travelling through the medium and fragments outside, thus gives rise to the similar suppression level and anisotropy of all hadron species.

5.1.4 Jet Bias: Non-flow Effect

In this measurement, the reaction plane angle in each event is determined by the detectors located at the forward region ($|\eta| > 1.0$), away from the central arms($|\eta| < 0.35$) where the π^0 v_2 is measured. The assumption behind this method is that all the particles are not correlated with each other, but only correlated with the reaction plane through the collective flow. However,

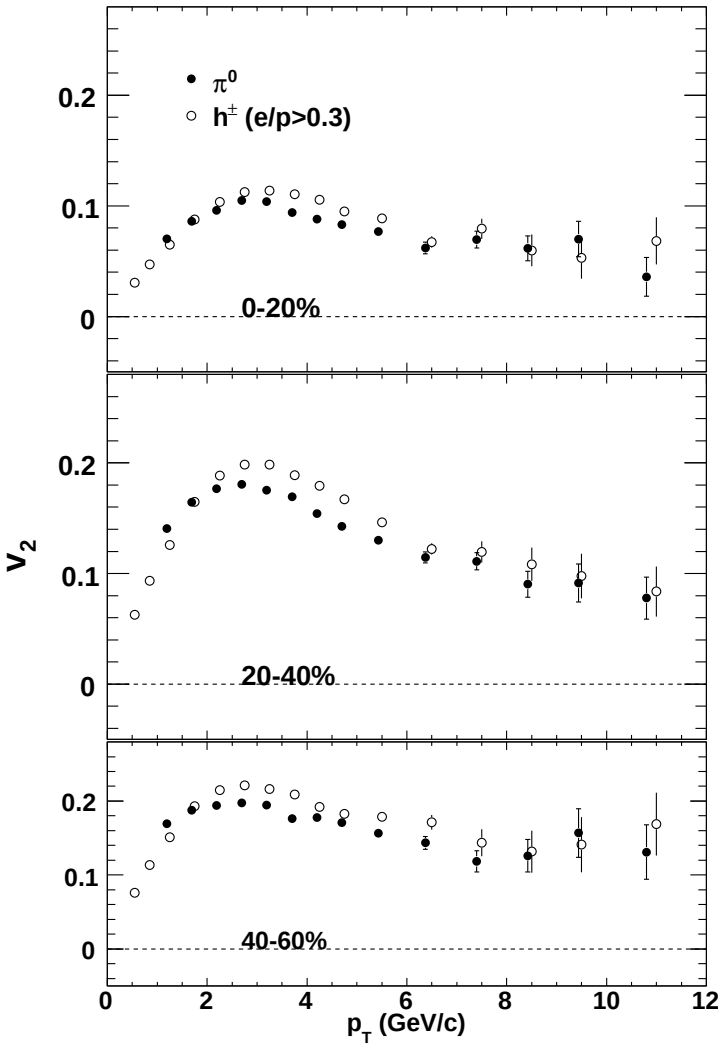

Figure 5.10: π^0 $v_2(p_T)$ compared to inclusive charged hadron $v_2(p_T)$ in three centrality selections.

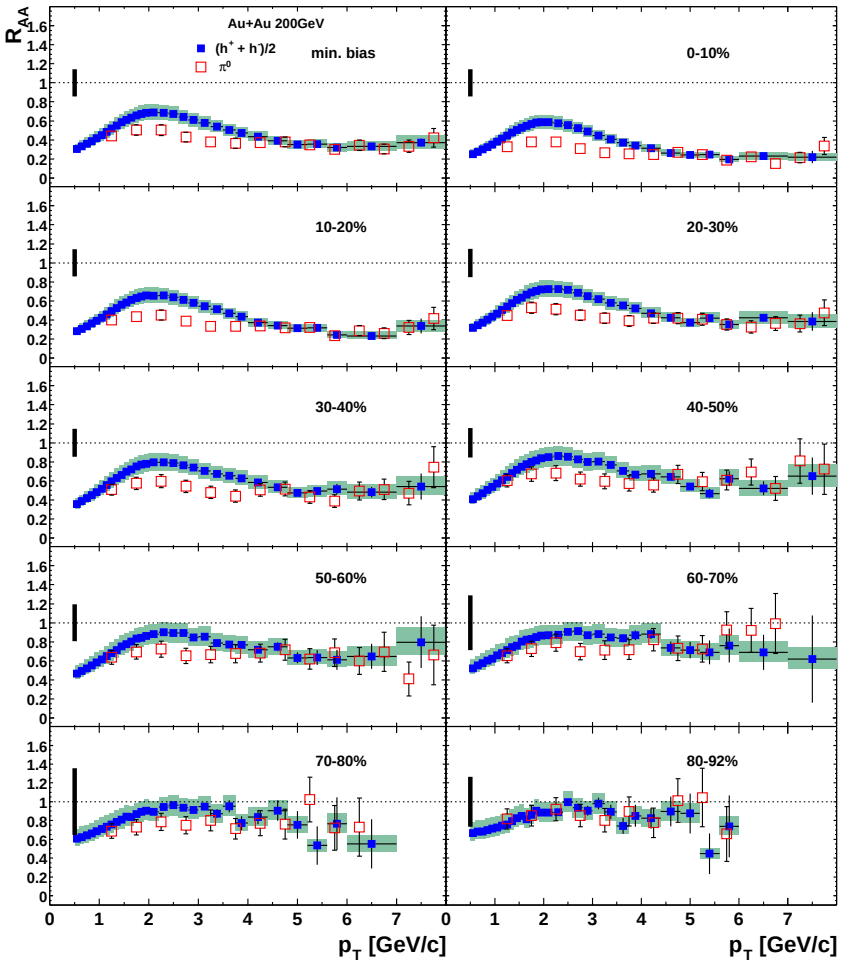

Figure 5.11: π^0 $R_{AA}(p_T)$ compared to inclusive charged hadron $R_{AA}(p_T)$ in several centrality selections [86].

there could be other correlations including transverse momentum conservation effects, resonance decays, HBT correlations and jet correlations. All these effects are called non-flow correlation, and they may affect the v_2 values either by changing the event plane resolution or introduce fake v_2 by biasing the event plane direction towards the non-flow particles. For example, if the particles produced by the fragmentation of near-side jet hit central arm and away-side hitting the forward detectors, the autocorrelations will be introduced, the reaction plane angle will biased towards to the jet direction and it can artificially increase the v_2 value.

There is belief that the long range jet correlation [85] can cause such non-flow effects. In the previous measurement, only BBC was used to measure the reaction plan angle, and it has been studied that the pseudorapidity range of BBC ($3.0 < |\eta| < 3.9$) can effectively suppress the non-flow effects. In Run-7, with several newly installed detectors:

- MPC ($3.0 < |\eta| < 3.9$);
- RXNin ($1.5 < |\eta| < 2.8$);
- RXNout ($1.0 < |\eta| < 1.5$);

we can study the bias on v_2 values due to the non-flow effect, by comparing v_2s using RP measured in different η windows of the forward detectors.

Figure 5.12 shows the measured v_2 values using three RP detectors, and Figure 5.13 shows the ratio of $v_2^{\mathrm{RXNin}}/v_2^{\mathrm{MPC}}$ and $v_2^{\mathrm{RXNout}}/v_2^{\mathrm{MPC}}$. At low p_T, the results are very consistent, within 10% and 5% for central and other centralities, respectively. At high p_T, the RXNout results are systematically higher

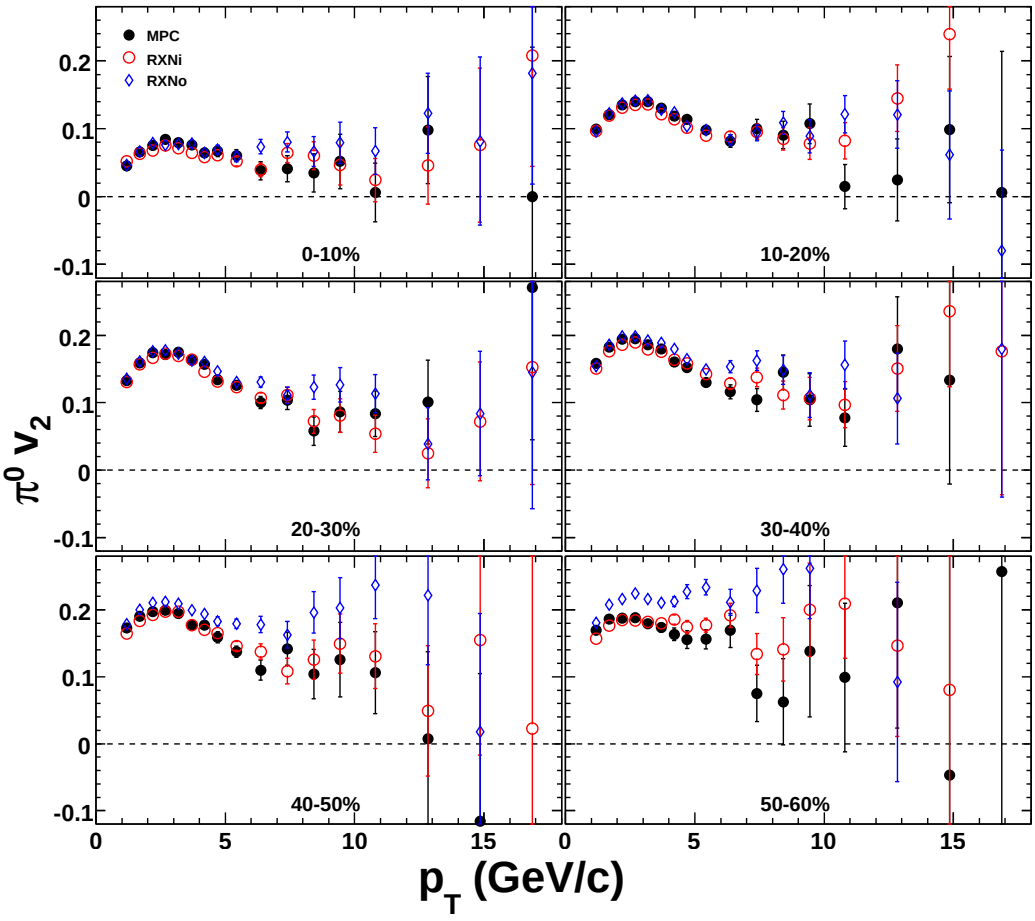

Figure 5.12: π^0 v_2 versus p_T using three different reaction plane detectors (MPC, RXNi and RXNout) for centralies 0-10%, 10-20%, 20-30%, 30-40%, 40-50%, and 50-60%.

than other two detectors, which could be due to the jet bias since it is sitting closer to central arm than other two. In events with hard process, the reaction plane determination can be biased towards to the jet direction. In the peripheral collisions, the RXNout results is always higher, independent of p_T, because the multiplicity in these events are much lower than central events, and the angle determination could easily be influenced by the jets. One can see more clear in Figure 5.14, at low p_T (1-1.5 and 3.0-3.5 GeV/c), all three detectors

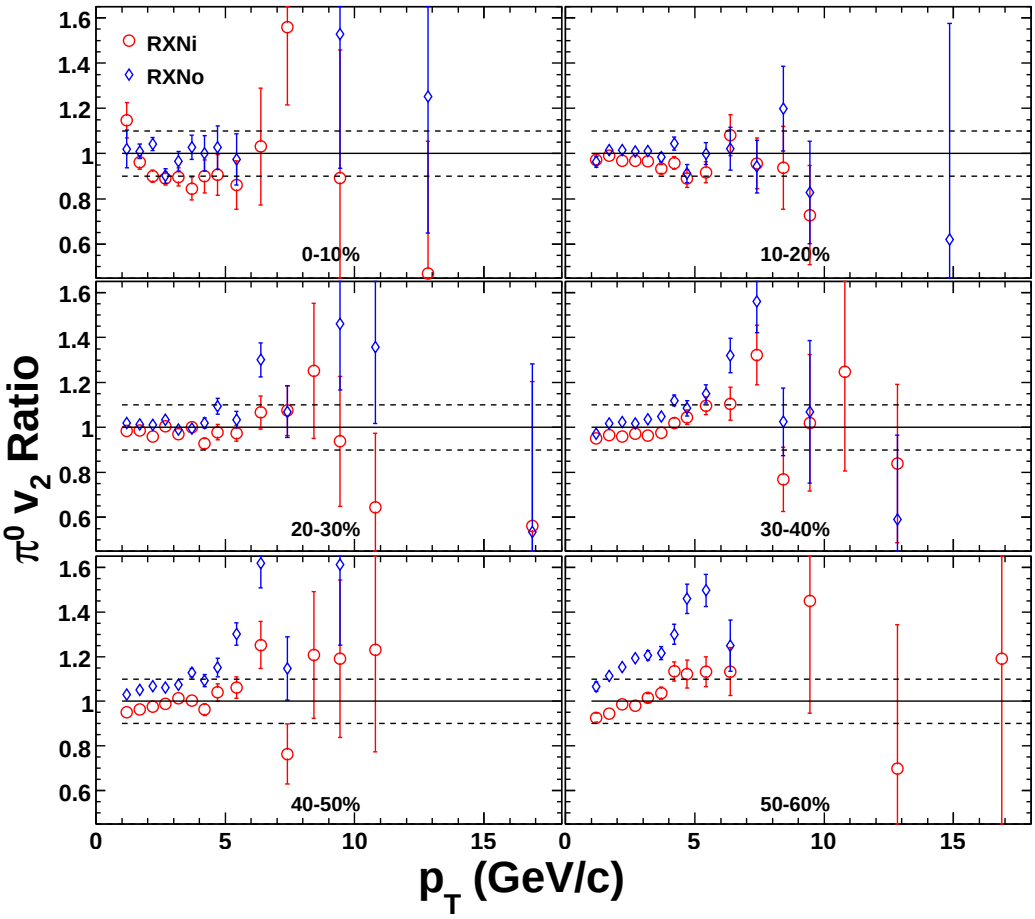

Figure 5.13: π^0 v_2 ratios to MPC results for RXNi and RXNout as function of p_T for centralies 0-10%, 10-20%, 20-30%, 30-40%, 40-50%, and 50-60%.

provide identical results except in the peripheral (50-60%) while at high p_T (6-9 and >9 GeV/c), RXNout clearly shows the jet bias in the measured v_2 results.

In order to improve the reaction plane resolution, while avoid such jet bias in our analysis, we decided to combine MPC and RXNin as described in section 3.2, with the results shown in Figure 5.1.

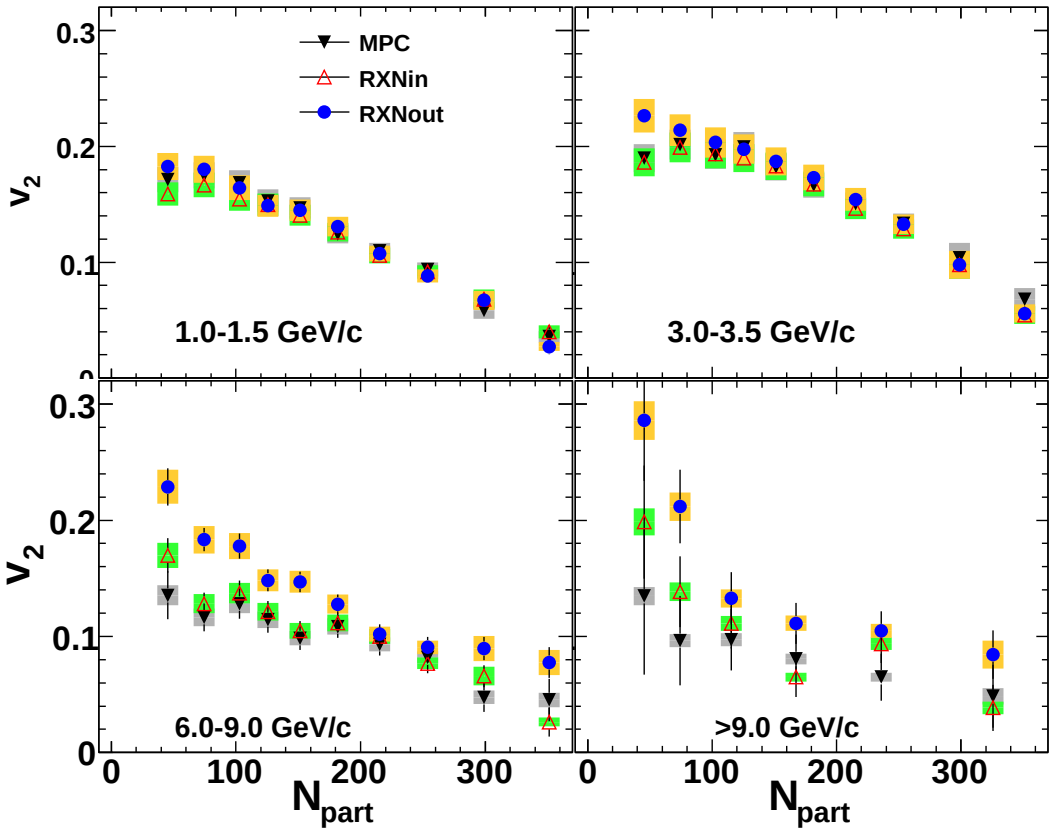

Figure 5.14: π^0 v_2 vs N_{part} for three detectors in different p_T selections.

5.1.5 v_2 Scaled by the Initial Eccentricity

As shown in Figure 5.14, at a given p_T, v_2 increases as the centrality becomes more peripheral. It is consistent with the change of initial collision geometry, that the eccentricity increases towards more peripheral events. However, to date, no direct experimental measurements of the initial collision geometry have been reported. Thus, theoretical models have to be assummed to properly estimate the initial geometric eccentricity. Glauber model as described in section 3.1 is a semi-classical model treating the nucleus-nucleus collisions as a superposition of the nucleon-nucleon collisions. Recent theoretical studies show that the initial collision geometry could be significantly modified by the gluon saturation effects [88]. This so called Color Glass Condensate geometry or CGC geometry has been implemented by Drescher et. al. into numerical code (MC-KLN model) [89].

In this study, we calculated the participant eccentricity defined as

$$\epsilon_{part} = \frac{\sqrt{(\sigma_y^2 - \sigma_x^2)^2 + 4\sigma_{xy}^2}}{\sigma_y^2 + \sigma_x^2} \tag{5.3}$$

in both models, MC-Glauber and MC-KLN. The models are constrained by the multiplicity measurements as a function of N_{part} for Au+Au collisions [39]. Especially in MC-Glauber calculations, an additional entropy density weight was applied reflecting the combination of spatial coordinates of participating nucleons and binary collisions:

$$\rho(\mathbf{r}_\perp) \propto (\frac{1-\alpha}{2}\frac{dN_{part}}{d^2\mathbf{r}_\perp} + \alpha\frac{dN_{coll}}{d^2\mathbf{r}_\perp}), \tag{5.4}$$

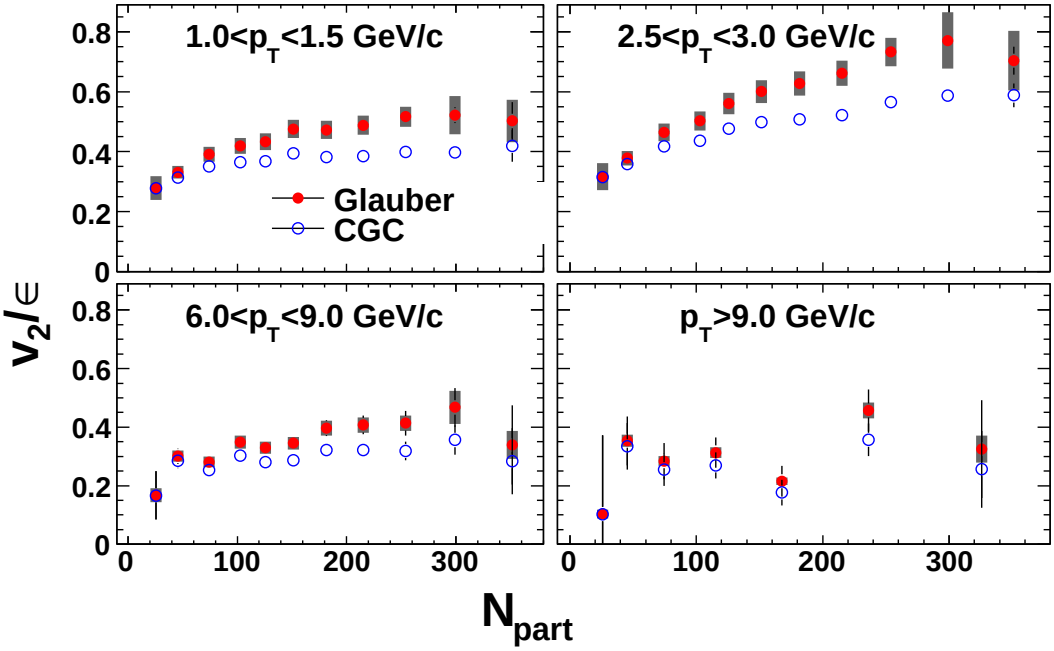

Figure 5.15: π^0 v_2 scaled by Glauber(solid) and CGC(open) eccentricities as a function of $N_{\rm part}$.

where $\alpha = 0.14$ to account for the centrality dependence of the multiplicity [39].

Figure 5.15 shows the v_2 scaled by the eccentricity separately in two models as a function of N_{part}. At low p_T (1-2 GeV/c), the CGC eccentricity scales v_2 better than the Glauber model, which may imply a small viscousity to entropy ratio (η/s) of the QGP medium [31]. The collective flow driven by the pressure gradient can effectively convert the initial spatial asymmetry to final momentum anisotropy. In the intermediate p_T region, the scaled v_2/ϵ decreases towards to the peripheral collisions, faster than that at low p_T. The interplays of viscous flow, coalescence and jets may cause such scaling violation. At high p_T, the trend is similar to the low p_T, but the dominant source is the path length difference of jet quenching, which can also effectively reflect the geometric asymmetry.

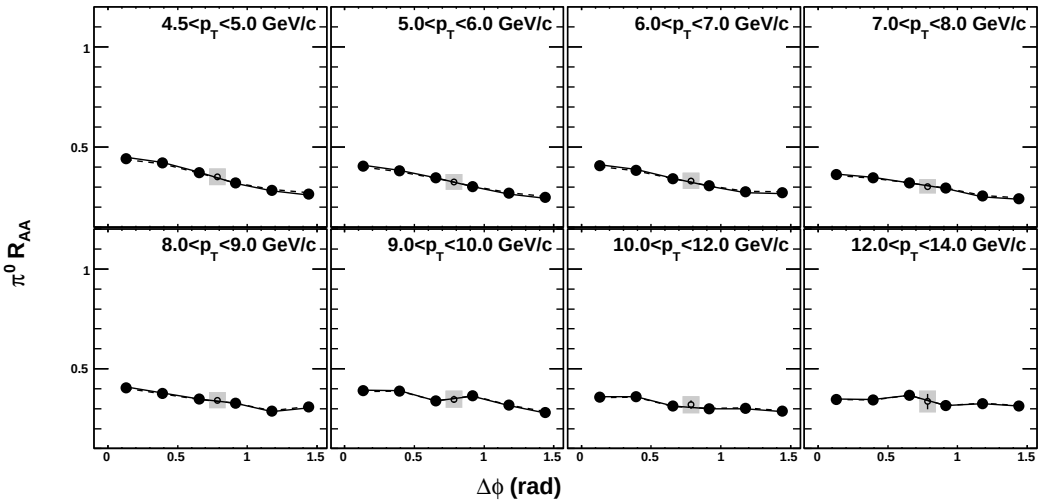

Figure 5.16: π^0 R_{AA} versus azimuthal angle with respect to the reaction plane for 20-30% centrality. The error bars denote the statistical errors, the solid and dash lines represent the systematic error due to the reaction plane resolution. The inclusive R_{AA} is shown with the open symbol.

5.2 $R_{AA}(\Delta\phi)$ Results

We also quantify the azimuthal anisotropy of the π^0 suppression by calculating the differential nuclear modification factor $R_{AA}(\Delta\phi_i)$ from the published inclusive R_{AA} as

$$R_{AA}(\Delta\phi_i) = R_{AA}\frac{N(\Delta\phi_i)}{\langle N(\Delta\phi)\rangle}\frac{1+2v_2\cos 2\Delta\phi_i}{1+2v_2^{raw}\cos 2\Delta\phi_i}, \tag{5.5}$$

where $N(\Delta\phi_i)$ denotes π^0 counts in the ith angle bin, and the last term accounts for the dilution from the imperfect reaction plane resolution.

Figure 5.16 presents the data versus the angles with respect to the reaction plane in 20-30% centrality at high p_T, with the inclusive R_{AA} measurement positioned at $\Delta\phi = \pi/4$. It is observed that the in-plane varies more rapidly with p_T than the out-of-plane.

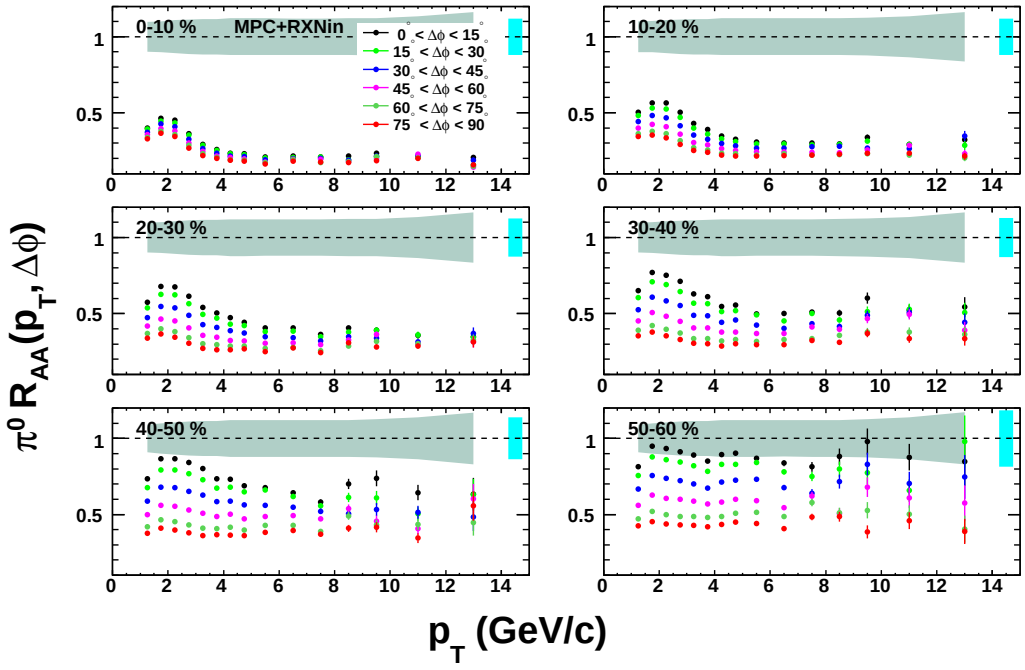

Figure 5.17: Nuclear modification factor R_{AA} as function of p_T for six different angular orientations with respect to the reaction plane.

Figure 5.17 shows the p_T dependence of the R_{AA} in each of the six $\Delta\phi$ bins. The in-plane direction has less suppression than the out-of-plane, compatible with path length energy loss picture. In each centrality, all six directions show a turn-over peaking in the p_T ~2 GeV/c region, start to decrease up to ~6 GeV/c and stay relative flat at higher p_T. This trend is very similar to the inclusive R_{AA} and v_2. The in-plane direction has stronger peaking than the out-of-plane, and it is more prominent in the central than the peripheral. Going from central to peripheral, the out-of-plane becomes more p_T independent, which may imply that jet quenching dominates in the out-of-plane direction, while mixes with collective flow in the in-plane direction [62].

When we focus on the two orientations interested, in-plane and out-of-plane, Figure 5.18 plots them as a function of centrality (N_{part}) for different

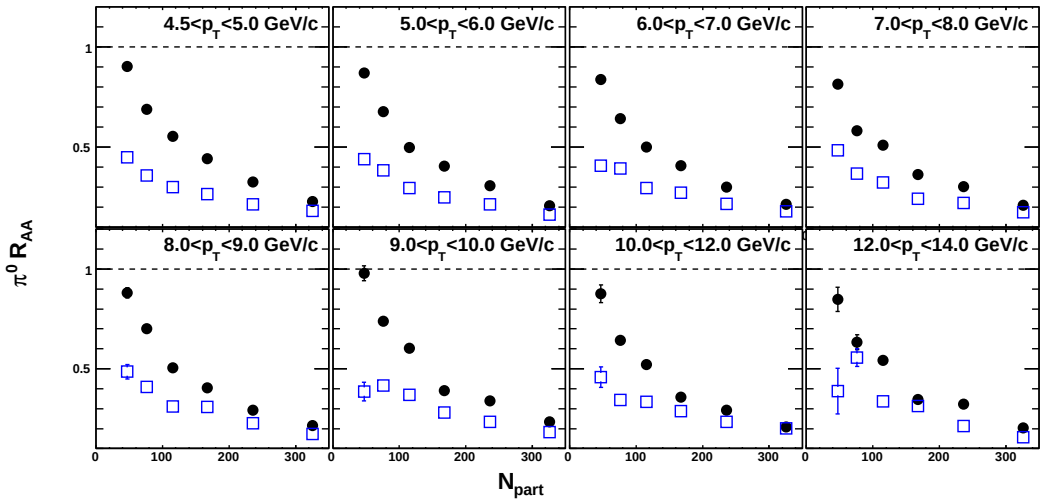

Figure 5.18: π^0 $R_{AA}(N_{part})$ for two angular bins in different p_T selections. The solid (black) symbol denotes the in-plane ($0 < \Delta\phi < 15°$), while the open (blue) is for the out-of-plane ($75 < \Delta\phi < 90°$).

p_T selections. It becomes clearer that in-plane direction has stronger centrality dependence. In central collisions, due to the symmetric shape of the overlap, the two directions has similar path length, thus has similar R_{AA} values. Going to more peripheral collisions, the path lenght of the jet within the overlap zone is changing more rapidly in the in-plane direction than the out-of-plane direction, which qualitatively explains why the in-plane has stronger centrality dependence.

5.3 Comparison with Jet Quenching Models

In this section, we focus on the comparisons between experimental results and theoretical calculations. In the high p_T region, most theoretical models of jet quenching are based on the perturbative QCD framework [57], which assumes that the coupling of jets with the medium is weak (due to the large energy scale) even though the medium itself is strongly coupled. By adjusting the input parameters, such as coupling strength, temperature, gluon density, these models can reproduce the observed suppression of single hadron spectra and di-hadron correlations. However, the medium properties implied by these input parameters, such as $\hat{q}$, differ significantly among these models [57].

Figure 5.19 shows the high p_T v_2 comparisons between our measurement (black) and WHDG model calculations. The Wicks-Horowitz-Djordjevic-Gyulassy (WHDG) model [92] utilizes the generalized GLV fomalism [93] for the radiative energy loss, and includes a convolution of radiative energy loss and collisional energy-loss mechanisms. A realistic transverse collision geometry with a Bjorken time expansion is utilized, and then a full distribution of parton paths through the medium is calculated. Three cureves with parameter (dN_g/dy = 1000,1400,1600 respectively) are plotted [94]. In the $p_T = 5 - 7$ GeV/c range where jet quenching is believed to dominate, the calculations are significantly below the experimental results, and have little p_T dependence. The model seems to describe higher p_T region ($>$ 8 GeV/c) in mid-central collisions 20-30% centrality.

Figure 5.20 (a)-(b) shows the centrality dependence of v_2 in two high p_T selections. They are compared with four pQCD jet quenching model calcu-

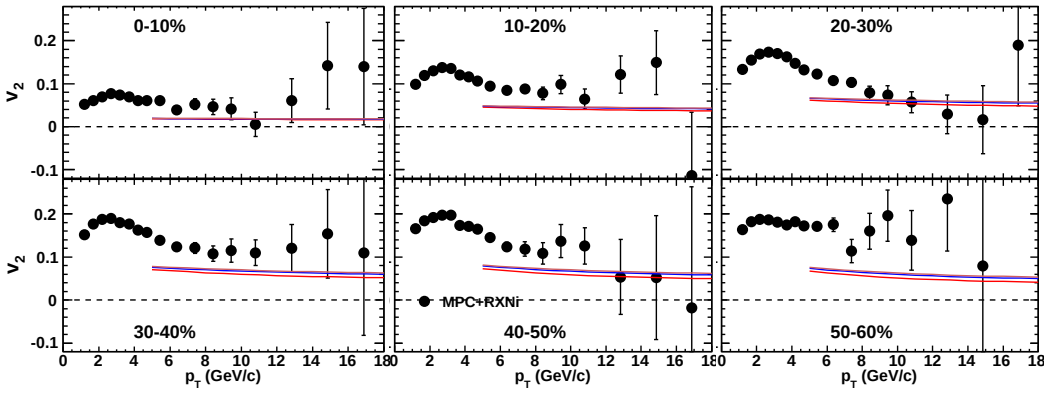

Figure 5.19: π^0 v_2 data compared to WHDG model, with parameter $dN_g/dy =$ 1000, 1400, 1600 separately.

lations, AMY, HT and ASW from [57] and WHDG from [92]. The WHDG model was calculated for gluon density $dN/dg = 1000 - 1600$, a range constrained by 0-5% ($N_{\rm part} = 351$) π^0 $R_{\rm AA}$ data [94]. The calculation assumes analytical Woods-Saxon nuclear geometry with a longitudinal Bjorken expansion. The AMY, HT and ASW models were fitted independently to the 0-5% π^0 $R_{\rm AA}$ data [57]; they were implemented in a 3D ideal hydrodynamic code with identical initial Wood-Saxon nuclear geometry, medium evolution and fragmentation functions. The HT and ASW models include only coherent radiative energy loss, while the AMY and WHDG also include collisional energy loss. The ASW and WHDG models predict quite sizable, and similar v_2, while the HT and AMY models tend to give much smaller v_2. However, all models significantly under-predict the v_2 data in $6 < p_T < 9$ GeV/c range. For $p_T > 9$ GeV/c, ASW and WHDG results show a better agreement with the 20-30% ($N_{\rm part} = 167$) centrality bin due to a slow decrease of v_2 with p_T in this bin (see Fig. 5.3). However, this seems to be accidental, since the v_2 values for the other centrality bins remain large, and are significantly above the WHDG

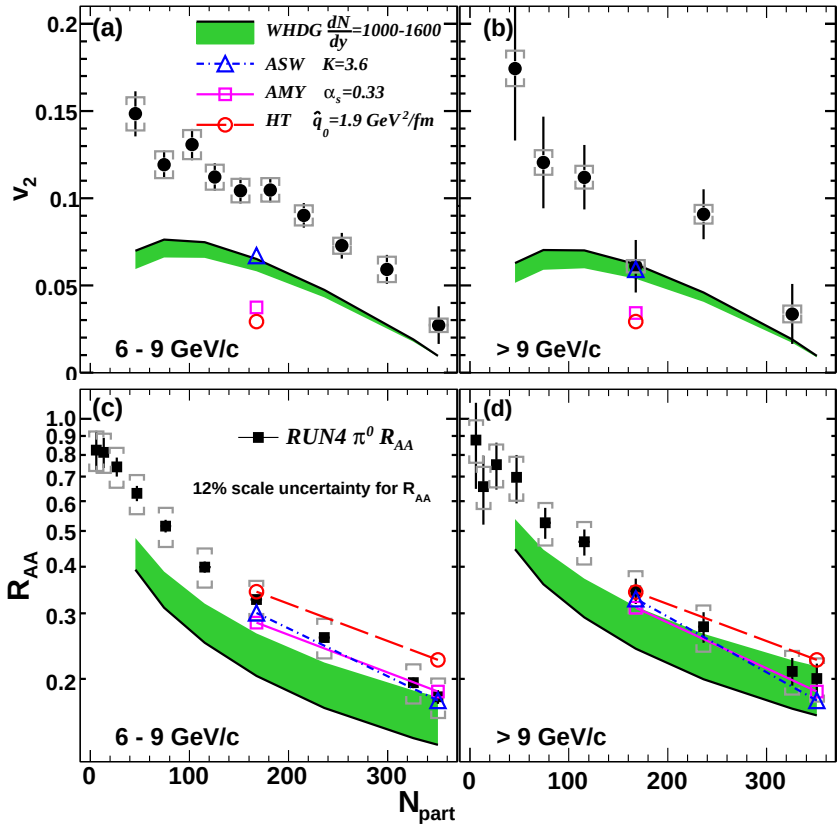

Figure 5.20: (Color online) (a)-(b) v_2 vs $N_{\rm part}$ in two p_T ranges; (c)-(d) $R_{\rm AA}$ vs $N_{\rm part}$ in same p_T ranges. Each are compared with four pQCD models from [57] (AMY, HT, ASW) and [92] (WHDG). Log-scale is used for $R_{\rm AA}$ to better visualize various model calculations. Note that the $\frac{dN}{dg}$=1000 of WHDG corresponds to lower (upper) boundary of the shaded bands for v_2 ($R_{\rm AA}$), while $\frac{dN}{dg}$=1600 corresponds to upper (lower) boundary for v_2 ($R_{\rm AA}$).

calculations (the p-value for the agreement is $< 10^{-4}$).

On Figure 5.21, the in-plane and out-of-plane R_{AA} in 20-30% centrality are calculated from a fit to inclusive R_{AA} to remove the statistical fluctuations. A clear split of the suppression levels can be seen between two directions, which persists to high p_T, consistent with large v_2 shown in previous section. The three pQCD jet quenching models predictions (AMY, HT, ASW) from [57], computed with identical initial conditions, medium evolution and fragmenta-

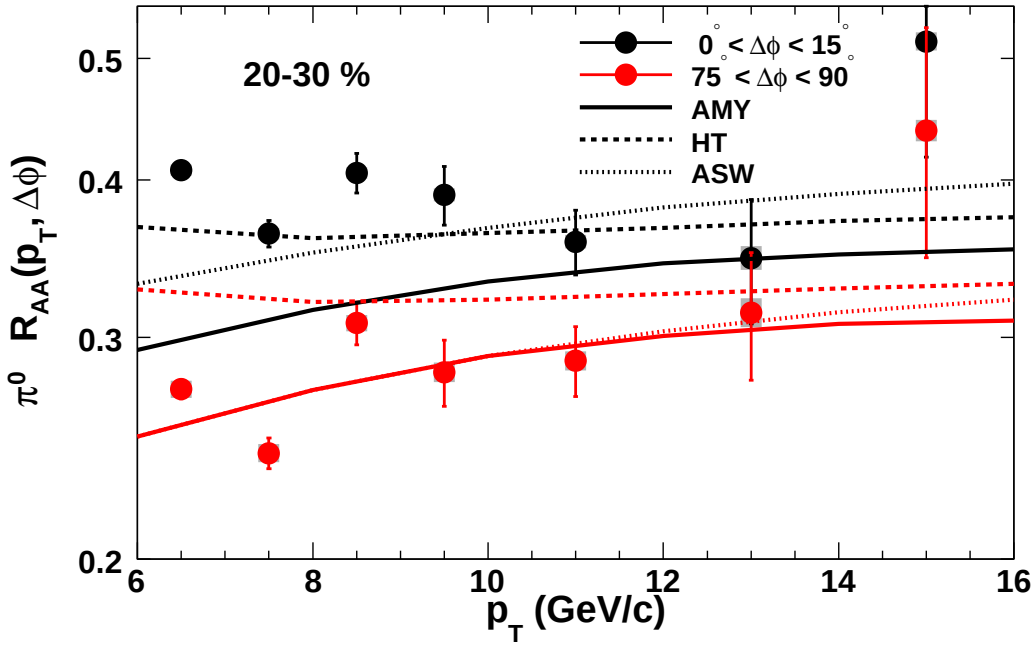

Figure 5.21: The 20-30% centrality $R_{AA}(\Delta\phi)$ compared with three pQCD models.

tion functions, are compared with data. AMY describes the out-of-plane, but misses in-plane. HT is the opposite. ASW model does a resonable job for both in- and out-of plane directions at high p_T, but misses the low p_T region. However, changing other parameters in the models, such as initial conditions, medium evolution or fragmentation functions may change this comparison. It is worthwhile to point out that the models are accidental to relatively well describe the data in 20-30% centrality. It will be interesting to see whether pQCD models can describe the anisotropy for other centrality selections.

In all these models, the inclusive suppression $R_{\rm AA}$ and v_2 are anti-correlated, *i.e.* a smaller $R_{\rm AA}$ implies a larger v_2 and vice versa. Consequently, more information can be obtained by comparing the data with a given model for both $R_{\rm AA}$ and v_2. Fig. 5.20 (c)-(d) compares the centrality dependence of π^0 $R_{\rm AA}$

data to four model calculations for the same two p_T ranges [97]. The calculations are available for a broad centrality range for WHDG, but only in 0-5% and 20-30% centrality bins for AMY, HT and ASW. The level of agreement varies among the models. The HT calculations are slightly above the data in the most central bin, while WHDG systematically under-predicts the data over the full centrality range, though better agrement with the data is obtained for $p_T > 9$ GeV/c. On the other hand, ASW and AMY calculations agree with the data very well in both p_T ranges. The different levels of agreement among the models are partially due to their different trends of $R_{\rm AA}$ with p_T: WHDG and ASW results have stronger p_T dependences than what is impled by the data, and tend to deviate at low p_T when fitted to the full p_T range [57, 94]. Given the larger fractional systematic error for $R_{\rm AA}$ measurements compared to the v_2 measurements, the deviation of $v_2(N_{\rm part})$ from the data is more dramatic than that for the $R_{\rm AA}(N_{\rm part})$. Nevertheless, Fig. 5.20 clearly shows the importance for any model to simultaneously describe the $R_{\rm AA}$ and the azimuthal anisotropy of the data.

The fact that the high p_T v_2 at RHIC exceeds expectation of pQCD jet-quenching models was first pointed out in Ref. [102] in 2002. This was not a serious issue back then since the p_T reach of early measurements was rather limited, and the v_2 could be strongly influenced, up to 6 GeV/c for pions, by collective flow and recombination effects rather than jet quenching [103]. Fig. 5.20 clearly shows that the v_2 at p_T above 6 or even 9 GeV/c still exceeds the pQCD-based energy loss models. It is possible that geometrical effects due to fluctuations and CGC effects, ignored in these models, can increase the calculated v_2; it is also possible that the energy loss process in the sQGP has

a steeper l dependence (*e.g.* AdS/CFT) than what is currently implemented in these models.

On the other hand, the failure of these models to reproduce the large anisotropy at high p_T may imply that the pQCD treatment of the energy loss process as sequential radiation, being proportional to the local color charge density is not sufficient. In the presence of the strongly coupled medium (sQGP), both the path length dependence and the color charge dependence could be modified. For example, calculation based on AdS/CFT technique suggests that $\Delta E \propto L^3$ [95] and $\hat{q} \propto \sqrt{\alpha_{SYM} N_c}$ [96] instead of $\Delta E \propto L^2$ and $\hat{q} \propto \alpha_S N_c^2$ for pQCD. In a separate calculation, Kharzeev [98] estimates $dE/dx \propto E^2$ in strong coupling limit, much stronger than the logarithmic dependence expected from pQCD. These non-linear dependences could be the reason for large anisotropy. Figure 5.22 shows the comparisons of v_2 with two toy model predictions with different medium density dependence. The model from [99] introduces strong non-linear dependence by assuming that jet quenching happens mostly close to phase transition boundary. The model from [100] does so by suppressing the energy loss at high energy density region by using a plasma formation time argument. Both are able to qualitatively describe centrality dependence. However, much need to be done to generalize these toy models into rigorous theoretical calculations.

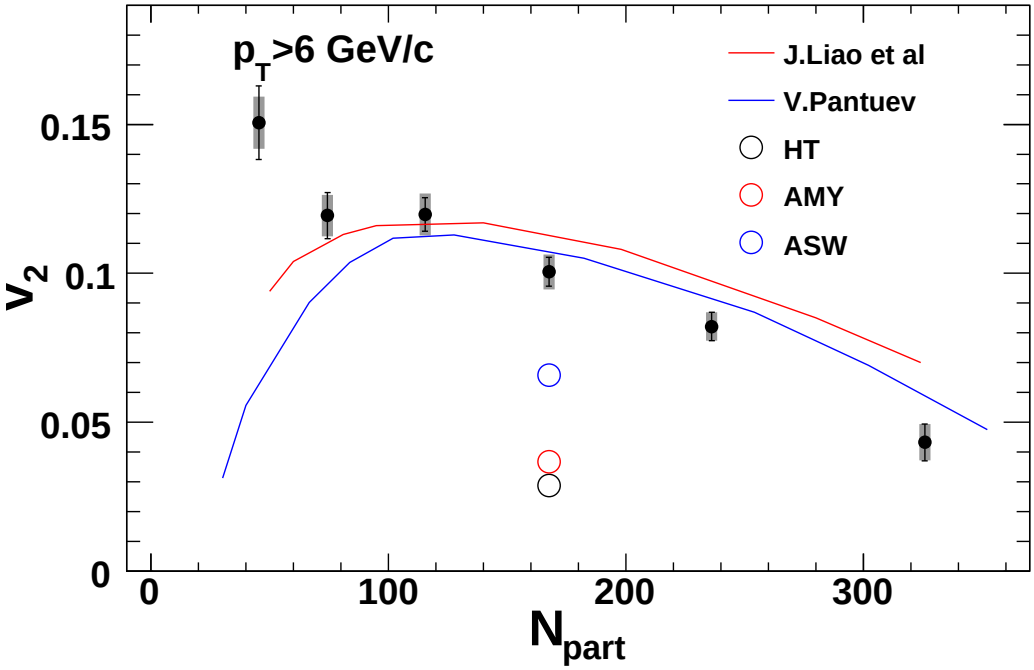

Figure 5.22: Data points: v_2 values at $p_T > 6$ GeV/c. Open symbols: pQCD model calculations [57]. Lines: geometric model calculations with different assumptions on path length dependence [99, 100].

5.4 Importance of Geometry and Path Length Dependence

The failure of pQCD models in describing the high p_T azimuthal anisotropy may indicate that the data favor a l dependence stronger than the naive $\Delta E \propto l^2$ implied by the radiative energy loss. However, as was pointed out in [101], the magnitude of the anisotropy is also very sensitive to the choice of initial collision geometry, which is poorly constrained. The collision geometry used by most jet quenching calculations is obtained from the so-called Optical Glauber model [71], which assumes a smooth Woods-Saxon nuclear geometry for Au ions. It ignores two important modifications: an event-by-event distortion of the shape of the overlap from random fluctuation of positions of participating nucleons [87]; and a possible overall distortion of the shape of the overlap due to, *e.g.* gluon saturation effect (so called CGC geometry [88]). Both effects are shown to lead to 15-30% corrections in the hydrodynamic calculation of elliptic flow at low p_T [39]; they were also shown in Ref. [88, 90] to play an important role for jet quenching calculation of azimuthal anisotropy at high p_T.

In this section, we investigate the sensitivity of the jet quenching v_2 on the choices/uncertainties of the collision geometry for the bulk matter. We explore, in the context of these uncertainties, whether the data allow for high order l dependence of energy loss.

5.4.1 Jet Absorption Model

The collision geometry is modelled by a Monte Carlo Glauber simulation of Au + Au collisions [74]. For the Au nucleus a Woods-Saxon density distribution with radius $R = 6.38$ fm and diffussness $a = 0.53$ fm is used. We calculate for each simulated Au + Au collision the underlying number of nucleon-nucleon collisions ($N_{\rm coll}$) and the number of participating nucleons ($N_{\rm part}$), assuming the inelastic nucleon-nucleon cross section is $\sigma_{NN}^{\rm inel} = 42$ mb.

For each centrality class, we calculate the participant density profile, $\rho_{\rm part}(x, y)$, and the nucleon-nucleon collision density profile, $\rho_{\rm coll}(x, y)$, in the plane transverse to the beam direction. We also include the eccentricity fluctuations event-by-event. In a given event, the impact parameter is defined along the x-axis. Due to the finite number of nucleons, the participant plane does not necessary lie along the x-axis, but is tilted by the angle Ψ (Figure 5.23):

$$\tan 2\Psi = \frac{\sigma_y^2 - \sigma_x^2}{2\sigma_{xy}} \tag{5.6}$$

where σ_x^2, σ_y^2 are the variances of the participating nucleons profile. The participant and collision profiles are generated by sampling many events. In stead of simply overlaping the events as in nucl-th/0310044, we generate another set of profiles by rotating the participant plane of every event back to x-axis, and then average over the profile together. The profiles are shown in Figure5.24.

In the following we assume that the energy density is proportional to the participant density. This is motivated by the recognition that the bulk particle production scales approximately with the number of participants. To give the participant density a physical scale we relate it to the energy density using the

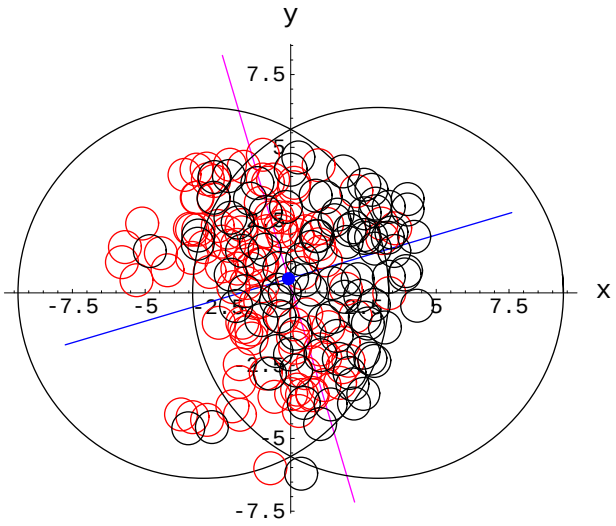

Figure 5.23: In one Au+Au collision, the participant plane is titled.

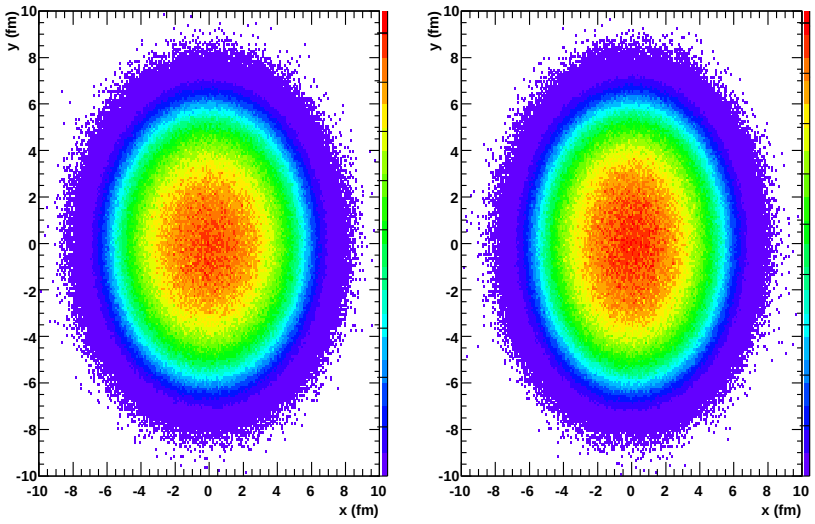

Figure 5.24: The participant profile at most central (0-5%) input for calculation. Left: no rotation; right: with rotation.

Bjorken estimate,

$$\epsilon_{\rm bj} = \frac{E}{\tau_0 A} \propto \frac{N_{\rm part}}{\tau_0 \pi r_0^2 \left(\frac{N_{\rm part}}{2}\right)^{2/3}} \tag{5.7}$$

where $\tau_0 = 0.2$ – 1 fm/c is the formation time, $r_0 = 1.2$ fm is the effective

nucleon radius, and $N_{\rm part}$ is the number of participating nucleons. For central collisions the experimentally determined value of $\epsilon_{\rm bj}$ is ≈ 5 GeV/fm^3 for $\tau_0 = 1$ fm/c. With approximately 350 participants the scale factor to convert participant density to $\epsilon_{\rm bj}$ is 2 GeV/fm for $\tau_0 = 1$ fm/c or 10 GeV/fm for $\tau_0 = 0.2$ fm/c.

We generate the CGC geometry using the MC-KLN model by Dresher & Nara [88, 89], which is based on the well known KLN (Kharzeev-Levin-Nardi) k_T factorization approach [91]. In a nutshell, the MC-KLN model calculates the CGC geometry event by event by modifying the output from a Monte-Carlo Glauber model. Specifically, the transverse gluon density profile, $dn/dy(x, y, b)$, is calculated through the k_T factorization formula, with the saturation scale Q_s^2 of each Au ion set to be proportional to its thickness function T_A or T_B. To insure internal consistency, the MC-KLN code is adapted to the same Glauber algorithms as the PHOBOS code (same hard-core nucleons and identical Woods-Saxon parameters). The obtained gluon density scales approximately [88] as $\min\{T_A, T_B\}$ in the x direction and $1/2(T_A + T_B)$ in the y direction, which leads to a 20-30% increase of the eccentricity relative to the Glauber geometry [104]. When implemented in hydrodynamic model calculations [39, 40], a similar amount of increase is seen for the predicted elliptic flow signal.

Binary scaling of hard scattering assumes that the incoming parton distribution in Au + Au collisions is a superposition of the individual nucleon parton distribution functions. According to the factorization theorem the probability for the hard scattering processes in Au + Au is then proportional to $\rho_{\rm coll}$. Therefore we generate back-to-back parton pairs in the transverse plane with

a distribution of $\rho_{\rm coll}(x,y)$ and isotropically in azimuth. These partons are then propagated through the nuclear medium with density proportional to $\rho_{\rm part}(x,y)$. The survival probability of a parton produced at (x,y) along direction (n_x,n_y) is calculated as

$$f = \exp(-\kappa I_m), \tag{5.8}$$

where κ is the absorption strength, which is the only free parameter in the model. I_m is the matter integral along the path of the parton, which is calculated as,

$$I_1 = \int_0^\infty dl\ \ l\frac{l_0}{l+l_0}\rho(x+(l+l_0)\,n_x, y+(l+l_0)\,n_y) \simeq \int_0^\infty dl\ \rho \tag{5.9}$$

This parameterization corresponds to a quadratic dependence of the absorption ($\propto ldl$) in a longitudinally expanding medium ($\frac{l_0}{l+l_0}$). Here we assume that partons travel with speed of the light and that they sense the dense matter after a formation time of 0.2 fm/c or a distance of $l_0 = 0.2$ fm.

We also examined three additional stronger L dependence: $I_2 = \int_0^\infty dl\ l\rho$, $I_3 = \int_0^\infty dl\ l^2\rho$, $I_4 = \int_0^\infty dl\ l^3\rho$. Similarly, I_2 is mapped in to the l^3 dependence of the absorption in a longtitudinally expanding medium, which is implied by the AdS/CFT theory [95]. The κ factor in each scheme is tuned to match the most central R_{AA} data as shown in Figure 5.25. All models can describe the centrality dependent R_{AA} quite well, which implys that the discriminating power of R_{AA} alone is not enough to distinguish between these models.

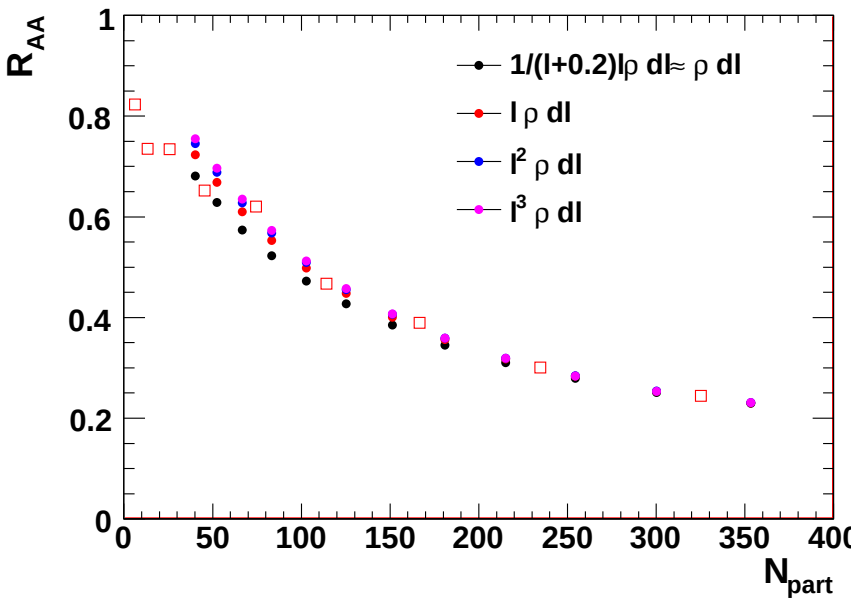

Figure 5.25: R_{AA} vs. $N_{\rm part}$. Open symbol: inclusive R_{AA} data.

5.4.2 Discussion

The v_2 calculated from the Glauber models are shown in Figure 5.26, compared with pQCD calculation (WHDG[92]). As expected, without the fluctuations and its quadratic dependence, WHDG is consistent with the I_1 without fluctuation case. Fig. 5.27 compare the v_2 calculated for CGC geometry (ρ_3) and Glauber geometry (ρ_0) in their respective rotated frames. The CGC geometry does lead to a larger v_2,

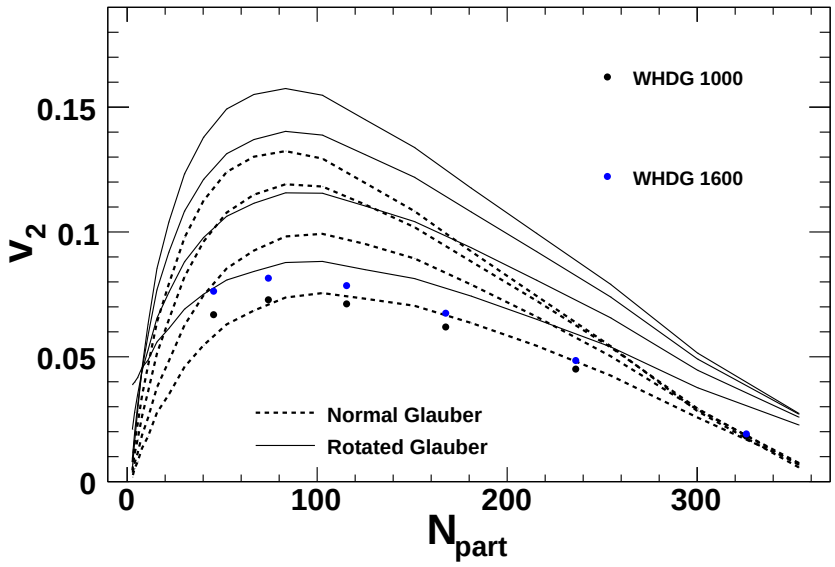

Figure 5.26: v_2 vs $N_{\rm part}$ from the jet absorption model calculation compared with WHDG calculations. Solid line: with fluctuations; Dashed line: without fluctuations. For each group of curve, from bottom to top are I_1, I_2, I_3, and I_4.

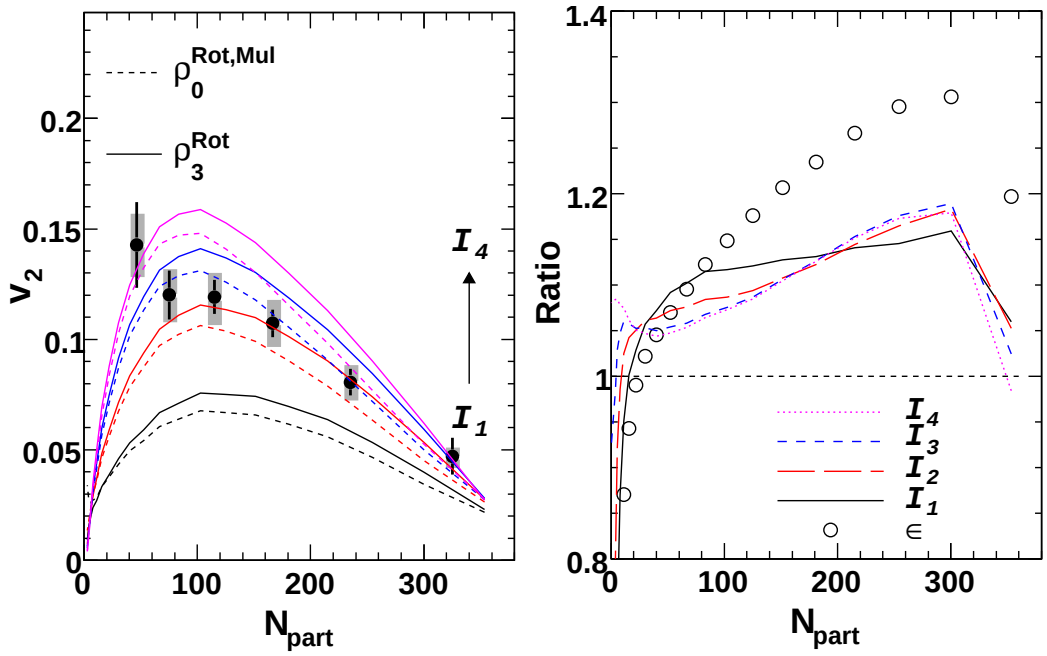

Figure 5.27: (Color online) Left: v_2 calculated for Glauber geometry (ρ_0^{Rot}) and CGC geometry (ρ_3^{Rot}) in their respective rotated frames for $I_1 - I_4$ (from bottom up). Right: Corresponding ratios for v_2s from $I_1 - I_4$ (lines) and for the eccentricity (open circles). Note that the CGC geometry has larger eccentricity.

To test whether initial eccentricity flutuation and stronger path-length dependent jet energy loss could bridge the difference between data and theory (Fig. 5.20), we compare the data with the jet absorption model (abbreviated as JR model as in Ref.[107]). The short-dashed curves in Fig. 5.28(a) show that the result for Glauber geometry without rotation ($\rho_{\rm GL}$) compares reasonably well with those from WHDG [92] and a version of ASW model from [105]. Consequently, we use the JR model to estimate the shape distortions due to fluctuations and CGC effects. The results for Glauber geometry with rotation ($\rho^{\rm Rot}_{\rm GL}$) and CGC geometry with rotation ($\rho^{\rm Rot}_{\rm CGC}$) each lead to an $\sim 15-20\%$ increase of v_2 in mid-central collisions. However, these calculated results still fall below the data.

Figure 5.28(b) compares the same data with three JR models for the same matter profiles, but calculated for a line integral motivated by AdS/CFT correspondence $I = \int dl\, l\rho$. The stronger l dependence for $\rho_{\rm GL}$ significantly increases (by $> 50\%$) the calculated v_2, and brings it close to the data for mid-central collisions. However, a sizable fractional difference in central bin seem to require additional increase from fluctuations and CGC geometry. Fig. 5.28 (b) also shows a CT model from [105], which implements the AdS/CFT l dependence within the ASW framework [1]; it compares reasonably well with the JR model for $\rho_{\rm GL}$ (short-dashed curves). Note that the CT or JR models in Fig. 5.28 have been tuned independently to reproduce the 0-5% π^0 $R_{\rm AA}$ data, and they all describe the centrality dependence of $R_{\rm AA}$ very well (see Fig. 5.28 (c)-(d)). On the other hand, these models predict a stronger suppression for

[1]The two CT models (ASW and AdS/CFT) in Fig. 5.28 are based on a 3D ideal hydrodynamic code slightly different from that of the ASW model shown in Fig. 5.20.

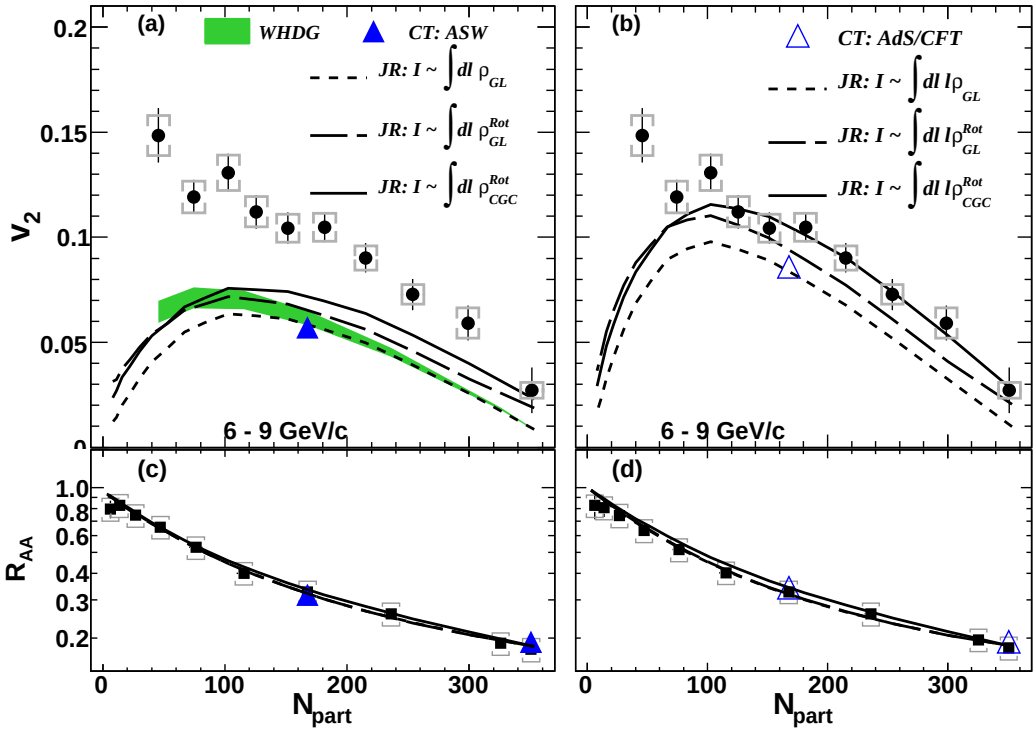

Figure 5.28: (Color online) v_2 vs $N_{\rm part}$ in 6-9 GeV/c compared with various models: (a) WHDG [92] (shaded bands), ASW [105] (solid triangle), and three JR calculations [104] with quadratic l dependence with longitudinal expansion for Glauber geometry (dashed lines), rotated Glauber geometry(long dashed lines) and rotated CGC geometry (solid lines); (b) Same as (a) except that AdS/CFT modified calculation in ASW framework (triangle) from [105] is shown and the JR calculations were done for cubic l dependence with longitudinal expansion; (c)-(d) the comparison of calculated $R_{\rm AA}$s from these models with data.

dihadrons than for single hadrons, opposite to experimental findings [106], thus a global confrontation of any model with all experimental observables is warranted.

Chapter 6

Summary

We have detailed the methods, procedures and results of azimuthal anisotropy measurements of π^0/η in in Au+Au collisions at PHENIX in the RHIC Year-7's run. The v_2 and $R_{AA}(\Delta\phi)$ results are presented as funtions of p_T and centralities, which are greatly improved compared to the previous measurement in Run-4. The p_T range covers 1-18 GeV/c, in more detailed centrality selections, with the aid of four times more statistics and better reaction plane resolution in Run-7.

We have shown that π^0 $v_2(p_T)$ is consistent with previous measurement and the charged pion results, but with smaller uncertainties and larger p_T reach. The systematic errors mainly come from the uncertainties in the reaction plane determination, that is estimated by comparing the results with different reaction plane detectors in different pseudorapidity ranges. It has shown that by combining MPC and RXNin detectors to measure reaction plane angle, the jet bias at high p_T are mostly suppressed, and the resolution can be improved by at least 40% compared to MPC alone.

The high quality data shows that v_2 gradually decreases in the p_T range of 3-7 GeV/c, and stays relatively flat at higher p_T, which implies a transition from particle production dominated by the soft process to a p_T region dominated by hard process. We have investigate the scaling behaviors of $v_{2(4)}$ in different p_T ranges, and its relation with the initial geometric asymmetry. At low KE_T/n_q, the v_2 of different particle species follows the constituent quark number scaling, while it seems to break from such scaling at $\mathrm{KE}_T/n_q \sim 1$ GeV, indicating hard process becomes dominant. v_4 scaled by n_q^2 also shows quark number scaling at low KE_T/n_q, that further confirms the picture of partonic collectivity in the medium. We compared the results of $v_2(p_T)$ and $R_{AA}(p_T)$ of π^0 and inclusive charged hadron, both of which start to merge at $p_T \sim 5$ GeV/c, the observation we argue that jet quenching may start to play an important role at such p_T. We have studied the eccentricities of two different geometric models, MC-Glauber and MC-KLN (CGC), and scaled v_2 by two types of eccentricity. We found that CGC scales v_2 data better than Glauber model, which could yield smaller η/s value. The v_2/ϵ at high p_T displays similar centrality dependence as that at low p_T, which may suggest that both collective flow and jet quenching can effectively convert initial geometic asymmetry to final momentum anisotropy.

We have shown the consistent v_2 and R_{AA} results of π^0 and η mesons above intermediate p_T region (>3 GeV/c). Additionally, these two observables of inclusive charged hadron $h^{\pm}$ and π^0 are also shown to be consistent at high p_T (>5 GeV/c). These comparisons imply that the high p_T particles are mainly from the leading parton fragments.

The differential probe of $R_{AA}(\Delta\phi)$ is calculated in the same p_T range for

six centralities. The detailed orientation decomposition in each centrality provides better handle on the average path length that a jet would go through. We found that R_{AA} along the direction of reaction plane has stronger p_T and centrality dependences than the R_{AA} normal to the reaction plane. For example, in $N_{\rm part} > 100$, the R_{AA} along the direction of normal to the reaction plane is almost constant, a trend seen in most p_T bins. By contrast, the R_{AA} along the reaction plane increases about factor of 2 from central to peripheral collisions. This provides a compelling argument that the geometry plays big part in the jet suppression, because the geometry length normal to the reaction plane varies much slower across centralities than the length along the reaction plane.

We have compared the experimental results with the pQCD based model calculations. The v_2 in WHDG model at high p_T (> 5 GeV/c) has little p_T dependence, and can only describe data at $p_T > 7$ GeV/c in mid-central collisions. Three pQCD models (AMY, HT and ASW) implemented in the identical hydro medium to calculate the jet energy loss are able to predict the inclusive R_{AA}, but fail to describe the large anisotropy observed in the experimental data. The geometric models which assume formation time effect or non-linear dependence of energy loss on the medium density can qualitatively describe the centrality dependence of high p_T v_2.

The failure of pQCD models in describing the large anisotropy has motivated us to study other effects, such as initial geometry uncertainty (Glauber vs CGC), eccentricity fluctuations which is absent from most pQCD models, higher order path length dependence of energy loss indicated by AdS/CFT. A jet absorption model which can describe the centrality dependence of inclu-

sive R_{AA} and di-hadron suppression, is deployed to include the effects. The results show that stronger l dependence and fluctuations increase v_2 significantly, while inclusive R_{AA} has little sensitivity to both case, indicating that azimuthal anisotropy is a more sensitive probe for jet quenching than the inclusive R_{AA}. In the central collisions, for its intrinsic symmetric shape, the initial geometry fluctuation has to be considered to match the calculation with the high p_T v_2 data. Estimates of the v_2 increase due to modifications of initial geometry from gluon saturation effects and fluctuations indicate that they are insufficient to reconcile data and theory. Incorporating an AdS/CFT-like path-length dependence for jet quenching in a pQCD-based framework [105] and a schematic model [101, 104] both compare well with the data. However, more detailed study beyond these simplified models are required to quantify the nature of the path-length dependence. Our precision data provide key experimental constraints on the role of initial geometry and for elucidating the jet quenching mechanism.

Bibliography

[1] Gross, D. J. and F. Wilczek, Phys. Rev. Lett. **30**, 1343 (1973).

[2] Cheuk-Yin Wong "Introduction to High-Energy Heavy-Ion Collisions", World Scientific.

[3] A. Bazavov *et al.*, Phys. Rev. D **80**, 014504 (2009) [arXiv:0903.4379 [hep-lat]].

[4] E. Shuryak, Phys. Rept.**61**, 71 (1980).

[5] Y. Aoki, Z. Fodor, S. D. Katz and K. K. Szabo, Phys. Lett. B **643**, 46 (2006) [arXiv:hep-lat/0609068].

[6] H. G. Baumgardt *et al.*, Z. Phys. A**273**, 359 (1975)

[7] S. Nagamiya and M. Gyulassy, Adv. Nucl. Phys.**13**, 201 (1984).

[8] J. W. Harris and B. Muller, Ann. Rev. Nucl. Part. Sci. **46**, 71 (1996) [arXiv:hep-ph/9602235].

[9] K. Adcox *et al.* [PHENIX Collaboration], Nucl. Phys. A **757**, 184 (2005) [arXiv:nucl-ex/0410003].

[10] J. Adams *et al.* [STAR Collaboration], Nucl. Phys. A **757**, 102 (2005) [arXiv:nucl-ex/0501009].

[11] I. Arsene *et al.* [BRAHMS Collaboration], Nucl. Phys. A **757**, 1 (2005) [arXiv:nucl-ex/0410020].

[12] B. B. Back *et al.*, Nucl. Phys. A **757**, 28 (2005) [arXiv:nucl-ex/0410022].

[13] U. W. Heinz and M. Jacob, arXiv:nucl-th/0002042.

[14] M. Gyulassy, arXiv:nucl-th/0403032.

[15] M. Gyulassy and L. McLerran, Nucl. Phys. A **750**, 30 (2005) [arXiv:nucl-th/0405013].

[16] B. Muller and J. L. Nagle, Ann. Rev. Nucl. Part. Sci. **56**, 93 (2006) [arXiv:nucl-th/0602029].

[17] N. Armesto *et al.*, J. Phys. G **35**, 054001 (2008) [arXiv:0711.0974 [hep-ph]].

[18] http://qgp.phy.duke.edu/.

[19] H. Satz, arXiv:hep-ph/0212046.

[20] L. D. McLerran and R. Venugopalan, Phys. Rev. D **49**, 2233 (1994) [arXiv:hep-ph/9309289].

[21] E. Iancu and R. Venugopalan, arXiv:hep-ph/0303204.

[22] U. W. Heinz and P. F. Kolb, Nucl. Phys. A **702**, 269 (2002) [arXiv:hep-ph/0111075].

[23] S. S. Adler *et al.* [PHENIX Collaboration], Phys. Rev. Lett. **91**, 182301 (2003) [arXiv:nucl-ex/0305013].

[24] K. Adcox *et al.* [PHENIX Collaboration], Phys. Rev. Lett. **89**, 212301 (2002) [arXiv:nucl-ex/0204005].

[25] K. Adcox *et al.* [PHENIX Collaboration], Phys. Rev. Lett. **88**, 022301 (2002) [arXiv:nucl-ex/0109003].

[26] N. Demir and S. A. Bass, Phys. Rev. Lett. **102**, 172302 (2009) [arXiv:0812.2422 [nucl-th]].

[27] S. S. Adler *et al.* [PHENIX Collaboration], Phys. Rev. Lett. **94**, 232302 (2005) [arXiv:nucl-ex/0411040].

[28] G. Policastro, D. T. Son and A. O. Starinets, Phys. Rev. Lett. **87**, 081601 (2001); P. Kovtun, D. T. Son and A. O. Starinets, Phys. Rev. Lett. **94**, 111601 (2005).

[29] D. Teaney, Nucl. Phys. A **830**, 891C (2009) [arXiv:0907.4843 [nucl-th]].

[30] D. A. Teaney, arXiv:0905.2433 [nucl-th].

[31] R. A. Lacey, A. Taranenko and R. Wei, arXiv:0905.4368 [nucl-ex].

[32] P. Romatschke and U. Romatschke, Phys. Rev. Lett. **99**, 172301 (2007) [arXiv:0706.1522 [nucl-th]].

[33] N. Borghini and J. Y. Ollitrault, Phys. Lett. **B642**, 227 (2006)

[34] A. Tang, Nucl. Phys. A **830**, 673C (2009) [arXiv:0907.4513 [nucl-ex]].

[35] L. P. Csernai, J. I. Kapusta and L. D. McLerran, Phys. Rev. Lett. **97**, 152303 (2006)

[36] A. Adare *et al.* [PHENIX Collaboration], Phys. Rev. Lett. **98**, 162301 (2007) [arXiv:nucl-ex/0608033].

[37] J. Jia and C. Zhang, Phys. Rev. C **75**, 031901 (2007) [arXiv:hep-ph/0608187].

[38] M. Luzum and P. Romatschke, Phys. Rev. C **78**, 034915 (2008) [Erratum-ibid. C **79**, 039903 (2009)] [arXiv:0804.4015 [nucl-th]].

[39] T. Hirano and Y. Nara, Phys. Rev. C **79**, 064904 (2009) [arXiv:0904.4080 [nucl-th]].

[40] U. W. Heinz, J. S. Moreland and H. Song, Phys. Rev. C **80**, 061901 (2009) [arXiv:0908.2617 [nucl-th]].

[41] U. W. Heinz, arXiv:0901.4355 [nucl-th].

[42] F. Karsch and E. Laermann, arXiv:hep-lat/0305025.

[43] J. C. Collions *et al.*, in Perturbative Quantum Chromodynamics, ed. A. H. Mueller, AdV. Ser. Direct. High Energy Phys. **5** 1 (1988).

[44] W. M. Geist *et al.*, Phys. Repts.**197**, 263 (1990).

[45] B. Alper *et al.*, Nucl. Phys. **B100**, 237 (1975).

[46] F. Abe *et al.*, Phys. Rev. Lett. **61**, 1819 (1988).

[47] S. S. Adler *et al.* [PHENIX Collaboration], Phys. Rev. Lett. **91**, 241803 (2003) [arXiv:hep-ex/0304038].

[48] F. Aversa *et al.*, Nucl. Phys. **B327**, 105 (1989); B. Jager *et al.*, Phys. Rev. **D67**, 054005 (2003); D. de Florian, Phys. Rev. **D67**, 054004 (2003).

[49] B. A. Kniehl *et al.*, Nucl. Phys. **B597**, 337 (2001).

[50] S. Kretzer, Phys. Rev. **D62**, 054001 (2000).

[51] X. N. Wang and M. Gyulassy, Phys. Rev. Lett. **68**, 1480 (1992).

[52] M. Gyulassy and M. Plumer, Phys. Lett. **B243**, 432 (1990); R. Baier *et al.*, Phys. Lett. **B345**, 277 (1995).

[53] R. Baier, D. Schiff, and B. G. Zakharov, Ann. Rev. Nucl. Part. Sci. **50**, 37 (2000).

[54] R. Baier, Y. L. Dokshitzer, A. H. Mueller and D. Schiff, J. High Energy Phys. **9**, 33 (2001).

[55] R. Baier, Y. L. Dokshitzer, A. H. Mueller, S. Peigne and D. Schiff, Nucl. Phys. **B483**, 291 (1997).

[56] S. S. Adler *et al.* [PHENIX Collaboration], Phys. Rev. C **75**, 024909 (2007) [arXiv:nucl-ex/0611006].

[57] S. A. Bass, C. Gale, A. Majumder, C. Nonaka, G. Y. Qin, T. Renk and J. Ruppert, Phys. Rev. C **79**, 024901 (2009) [arXiv:0808.0908 [nucl-th]].

[58] J. Adams *et al.* [STAR Collaboration], Phys. Rev. Lett. **91**, 072304 (2003) [arXiv:nucl-ex/0306024].

[59] A. Adare *et al.* [PHENIX Collaboration], Phys. Rev. C **78**, 014901 (2008) [arXiv:0801.4545 [nucl-ex]].

[60] J. Casalderrey-Solana, E. V. Shuryak and D. Teaney, J. Phys. Conf. Ser. **27**, 22 (2005) [Nucl. Phys. A **774**, 577 (2006)] [arXiv:hep-ph/0411315].

[61] H. Liu, K. Rajagopal and U. A. Wiedemann, Phys. Rev. Lett. **97**, 182301 (2006).

[62] S. Afanasiev *et al.* [PHENIX Collaboration], Phys. Rev. C **80**, 054907 (2009) [arXiv:0903.4886 [nucl-ex]].

[63] M. Harrison, T. Ludlam, and S. Ozaki. RHIC project overview. Nucl. Instrum. Meth. A**499**, 235244 (2003).

[64] K. Adcox *et al.*, NIM**A499**, 469-479 (2003).

[65] M. Allen *et al.*, NIM**A499**, 549-559 (2003).

[66] K. Adcox *et al.*, NIM**A499**, 489-507 (2003); M. Aizawa *et al.*, NIM**A499**, 508-520 (2003); L. Aphecetche *et al.*, NIM**A499**, 521-536 (2003).

[67] G. David *et al.*, IEEE Trans. Nucl. Sci. **45**, 692 (1998).

[68] A. Adare *et al.* [PHENIX Collaboration], Phys. Rev. C **81**, 034911 (2010) [arXiv:0912.0244 [nucl-ex]].

[69] J. Haggerty *et al.*, "Letter of intent for PHENIX reaction plane detector", Internal Letter of Intent, (2006).

[70] M. Chiu [PHENIX Collaboration], AIP Conf. Proc. **915**, 539 (2007) [arXiv:nucl-ex/0701031].

[71] M. L. Miller, K. Reygers, S. J. Sanders and P. Steinberg, Ann. Rev. Nucl. Part. Sci. **57**, 205 (2007) [arXiv:nucl-ex/0701025].

[72] K. Homma, PHENIX analysis note 103.

[73] J. Nagle *et al.*, PHENIX analysis note 113, 387.

[74] B. Alver, M. Baker, C. Loizides and P. Steinberg, arXiv:0805.4411 [nucl-ex].

[75] S. A. Voloshin, A. M. Poskanzer and R. Snellings, arXiv:0809.2949 [nucl-ex].

[76] A. M. Poskanzer and S. A. Voloshin, Phys. Rev. C **58**, 1671 (1998) [arXiv:nucl-ex/9805001].

[77] Tadaaki Isobe, "Production of Direct Photons and Neutral Pions in Relativistic Au+Au Collisions", Ph.D. thesis, University of Tokyo.

[78] N. Borghini and J. Y. Ollitrault, Phys. Rev. C **70**, 064905 (2004) [arXiv:nucl-th/0407041].

[79] J. Y. Ollitrault, arXiv:nucl-ex/9711003.

[80] Jiangyong Jia, Nucl. Phys. **A834**, 229 (2010).

[81] S. Huang [PHENIX Collaboration], J. Phys. G **35**, 104105 (2008) [arXiv:0804.4864 [nucl-ex]].

[82] K. Adcox *et al.* [PHENIX Collaboration], Phys. Rev. C **69**, 024904 (2004) [arXiv:nucl-ex/0307010].

[83] D. Teaney, Phys. Rev. C **68**, 034913 (2003) [arXiv:nucl-th/0301099].

[84] A. Adare *et al.* [PHENIX Collaboration], Phys. Rev. C **82**, 011902 (2010) [arXiv:1005.4916 [nucl-ex]].

[85] B. Alver *et al.* [PHOBOS Collaboration], Phys. Rev. Lett. **104**, 062301 (2010) [arXiv:0903.2811 [nucl-ex]].

[86] Jiangyong Jia, "High-p_T Charged Hadron Suppression in Au+Au Collisions at $\sqrt{s_{NN}} = 200$ GeV", Ph.D. thesis, Stony Brook University.

[87] B. Alver *et al.*, Phys. Rev. C **77**, 014906 (2008)

[88] H. J. Drescher, A. Dumitru, A. Hayashigaki and Y. Nara, Phys. Rev. C **74**, 044905 (2006) [arXiv:nucl-th/0605012].

[89] H. J. Drescher and Y. Nara, Phys. Rev. C **75**, 034905 (2007) [arXiv:nucl-th/0611017].

[90] W. Broniowski, P. Bozek and M. Rybczynski, Phys. Rev. C **76**, 054905 (2007)

[91] D. Kharzeev, E. Levin and M. Nardi, Nucl. Phys. A **730**, 448 (2004) [Erratum-ibid. A **743**, 329 (2004)]

[92] S. Wicks, W. Horowitz, M. Djordjevic and M. Gyulassy, Nucl. Phys. A **784**, 426 (2007) [arXiv:nucl-th/0512076].

[93] M. Gyulassy, P. Levai and I. Vitev, Nucl. Phys. B **571**, 197 (2000) [arXiv:hep-ph/9907461].

[94] A. Adare *et al.* [PHENIX Collaboration], Phys. Rev. C **77**, 064907 (2008) [arXiv:0801.1665 [nucl-ex]].

[95] S. S. Gubser, D. R. Gulotta, S. S. Pufu and F. D. Rocha, JHEP **0810**, 052 (2008) [arXiv:0803.1470 [hep-th]].

[96] H. Liu, K. Rajagopal and U. A. Wiedemann, Phys. Rev. Lett. **97**, 182301 (2006) [arXiv:hep-ph/0605178].

[97] A. Adare *et al.*, Phys. Rev. Lett. **101**, 232301 (2008)

[98] D. E. Kharzeev, arXiv:0806.0358 [hep-ph].

[99] J. Liao and E. Shuryak, Phys. Rev. Lett. **102**, 202302 (2009) [arXiv:0810.4116 [nucl-th]].

[100] V. S. Pantuev, JETP Lett. **85**, 104 (2007) [arXiv:hep-ph/0506095].

[101] A. Drees, H. Feng and J. Jia, Phys. Rev. C **71**, 034909 (2005) [arXiv:nucl-th/0310044].

[102] E. V. Shuryak, Phys. Rev. C **66**, 027902 (2002)

[103] V. Greco, C. M. Ko and P. Levai, Phys. Rev. C **68**, 034904 (2003); R. J. Fries, B. Muller, C. Nonaka and S. A. Bass, Phys. Rev. C **68**, 044902 (2003)

[104] J. Jia and R. Wei, Phys. Rev. C **82**, 024902 (2010) [arXiv:1005.0645 [nucl-th]].

[105] C. Marquet and T. Renk, Phys. Lett. B **685**, 270 (2010)

[106] A. Adare *et al.*, Phys. Rev. Lett. **104**, 252301 (2010) [arXiv:1002.1077 [nucl-ex]].

[107] A. Adare *et al.*, Phys. Rev. Lett. **105**, 142301 (2010).